

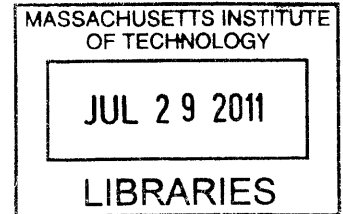
Integration of Real Time Oxygen Measurements with a 3D Perfused Tissue Culture System

by

Samuel Walker Inman

Bachelor of Science in Mechanical Engineering
Georgia Institute of Technology, 2004

Master of Science in Mechanical Engineering
Massachusetts Institute of Technology, 2006



ARCHIVES

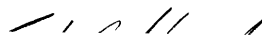
SUBMITTED TO THE DEPARTMENT OF MECHANICAL ENGINEERING IN
PARTIAL FULFILLMENT OF THE REQUIREMENTS FOR THE DEGREE OF

DOCTOR OF PHILOSOPHY IN MECHANICAL ENGINEERING
AT THE
MASSACHUSETTS INSTITUTE OF TECHNOLOGY

June 2011


© 2011 Massachusetts Institute of Technology. All Rights Reserved

Signature of Author:



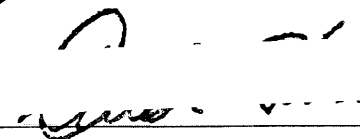
Department of Mechanical Engineering
May 23, 2011

Certified by:



Dr. Linda G. Griffith
Professor Biological Engineering and Mechanical Engineering
Thesis Supervisor

Accepted By:



Dr. David E. Hardt
Professor of Mechanical Engineering
Chairman, Committee for Graduate Students

this page is blank

Integration of Real Time Oxygen Measurements with a 3D Perfused Tissue Culture System

by

Samuel Walker Inman

Submitted to the Department of Mechanical Engineering
on May 23, 2011 in partial fulfillment of the
requirements for the Degree of
Doctor of Philosophy in Mechanical Engineering

ABSTRACT

In vitro models that capture the complexity of human tissue and organ behaviors in a scalable and easy-to-use format are of increasing interest for both technological applications in drug development and in basic biology research. Tissues and organs are perfused continuously with blood, which delivers nutrients, oxygen, and macromolecular regulatory molecules. In vitro culture models that incorporate local microperfusion in a format that allows accesses to cells and their microenvironment are desirable to a broad research community. This thesis describes a platform that features an array of bioreactors that foster three dimensional tissue organization under continuous perfusion. Each bioreactor contains a scaffold that supports formation of hundreds of 3D microscale tissue units. Perfusion through the tissue is achieved using integrated pneumatic diaphragm micropumps. Pumps continuously circulate cell culture medium within each of the fluidically isolated bioreactors in the array. Pulsatile flow from the pumps is filtered using integrated fluidic capacitors such that the flow rate through the scaffold is constant. The format of the device mimics the familiar multiwell tissue culture plate and is easily integrated into existing laboratory facilities.

One desirable feature for both parsing metabolic function and assessing response to treatments is a real time read out of oxygen tension at key points in the bioreactor. Such added dimension of real time measurement significantly enhances the value of a cue-response experiment such as a liver drug toxicology study. The thesis describes optical oxygen sensors that measure the florescence decay time of a ruthenium complex, which varies predictably in different oxygen environments. The sensors excite a layer of ruthenium glued to the end of an optical fiber using a stochastic signal from a light emitting diode (LED). The response is then measured on a photodiode. System identification techniques are used to determine the relevant time constants which are subsequently converted to oxygen measurements. Application to real time monitoring of liver tissue function is used for illustration of the utility of the measurements.

Thesis Supervisor: Linda G. Griffith

Title: Professor of Biological Engineering and Mechanical Engineering

this page is blank

ACKNOWLEDGEMENTS

Many people throughout MIT have contributed to the success of projects described in this thesis. Mathew Weissinger was tremendously helpful with development and characterization of bioreactor systems, development of the oxygen multiplex system, and biological characterization of the bioreactor. Steven Wasserman and Steve Nagle provided invaluable help with the electronics and optics in the oxygen sensors. Karel Domansky and James Serdy made substantial contributions to bioreactor development and fabrication, and Professor David Trumper helped guide this development. Ajit Dash and Rachel Pothier were instrumental in characterizing the bioreactor systems. Jean-Christophe Nave helped with flow simulations. Niraj Inamdar also provided useful perspectives on flow simulations and optical oxygen sensors. I also owe thanks to our lab managers Hsinhwa Lee and Mary Rhoads.

Financial support for portions of the project was provided through collaboration with Roche headed by Adrian Roth. Support was also provided through collaboration with UNC and with the University of Pittsburgh.

Collectively my thesis committee helped provide a focus to my work which was tremendously helpful. Steven Tannebaum in particular was instrumental in this respect. I am also indebted to Ian Hunter for introducing me to system identification and for teaching it as a form of magic. Most importantly, my advisor Linda Griffith has been incredibly supportive throughout my time at MIT. I have been fortunate to work with great people and it has made my time at MIT very enjoyable.

Finally I am grateful to my wife Amanda for her patience with my going back to school.

TABLE OF CONTENTS

ABSTRACT.....	3
ACKNOWLEDGEMENTS.....	5
TABLE OF CONTENTS.....	6
LIST OF FIGURES.....	8
LIST OF TABLES.....	12
1. INTRODUCTION.....	13
2. BIOREACTOR DESIGN.....	17
2.1 Concept of multiwell bioreactor systems.....	17
2.2 Pump.....	19
2.2.1 Pump Function.....	19
2.2.2 Pump Model.....	23
2.2.3 Pump Characterization.....	25
2.3 Capacitor.....	29
2.3.1 Capacitor Operation.....	30
2.3.2 Capacitor Model.....	31
2.3.3 Capacitor Characterization.....	37
2.3.4 Pressure sensing through the capacitor membrane.....	40
2.4 Auxiliary Systems.....	43
2.4.1 Controller.....	43
2.4.2 Imaging / Assay Plate.....	44
2.5 Fabrication, Sterilization and Assembly.....	45
2.6 Design Parameter Selection.....	46
2.7 Discussion.....	49
3. OXYGEN ENVIRONMENT.....	50
3.1 Oxygen Consumption.....	50
3.1.1 Preliminary Oxygen Measurements.....	51
3.1.2 Convection-Diffusion Reaction Equations.....	54
3.1.3 Scaffold model.....	56
3.2 Formulation of interfacial absorption analysis.....	65
3.2.1 Non-dimensionalization of mass transport inside the bioreactor.....	65
3.3 Oxygen absorption modeling for finding oxygen absorption potential.....	69
3.4 Bioreactor design.....	72
3.4.1 Discussion of design parameters influencing oxygen absorption capacity.....	73

3.4.2 Oxygen test bioreactors designed with three different oxygen absorption capacities.....	74
3.5 Influence of oxygen environment on rat liver cell culture	76
3.5.1 Oxygen environment evaluation	76
3.5.2 Biological results	79
3.5.3 High oxygen capacity bioreactor.....	80
3.6 Experimental application of oxygen sensors.....	81
3.7 Discussion	83
4. OXYGEN SENSORS	84
4.1 Introduction.....	84
4.2 Optical oxygen sensor background	86
4.3 Calibrations and oxygen readouts.....	89
4.4 Optical oxygen sensor design	90
4.5 Measurement method	93
4.5.1 System identification, selection of the model	95
4.5.2 Least squares estimation of model parameters	97
4.5.3 Computation of P, B, F using auto-and cross correlations.....	99
4.5.4 Computing model parameters.....	102
4.5.5 Analysis of noise.....	105
4.5.6 Computing the time constant	106
4.5.7 Oxygen measurement.....	108
4.5.8 Minimizing the excitation period.....	109
4.5.9 Multiplexing sensors with different input signals.....	111
4.6 Discussion	112
5. CONCLUSIONS.....	114
REFERENCES	115
APPENDIX	118
Appendix A.1: Generations of bioreactor devices.....	118
Appendix A.2: Scaling the mass transport equation	119
Appendix A.3: 1D Radial diffusion reaction finite differences	121
Appendix A.4: Navier-Stokes approximations using finite differences	123
Appendix A.5: Analysis of flow in the filter	124

LIST OF FIGURES

Figure 2.1: A live-dead (green-red) stain of human and rat hepatocytes cultured in the scaffold alongside a schematic cross section (1A). The scaffold resides within a well of the bioreactor (1B), and there are 12 isolated 3-D perfused bioreactors on each culture plate (1C).....	17
Figure 2.2: (a) The scaffold with no cells and (b) the scaffold with human tissue	18
Figure 2.3: Schematic cross-section of the pumping system.	20
Figure 2.4: Schematic cross-sections and top view photographs of the valves and pump chamber illustrating the pump cycle.....	21
Figure 2.5: A 3D model of the pump elements. Only the volumes filled with fluid (blue) or air (grey) are shown. Both the top (a) and bottom half (b) of the pump features are presented.	22
Figure 2.6: The clearance of air bubbles through one complete cycle of the pump. In the first image, the pump is filled with a air bubbles (a). The pump chamber is drained and the bubbles are ejected (b) and the chamber is refilled with fluid (c).	23
Figure 2.7: A balance of forces between pressure acting on the circular area of the membrane and tension in the membrane acting around the circumference of the membrane.....	24
Figure 2.8: Stroke volume in relation to actuation pressure. The pump was driven at 5 Hz.	26
Figure 2.9: Volume of fluid ejected from the pump chamber during phase five of the pumping cycle for various pneumatic pressures.	27
Figure 2.10: Volume of fluid filling the pump chamber during phase 2 of the pump cycle.....	28
Figure 2.11: Flow rate as a function of frequency and head pressure for a pneumatic pressure of 40 kPa.	29
Figure 2.12: Volume output from the pump through one pumping cycle is plotted versus time. Numbers indicate phases of the pump cycle from figure 2.4. Fluid flow in phase five is the result of draining the pump chamber. The smaller volume change in phase 6 and 4 represents draining and filling the exit valve.	30
Figure 2.13: A two-capacitor system filters flow pulses both entering (a) and leaving (b) the pump. In (a), lower than atmospheric pressure draws fluid through the fluidic resistor, and in (b) elevated pressures drive flow through the resistor. The bioreactor uses a single capacitor between the pump and scaffold.....	31
Figure 2.14: Capacitance versus pressure for capacitors of different diameters.....	32
Figure 2.15: Ratio of time constant to cycle time of the pump plotted in log scale across a range of flow rates for several capacitor diameters.	35
Figure 2.16: Volume displacement of the capacitor versus fluid pressure is compared against the model. Capacitors of two diameters (5 and 10 mm) were measured and modeled.	38
Figure 2.17: Capacitance measurements compared with the model.	38
Figure 2.18: Comparison of measured capacitor performance to the capacitor model for a flow rate of 0.05 mL/min. The time constant ratio, estimated using 2.14, is show for the two capacitors.	39

Figure 2.19: Flow from two different capacitors for several flow rates. The time constant ratio from (2.14) is shown for each curve.	40
Figure 2.20: Optical position sensor measures reflected light from a surface. The intensity of light is often correlated with the distance of the surface away from the sensor.	41
Figure 2.21: Linear range of the Vishay TCRT 5000 matches the desired range for measuring the position of the capacitor membrane during an experiment.	41
Figure 2.22: Evaluation of the position sensor response to increasing head pressure.	43
Figure 2.23: Control panel for operating 3 bioreactors.	44
Figure 2.24: Imaging / assay plate containing 24 wells.	45
Figure 3.1: Structure of liver, from whole liver on the left to the liver sinusoid on the right ^{59, 60}	50
Figure 3.2: Oxygen probes are sketched as black rectangles above the scaffold (left) and in the reservoir (right). The fluid is colored to show and expected distribution of oxygen throughout the bioreactor when flow is directed up through the scaffold. This simulation is discussed in detail later in the chapter.	52
Figure 3.3: Measured concentration of dissolved oxygen in reservoir and reactor wells seeded with rat hepatocytes: (a) As a function of time post seeding with a flow rate of $0.3 \mu\text{L channel}^{-1} \text{min}^{-1}$ and a sampling interval of 5 minutes. (b) As a function of flow rate (immediately following the time course measurement) with a sampling interval of 1 minute.	52
Figure 3.4: Schematic of bulk oxygen transport length and velocity scales to the scaffold for comparison of diffusion to convection using the Peclet number.	57
Figure 3.5: A representative image of a scaffold looking down into the channels. This image shows a variety of common tissue structures. The left hand image shows live cells stained green and dead cells stained red. The image on the right shows the same cells, but is analyzed to find the average cross section of the flow path in the channel.	58
Figure 3.6: Grid layout for finite differences estimation of oxygen consumption in a channel of the scaffold. Concentration estimates are found at equally spaced intervals along the radius of the tissue in the channel. The concentration at the fluid-tissue interface is fixed.	60
Figure 3.7: Distribution of O_2 concentration in a simplified model of a channel in the scaffold. Channel diameter is $340 \mu\text{m}$. The different lines represent different inner diameters of the tissue annulus. The legend shows annulus diameter in microns. O_2 Concentration at the tissue surface is $180 \mu\text{M}$	61
Figure 3.8: Total oxygen consumption increases with increasing tissue volume until diffusion limitations restrict oxygen transport to the outside edge of the channel. Values were obtained by integration of equation 3.1 for a channel height of $200 \mu\text{m}$	61
Figure 3.9: Increasing the amount of tissue in the channel beyond oxygen diffusion limits (denoted by d) effectively reduces the volume of tissue that is provide with sufficient oxygen. Although the total volume of tissue (denoted by blue and red color) is greater in the channel on the right, the volume of tissue with adequate oxygen supply, shown in blue, is greater for the channel on the left.	62
Figure 3.10: Simulation of consumption within one channel of the scaffold. The images show cross-sections of the circular channels. Dotted lines depict where tissue is contained in the scaffold. Fluid flow is constrained to the center of the channel where no cells reside. The colormap shows.	

the concentration of oxygen. The model uses polar coordinates so is an axi-symmetric 3D representation.	64
Figure 3.11: oxygen absorption schematic.....	70
Figure 3.12: Oxygen absorption potential across a wide range of design and operating conditions shows high correlation with the Peclet number for oxygen transport across the surface channel.....	71
Figure 3.13: Total absorption into the system normalized to the difference between oxygen saturation and the concentration of oxygen exiting the scaffold increases with increasing Peclet number.	72
Figure 3.14: Bioreactor plate with three different designs used to study the influence of oxygen concentration on liver cell cultures. A schematic is shown on the left with the solid model on the right.	75
Figure 3.15: Oxygen sensor multiplexor designed to cycle sensing equipment between three different oxygen probes. After oxygen is recorded on one probe, the multiplexor automatically reconnects the sensing equipment with the next probe and waits for a measurement to be taken. Once a measurement is taken, the multiplexor connects the sensing equipment with the next sensor in the series. The process can repeat indefinitely.....	77
Figure 3.16: Shows two days of oxygen concentration measurements for rat cell culture. The top plot shows concentration measurements from 12 sensors placed in 6 bioreactors. The black line is saturating oxygen concentration as predicted from atmospheric pressure. Blue curves are from reactors with the highest oxygen absorption potential, green are from bioreactors with mid range absorption potential and red are from bioreactors with the lowest oxygen absorption potential. The initial high concentration and spike at day 1 result from medium exchanges where oxygen saturated medium was added to the bioreactor. The oxygen sensor above the scaffold in one of the high oxygen bioreactors (blue lines) appears not to have been completely submerged in the medium during the first day. Absorption potential and metabolic activity during this day are therefore not representative. During the second day, absorption potential (middle plot) agrees with predictions from the models. The gradual decline in consumption (bottom plot) indicates a progressively decline in metabolic activity. The black line in this plot is the product of flow rate and saturating oxygen concentration, indicating the total amount of oxygen that would be available for consumption if absorption potential is driven to 100%.....	78
Figure 3.17: Total protein retained in the scaffold at the end of culture. A small but consistent trend shows that high oxygen content bioreactors retain more cells as measured by total protein.	79
Figure 3.18: Albumin production and total bile acid production in different oxygen environments.	80
Figure 3.19: High oxygen content bioreactor	81
Figure 3.20: Oxygen concentration measurements following drug dose (day 3) show an immediate drug response, followed by stabilization in metabolic activity after roughly 12 hours.	82
Figure 3.21: Oxygen concentration and oxygen consumption at the end of the drug incubation show a clear dose response to the drug. Error bars indicate the standard deviation in consumption measurements over the last 7 hours of culture.....	82
Figure 4.1: Influence of time constant measurement error on predicted oxygen concentration.	90
Figure 4.2: Optical properties of relevant sensor components and typical excitation and emission spectrum of ruthenium complexes ⁷⁷	91

Figure 4.3: Schematic representation of the oxygen measuring sensor. The ruthenium layer on the left side of the schematic is placed in medium for oxygen analysis. The electronic circuit is controlled by a microcontroller and readings from the ADC are sent to a computer for signal processing. 92

Figure 4.4: Oxygen sensor breakout showing LED and photodiode attached to the excitation, amplification and measurement circuit board. The filter cube with lid removed shows placement of the optical filters and mirrors. The optical fiber and ruthenium layer (not shown) attach to the filter cube..... 92

Figure 4.5: Schematic of filter cube showing blue LED and blue excitation filter. A first surface mirror is used to reflect blue light to a dichroic mirror. Blue light reflected off the dichroic is sent through a lens into the end of an optical fiber. Red light from the ruthenium probe is collimated by the lens, passed through the dichroic and through an emission filter before intensity is measured on the photodiode..... 92

Figure 4.6: Stochastic binary pattern applied to the LED for excitation of the ruthenium sensor and response of the sensor for a short time segment. The x-axis shows time normalized by the sampling interval (typically 1 to 10 μ s)..... 93

Figure 4.7: Autocorrelation and power spectrum of the excitation signal. The sample interval is 6 μ s and the time constant for the first order low pass filter is 30 μ s. The power spectrum of the excitation signal is not exactly representative of a first order low pass filter because it has been hard limited. 94

Figure 4.8: Measured signal and predicted signal for two different model structures, the ARX model is on the left and FIR is on the right. The prediction error is shown in red which is comparable for both models..... 103

Figure 4.9: The relationship between measurement and model prediction indicates a linear system... 103

Figure 4.10: Dynamics of the ruthenium sensor presented in the frequency domain. The top and bottom charts show the gain and phase portions of the Bode plot. The middle plot compares the power spectrum of the measured signal to the power spectrum of the noise that is not predictable based on the FIR model. 104

Figure 4.11: Autocorrelation of the measured noise and probability density histogram..... 105

Figure 4.12: Autocorrelation of the prediction error for an ARX model structures with 2 parameters and for a structure with 100 parameters..... 106

Figure 4.13: Measured impulse response at atmospheric oxygen..... 107

Figure 4.14: Oxygen calibration environmental chamber. The oxygen sensor is contained inside the fitting and regulated pressure is measured on an analog gauge..... 108

Figure 4.15: Oxygen partial pressure as measured by the optical sensor is compared with oxygen partial pressure measured using a pressure gauge..... 109

Figure 4.16: Observation of the convergence of the estimated time constant overlaid with error variance for an FIR model fit to a first order decay..... 110

Figure 4.17: Convergence of model parameters for 16 individual measurements at atmospheric oxygen. 111

Figure 4.18: Multiplexing two sensors results in low SNR but model parameters are accurately predicted 112

LIST OF TABLES

Table 2.1: Times required to complete each phase of the pump cycle at an actuation pressure of 40 kPa. These times result in maximum frequency of 85 Hz. When times were set for lower frequencies, phase 1 & 4 were allotted 33% of the total cycle time, phase 2 & 5 used 11% and 3 & 6 used 6%... 28	
Table 2.2: Parameters of various culture systems with comparison to in-vivo. 48	48
Table 3.1: Oxygen concentration and consumption measurements as a function of different flow rates. The final column assumes 0.65 µg protein per channel in the scaffold. Oxygen consumption conversions between various systems assume 110×10^6 cells per gram of liver ⁶¹ and 1 mg protein per 10^6 cells (observations from our laboratory)..... 53	53

1. INTRODUCTION

In vitro models that capture the complexity of human tissue and organ behaviors in a scalable and easy-to-use format are of increasing interest for both technological applications in drug development and in basic biology research¹. Tissues and organs are perfused continuously with blood, which delivers nutrients, oxygen, and macromolecular regulatory molecules. In liver, many biological responses arise from complex interactions between different cell types and vary with position along the capillary bed^{2,3}. Microfluidic platforms that recapitulate the physiological cellular microenvironment of the hepatic capillary bed, with perfusion flow that allows development of physiological oxygen gradients, may be useful in understanding liver toxicity, disease, inflammation, and drug metabolism⁴⁻¹⁵. In vitro culture models that foster local microperfusion with a format that allows accesses to cells and their microenvironment are desirable to a broad research community.

This thesis describes a platform technology that has been developed for studying liver tissue in-vitro. There are several factors that have guided the development of the technology. The first is the desire to create a system that is robust and easy to use. The second is to maximize the function of tissue in the system and the final goal is to make the system amenable to biological interrogation – with the intent of gathering a maximal amount of information from each experiment. The thesis is broken into three primary sections based on the above focus areas. The first section describes the mechanical development of the device with a focus on the pumping system and auxiliary systems. The second section addresses how the system has been designed to optimize the oxygen environment to provide ideal culture conditions for liver. The final section describes sensors that can be used to continuously monitor tissue activity in the device by measuring oxygen concentration.

The first portion of the thesis describes a platform that features an array of bioreactors that foster three dimensional tissue organization under continuous perfusion. Although many types of perfusion

bioreactors for 3D culture have been developed, they are generally limited in throughput and often complicated to use. The approach here adapts 3D models to an easy-to-use, multiwell plate format suitable for higher throughput applications. Ease of use is achieved by designing the bioreactors as an array of open wells covered by a conventional tissue culture lid and by employing docking stations that facilitate handling the perfused multiwell plates. Each bioreactor contains a scaffold that supports formation of hundreds of 3D microscale tissue units. Perfusion through the tissue is achieved using integrated pneumatic diaphragm micropumps. Pulsatile flow from the pumps is filtered using integrated fluidic capacitors such that the flow rate through the scaffold is constant. Pneumatic actuation was selected because it offers significant advantages for operation inside humidified CO₂ incubators maintained at 37 °C, a harsh environment for electrically driven micropumps. Pneumatic actuation permits the necessary electronic timing components to be kept outside the incubator. This arrangement can make perfused multiwell plates inexpensive or even disposable if mass-produced. Additionally, life science research laboratories in academia and industry typically have distributed outlets for vacuum and compressed air which makes sources for pneumatic actuation readily available.

The format of the device mimics the familiar multiwell tissue culture plate. Three dimensional tissue cultures in the perfused multiwell system are initiated by pipetting a cell suspension directly onto extracellular matrix (ECM)-coated scaffolds. Microscale perfusion is started immediately after seeding to control the local oxygen concentration and biomechanical stimuli (i.e., shear stress) during the critical time period of tissue formation. This arrangement addresses some of the issues that have been reported in microscale perfusion systems such as seeding efficiencies and local control of oxygen during the initial static incubation required for cell attachment¹⁶⁻¹⁹.

Oxygen is a key regulator of cell survival and function and thus, its level in cell culture medium must be adequately controlled. One area of focus was to develop a model of oxygen transport and reaction in

the system and used it to predict oxygen concentration gradients across the tissue and profiles in the bioreactor as a function of system parameters (e.g., flow rate, flow direction, and medium volume).

Oxygen concentration at various points in the bioreactor is also a valuable indicator for cellular metabolism and ultimately cell health. One desirable feature for both parsing metabolic function and assessing response to treatments is a real time read out of oxygen tension at key points in the bioreactor. Such added dimension of real time measurement significantly enhances the value of a cue-response experiment such as a liver drug toxicology study.

There is a growing recognition for the value of online monitoring of cell culture environments, particularly in perfused cell culture²⁰⁻²². Optical sensors whose emission characteristics are predictably influenced by the surrounding environment have received a large amount of attention over the past decade²⁰⁻²⁷. These sensors can provide a non-invasive, cost effective means for continuous monitoring of key culture conditions including oxygen, CO₂, and pH²³. Oxygen concentration can be measured by examination of the florescent intensity or decay time of an excited ruthenium complex. Significant advances have been made in development of mechanically and chemically stable materials^{28, 29}, but relatively few developments have been made in the sensing techniques used for measurement.

Currently three measurement techniques are employed. The first is to measure the total emission intensity for a given excitation signal^{22, 24-27}. This method suffers from signal drift, is particularly sensitive to the intensity of excitation and requires frequent re-calibration. The second method is to measure the phase lag between a sinusoidal reference signal and the response signal^{30, 31}. This method is problematic because it assumes that the florescence decay exactly fits a first order exponential decay and only measures phase at a single frequency³². The final method is to excite the material with an impulse from a laser or a light emitting diode (LED) and to measure the response^{20, 33-35}. This method is able to identify the time response to an impulse, but is subject to noise and averaging multiple signals (to

reduce noise) can be a slow process. This thesis describes an alternative approach where sensors excite a layer of ruthenium using a stochastic signal from a (LED). The response is then measured on a photodiode. System identification techniques are used to determine the relevant time constants which are subsequently converted to oxygen measurements. This stochastic method offers several advantages including insensitivity to the intensity of the excitation source, robustness to noise and fast measurement durations.

Coupling of real-time oxygen sensors with a three dimensional perfused model for liver presents a novel culture platform that advances the state of the art for liver research and provides a method for investigating liver related drug toxicities, a major challenge for the pharmaceutical industry. Furthermore, the techniques of measuring fluorescence lifetime using stochastic excitation signals could provide value for continuous sensing of a wide range of environmental and cellular conditions.

2. BIOREACTOR DESIGN

2.1 Concept of multiwell bioreactor systems

The bioreactor provides a culture environment that mimics the in-vivo liver by fostering formation of three-dimensional tissue structures resembling the liver sinusoid. Like the sinusoid, tissue contained in the bioreactor is continually perfused with culture medium. The core of the device is a scaffold (Figure 2.1a) containing a matrix of 3-D liver tissue units that support cell attachment and 3D tissue formation. Culture medium is continually circulated by pneumatic micropumps that are integrated into each well (Figure 2.1b). To enable throughput as well as integration into existing automated cell culture paradigms, the device was designed to mimic the format of a multi-well plate. Open wells facilitate cell seeding, reagent sampling and addition, insertion and removal of scaffolds and oxygen exchange with the environment. Each plate houses 12 isolated bioreactors so multiple conditions can be run in parallel (Fig 2.1c). The 18-mm spacing between bioreactor centers matches the spacing interval of a 96-well plate (9-mm), enabling the use of multi-channel pipettes.

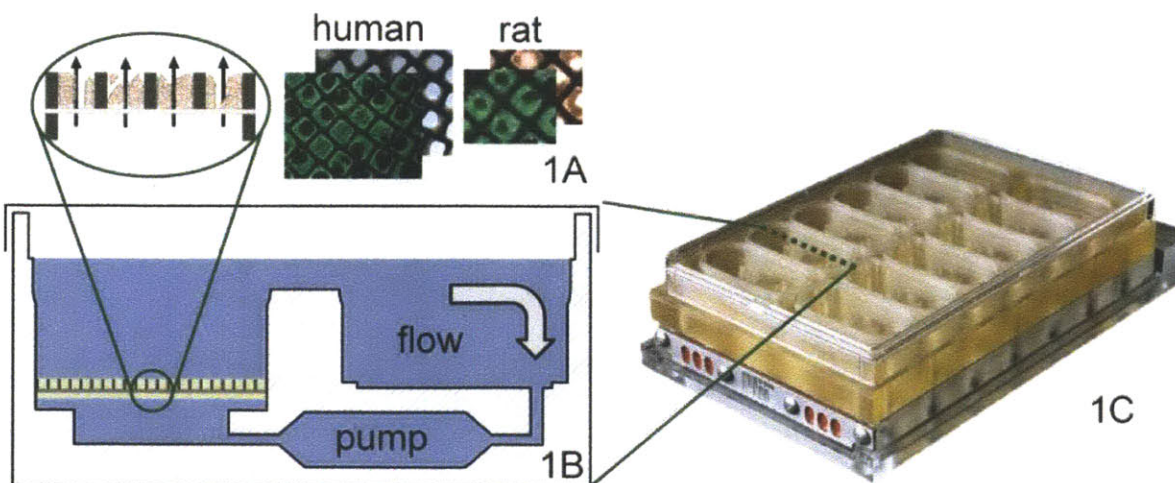


Figure 2.1: A live-dead (green-red) stain of human and rat hepatocytes cultured in the scaffold alongside a schematic cross section (1A). The scaffold resides within a well of the bioreactor (1B), and there are 12 isolated 3-D perfused bioreactors on each culture plate (1C)

Tissue is formed by seeding a suspension of liver cells into a reactor well; the cells adhere to the scaffold contained in the well and form tissue-like structures under continuous perfusion. The bioreactor is housed in a standard incubator and a docking mechanism within the incubator actuates the integrated micropumps. Nine generations of functional multi-well bioreactors have been fabricated and the basic design features of each system are detailed in Appendix A.1.

A scaffold is used to support the 3-D organization of cells. The composition, architecture, and mechanical properties of the scaffold work together to dictate tissue morphogenesis and continued evolution of tissue function. The basic design of the scaffold, figure 2.2, has remained constant throughout several generations of bioreactors^{11, 12, 15, 36}. Briefly, it is a thin wafer with a number of channels (typically 40 to 1,000 depending on design) spanning the wafer. The thickness of the wafer (between 230 and 250 μm) sets the depth of the channel to around 10 cell diameters. The scaffold is coated with extracellular matrix (Collagen Type I, PN: 354236, BD Biosciences, Bedford, MA) and cells attach to the inside walls of the channel. The cross-section of the channel is typically round or rectangular with an area of roughly 0.09 square mm. Each channel holds a 'unit' of tissue, and thus the total amount of tissue in a reactor is easily scaled by the number of channels.

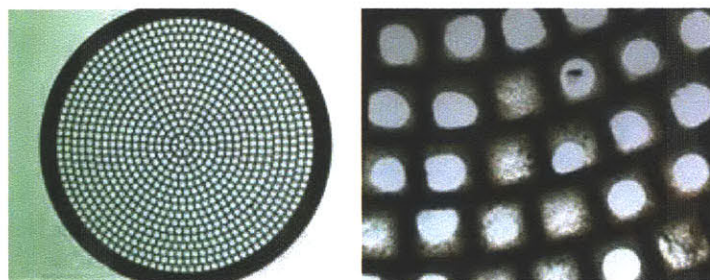


Figure 2.2: (a) The scaffold with no cells and (b) the scaffold with human tissue

A 5 μm pore size filter is placed below the scaffold to capture the cells within the channel immediately following seeding (Durapore, SVLP09050, Millipore, Billerica, MA). A filter support is integrated into the bottom of the reactor well, and the entire assembly is held in place by a retaining ring. Typically 1,000

cells are seeded into the bioreactor per channel in the scaffold, and 0.625 μg of tissue (~ 625 cells) is retained in the channel throughout the duration of an experiment. The scaffold is fabricated by drilling or milling holes in a thin sheet of polystyrene.

A micropump is embedded in each well of the bioreactor so that all bioreactors have self-contained fluidic systems. The pumps are positive displacement with a constant stroke volume set by design. The pulsatile nature of flow exiting the pump is filtered by a fluidic capacitor to produce a constant flow stream at the tissue. The pumps are pneumatically actuated in parallel by a control system that is housed outside the incubator. Pumps, capacitors and auxiliary systems are described in Sections 2.2, 2.3 and 2.4 respectively.

2.2 Pump

The bi-directional micropump features a clamshell-like pump chamber, two active valves and a fluidic capacitor. The contoured shape of the pump chamber used in combination with a thin, flexible membrane reduces actuation pressure requirements and leads to a constant stroke volume. A relatively large stroke volume allows for a high compression ratio and results in a pump that is self-priming and bubble-tolerant. The pump was fabricated by standard CNC machining but is readily amenable to other fabrication and replication techniques such as laser machining³⁷ or micromolding^{38, 39}.

2.2.1 Pump Function

A schematic cross-section of the pumping system is illustrated in figure 2.3. The system consists of a pump chamber, two active valves, and a fluidic capacitor. The pump was made by sandwiching a thin ($\sim 25 \mu\text{m}$), flexible polyurethane membrane between two plates. The top (fluidic) plate contains the top half of the pump chamber, valve seats, and fluidic channels. The bottom (pneumatic) plate contains the bottom half of the pump chamber, the valves, and connections to the pneumatic lines. The membrane

provides a partition between the sterile top plate (containing the cell cultures) and the non-sterile bottom plate (containing the pneumatics). Sealing pressure between the plates was maximized by using narrow bosses in the pneumatic plate around the pump features. Also, a very thin membrane was used to minimize membrane penetration into the pump features. Dowell pins ensure proper alignment of the pump features.

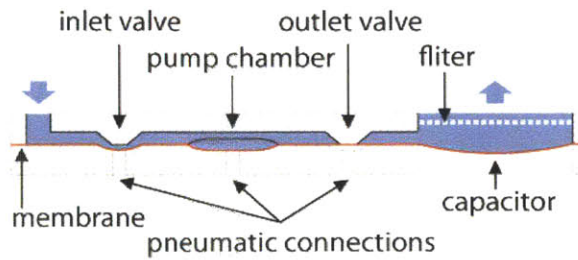


Figure 2.3: Schematic cross-section of the pumping system.

Air pressure drives the pumps by actuating the membrane. A valve is opened when negative air pressure pulls the membrane towards the pneumatic plate. Positive air pressure closes the valve by pressing the membrane against the valve seat in the fluidic plate. The pump chamber fills when negative pressure is applied to the membrane, and drains in response to positive air pressure. Fluid is pumped by opening the inlet valve, filling the pump chamber, reversing the state of the valves and draining the pump chamber. Movement of the membrane between the rigid surfaces of the pump chamber sets the stroke volume. At least one valve is closed at all times to prevent backflow when pumping against a head pressure. The pumping sequence, shown in figure 2.4, can be run in the forward or reverse direction.

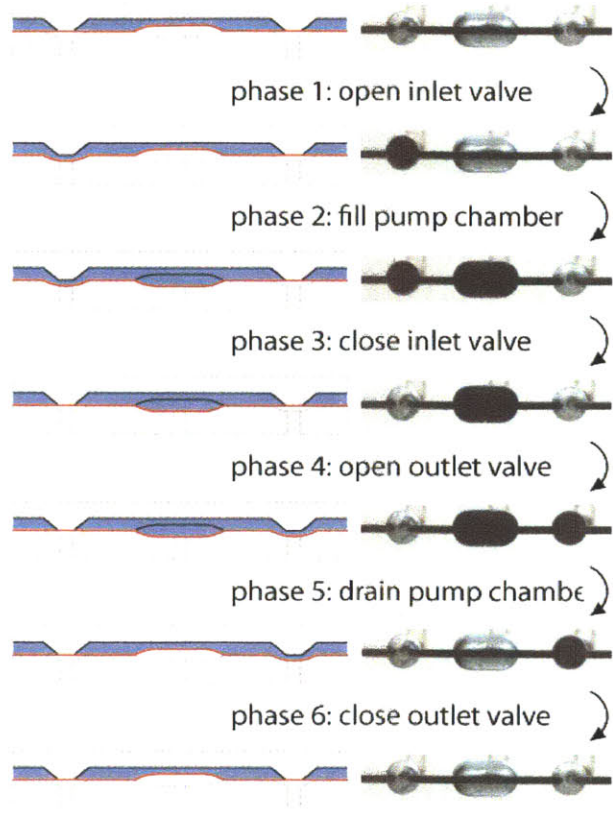


Figure 2.4: Schematic cross-sections and top view photographs of the valves and pump chamber illustrating the pump cycle.

A model of the pump that highlights features made in the top and bottom plates is shown in figure 2.5. The pump chamber has a 1.5 x 1.9 mm footprint and a 1.58 mm radius of curvature. The combined volume of the top and bottom halves of the pump chamber is 0.5 μL . (These dimensions apply to the newest versions of the bioreactor (version H & I) which utilize a scaffold with 300 channels. The pumps in reactors with larger tissue capacity (reactor version A – G) have a footprint of 1.5 x 3 mm and 0.92 μL volume). The valves have a 1.5 mm circular footprint and are 0.3 mm deep with a flat bottom. The fluidic channels have a 0.4 x 0.4 mm D-shaped cross-section. Between each pump feature, a short section of channel is connected with angled drill holes (not shown). This ensures that the membrane cannot deflect into the fluidic channels, and eliminates potential pneumatic connections between adjacent pump features.

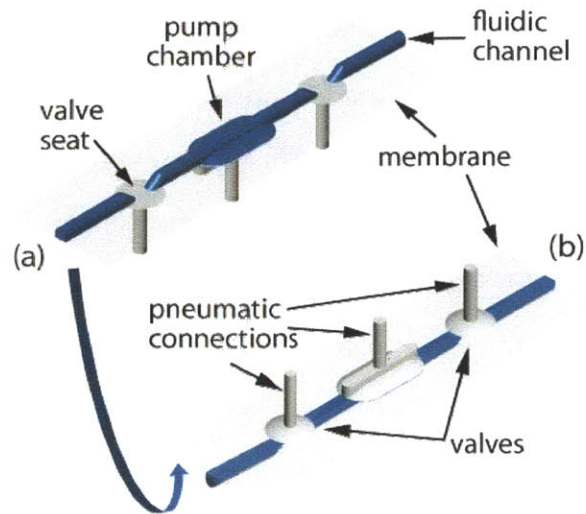


Figure 2.5: A 3D model of the pump elements. Only the volumes filled with fluid (blue) or air (grey) are shown. Both the top (a) and bottom half (b) of the pump features are presented.

In order to maintain a set flow rate, it is essential that a constant volume of fluid is pumped during each cycle. To achieve this goal, actuation pressures are chosen to greatly exceed the expected head pressure (discussed in the following sections). Constant stroke volume is ensured by the contoured surfaces of the pump chamber that limit the maximum deflection of the membrane. Additionally, the fluidic channel was cut across the length of the pump chamber. This prevents the flexible membrane from throttling or closing the outlet of the pump chamber before all fluid is ejected, alleviating problems of valve leakage. Similarly, a small channel in the bottom plate ensures the membrane does not prematurely seal off the pneumatic input when vacuum is applied. These channels significantly improve pump consistency and performance. Because of the large pump stroke volume, these pumps are self priming and bubble tolerant. The tapered ends of the fluidic channels also reduce the possibility of bubble entrapment. The bubble clearing capability of the pump is demonstrated by a sequence of images in figure 2.6.

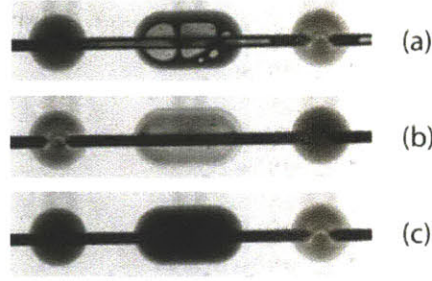


Figure 2.6: The clearance of air bubbles through one complete cycle of the pump. In the first image, the pump is filled with a air bubbles (a). The pump chamber is drained and the bubbles are ejected (b) and the chamber is refilled with fluid (c).

2.2.2 Pump Model

The volume V of a pump chamber with a round footprint is given by the equation for a spherical cap:

$$V = \frac{\pi}{24} \left[16r_p^3 - (8r_p^2 + w^2) \sqrt{4r_p^2 - w^2} \right], \quad (2.1)$$

where r_p is the radius of curvature and w is the diameter of the cap. Since the pump chamber has an obround footprint, its volume increases by:

$$(l - w) \left[r_p^2 \sin^{-1} \left(\frac{w}{2r_p} \right) - \frac{w}{4} \sqrt{4r_p^2 - w^2} \right], \quad (2.2)$$

where w is now the width of the cap and l is the length of the chamber. The additional length term accounts for the middle section between the semi-circular ends.

For a circular chamber, the balance of forces shown in figure 2.7 between pressure P , which acts on the projected area of the chamber, and membrane tension, acting around the circumference of the chamber is:

$$P[\pi(w/2)^2] = \sigma_n(\pi wt), \quad (2.3)$$

where w is the width of the chamber, t is the membrane thickness and σ_n is the component of membrane tensile stress acting normal to a flat membrane. This component of tensile stress can be found using:

$$\sigma_n = \sigma \sin \theta = \frac{\sigma w}{2r}, \quad (2.4)$$

where r is the radius of curvature of the membrane and σ is tensile stress in the membrane. This leads to:

$$P = \frac{2\sigma t}{r}, \quad (2.5)$$

which is analogous to the Young-Laplace equation for pressure inside a spherical droplet where tensile stress in the membrane, the product of σt , represents surface tension.

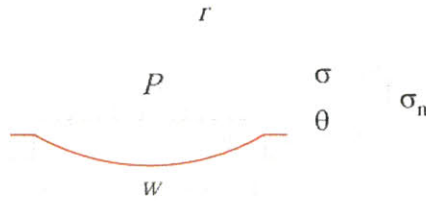


Figure 2.7: A balance of forces between pressure acting on the circular area of the membrane and tension in the membrane acting around the circumference of the membrane.

Sigma is the product of strain ε and the Young's Modulus E ($\sigma = \varepsilon E$). Strain is calculated using:

$$\varepsilon = \frac{l_f - l_i}{l_i} = \frac{2r}{w} \sin^{-1} \left(\frac{w}{2r} \right) - 1, \quad (2.6)$$

where l_i is the width of the chamber (w) and l_f is the length of the chamber surface (the arc length of the membrane). Using (2.5) and (2.6), a relationship between pressure and membrane deflection is found:

$$P = \frac{4Et}{w} \left[\sin^{-1} \left(\frac{w}{2r} \right) - \frac{w}{2r} \right]. \quad (2.7)$$

A Young's Modulus of 15 MPa was measured for the membrane in the described system. Because a thin, flexible membrane is used, only tension is considered, and moment, shear and compression are all neglected.

According to (2.7), in order to deflect a 1.5 mm diameter round membrane to a radius of curvature of 1.58 mm, the pressure differential across the membrane must be approximately 20 kPa. For an obround chamber, strain across the long axis is less than across the short axis. The strain along this axis is given by:

$$\varepsilon_l = \frac{2r}{l} \sin^{-1} \left(\frac{w}{2r} \right) - \frac{w}{l} = \varepsilon \frac{w}{l}, \quad (2.8)$$

where l is the length of the chamber. Estimates for the obround, 3 x 1.5 mm, chamber suggest the minimum actuation pressure drops to approximately 12 kPa. For a 3 x 1.9 mm obround chamber, the actuation pressure should be roughly 16 kPa.

2.2.3 Pump Characterization

Flow from the pump is independent of pneumatic pressure and head pressure within certain limits. Outside these limits, the stroke volume is not set by the size of the pump chamber. The operating range of the pump is the subject of this section. Characterization was performed on the bioreactor version with a pump chamber volume (stroke volume) of 0.92 μL .

Durability

To test the durability of the pump and polyurethane membrane, a system was assembled and operated continuously for six months at a flow rate of 0.2 mL min^{-1} (~ 3.6 Hz). Eight bioreactors were filled with fluid (but without cells) and four were empty (dry). The test was performed on the bench, but identical results could be expected inside the incubator. None of the valves or pumps leaked or failed after the nearly 60 million cycles of the stress test. This demonstrates the suitability of the pumping system for

long-term perfusion culture and shows that the presence or absence of fluid and cells in one well does not affect the operation of adjacent wells on the plate. Therefore, the bioreactor system is amenable to a timecourse experiment where individual wells are terminated at various times.

Pneumatic pressure

The minimum pneumatic pressure required to fully actuate the membrane was determined at a cycle frequency of 5 Hz. This frequency allowed sufficient time for the membrane to actuate. Equal positive and negative pressures were used. A small glass capillary was connected to the exit of the pump, bypassing the capacitor. The capillary was mounted on a ruler and the position of fluid in the capillary before and after 50 pump cycles was measured. The difference in positions was used to determine a fluid volume. Volume measurements, normalized to the number of cycles, are plotted in figure 2.8.

When sufficient pressure was applied, the measured stroke volume was 0.95 μL . This value is very close to the calculated volume of the pump chamber (0.92 μL). Differences in pump chamber volume could be explained by accuracy limitations in the fabrication process or deflection of the membrane into the pneumatic and fluidic channels that span the pump chamber. As predicted by the model, the pneumatic pressure required to fully actuate the membrane was between 12 and 20 kPa.

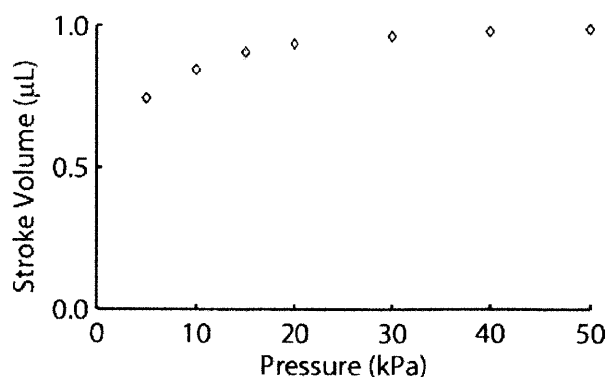


Figure 2.8: Stroke volume in relation to actuation pressure. The pump was driven at 5 Hz.

Phase timing

There are six phases in a cycle of the pump. Complete execution of each phase requires a minimum amount of time and that time was measured. The time required for each cycle was determined by setting the controller to allow excess time for five of the six phases, and the time for the remaining phase was varied. Flow was measured using the methods described previously. The results for draining the pump chamber are shown in figure 2.9.

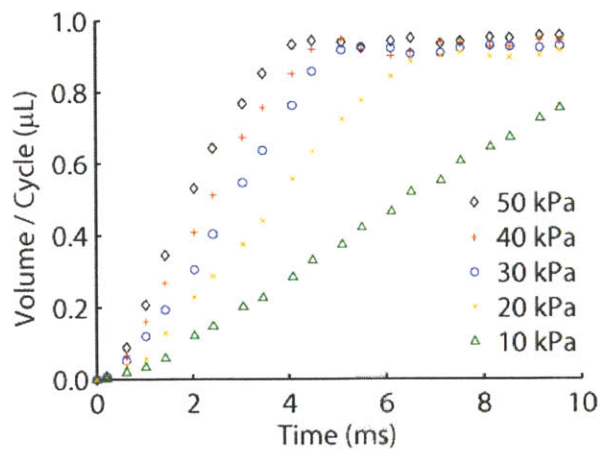


Figure 2.9: Volume of fluid ejected from the pump chamber during phase five of the pumping cycle for various pneumatic pressures.

It can be seen that volume of fluid ejected from the pump chamber increases with time, then plateaus once the entire volume of the pump chamber has been ejected. For a given pneumatic pressure the minimum time for complete actuation of a pump cycle is defined by the inflection point at the plateau. The slopes of these curves represent flow rates from the pump. The highest actuation pressures drove fluid at the fastest rates.

Figure 2.10 shows the time required to fill the pump chamber. As seen in both figure 2.9 and 2.10, the pump response changed only minimally when pneumatic pressure was increased from 30 to 50 kPa. As a result, positive and negative 40 kPa were selected as optimal pneumatic actuation pressures.

The minimum time required for complete actuation of the valves was found in a similar manner. The minimum time required for each phase of the pump cycle is shown in table 2.1.

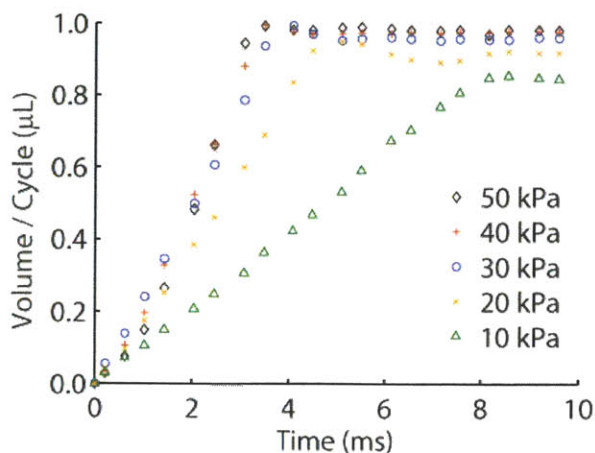


Figure 2.10: Volume of fluid filling the pump chamber during phase 2 of the pump cycle.

Table 2.1: Times required to complete each phase of the pump cycle at an actuation pressure of 40 kPa. These times result in maximum frequency of 85 Hz. When times were set for lower frequencies, phase 1 & 4 were allotted 33% of the total cycle time, phase 2 & 5 used 11% and 3 & 6 used 6%.

Minimum Time	
Step 1: Open Inlet Valve	0.4 ms
Step 2: Fill Pump Chamber	3.7 ms
Step 3: Close Inlet Valve	1.4 ms
Step 4: Open Outlet Valve	0.4 ms
Step 5: Drain Pump Chamber	4.5 ms
Step 6: Close Outlet Valve	1.4 ms

Head Pressure

The relationship between flow and head pressure was investigated. The height of a horizontally mounted capillary was adjusted relative to the pump in order to achieve the desired head pressures. Flow was measured across a range of frequencies for head pressures ranging from 0 to 25 kPa. The results are shown in figure 2.11.

The initial linear slope of this figure signifies a constant stroke volume. Declining flow rates signify that the membrane is no longer conforming to the rigid walls of the chamber and the pump is sensitive to changes in pneumatic and head pressure. Therefore, it is desirable to operate the pumps in the linear

region. At 85 Hz the pump achieves 5 mL/min against zero head. Against a head pressure of 25 kPa, the pump can achieve 2.6 mL/min at 50 Hz. At the lower frequencies, variations in head pressure do not affect the performance of the pump.

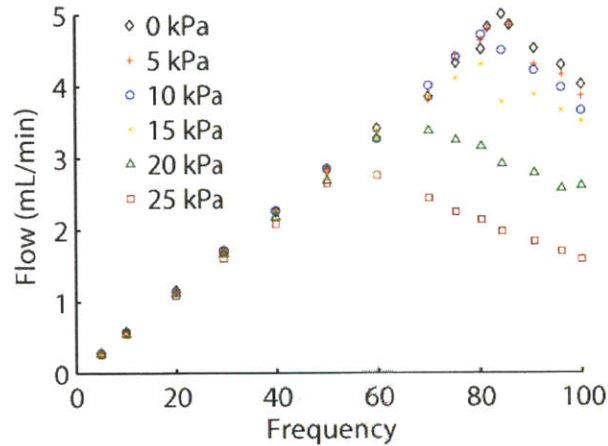


Figure 2.11: Flow rate as a function of frequency and head pressure for a pneumatic pressure of 40 kPa. In typical bioreactor operation, the pump frequency is below 4 Hz (0.2 mL min^{-1}), well within the flow rate thresholds observed here. The hydraulic permeability of the 0.11 mm thick filter is $0.735 \text{ mm s}^{-1} \text{ kPa}^{-1}$ (SVLP09050, Millipore Corp., Bedford MA)¹¹. The filter is the dominant source of fluidic resistance, and under normal operation creates a head pressure of 50 Pa, over three orders of magnitude below maximal achievable pressure. Although head pressure in the system is expected to rise over time as a result of cell debris clogging the filter, increases in pressure of this magnitude are generally undesirable and clogged filters should be replaced before these pressure levels are reached.

2.3 Capacitor

A consequence of designing the pump to operate robustly against an uncertain head pressure is that high actuation pressures generate sharp pulses of flow at the pump exit. A fluidic capacitor converts pulsatile flow from the pump into continuous flow. A representative volume output from one pump cycle is schematically illustrated in figure 2.12. It can be seen that flow occurs in bursts during certain

phases and is zero or negative during other phases. To filter out the pulses and achieve an approximately constant flow, the pump is equipped with a fluidic capacitor.

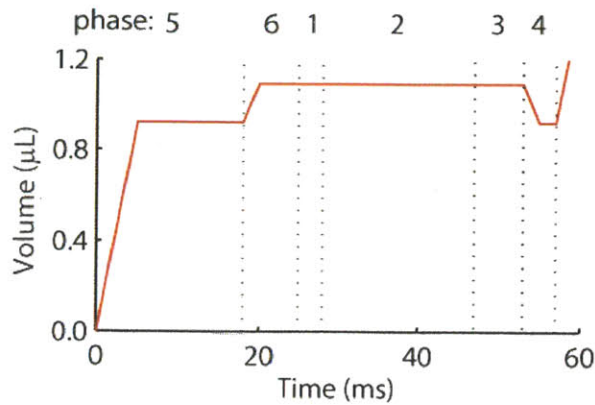


Figure 2.12: Volume output from the pump through one pumping cycle is plotted versus time. Numbers indicate phases of the pump cycle from figure 2.4. Fluid flow in phase five is the result of draining the pump chamber. The smaller volume change in phase 6 and 4 represents draining and filling the exit valve.

The fluidic capacitor is created by allowing a section of the membrane (between the pumps and tissue) to flex. Models for assessing capacitor designs were developed and a parameter indicating capacitor performance was established.

2.3.1 Capacitor Operation

The main components of the fluidic capacitor shown in figure 2.13 are a flexible membrane and a fluidic resistance supplied by a filter. When flow is directed into the capacitor from the pump, there is an increase in fluid pressure within the capacitor which deflects the membrane downward. The capacitor is able to absorb incremental pulses of fluid while maintaining a constant pressure in the chamber. Since it is the fluid pressure in the chamber that drives flow through the resistance, the flow through the filter is approximately constant. Because the membrane can deflect up or down, a capacitor situated between the cells and the pump will filter flow pulses regardless of the direction of flow.



Figure 2.13: A two-capacitor system filters flow pulses both entering (a) and leaving (b) the pump. In (a), lower than atmospheric pressure draws fluid through the fluidic resistor, and in (b) elevated pressures drive flow through the resistor. The bioreactor uses a single capacitor between the pump and scaffold.

2.3.2 Capacitor Model

Fluidic capacitance describes how volume in the capacitor changes in response to fluid pressure:

$$C = \frac{dV}{dP}. \quad (2.9)$$

Fluidic capacitance can be provided with a number of physical devices that can be linear or nonlinear. Examples of linear elements include an open-top reservoir or a closed reservoir with a spring-loaded piston. For membrane capacitors with a high Young's Modulus, capacitance can be modeled as a constant acknowledging the fact that deflection is typically less than the membrane thickness⁴⁰. Examples of nonlinear capacitors include an air bubble inside a closed chamber or flow channels with elastic walls⁴¹. Linear fluidic capacitors are easier to characterize but can be difficult to integrate into a microfluidic system. In contrast, nonlinear capacitors can be easy to implement and can be effective over a larger range of operating conditions. Models for membrane capacitors have been developed; however, they do not account for the actual geometry of the deflected membrane⁴¹⁻⁴³. The following model accounts for the nonlinear relationship between fluid pressure and the geometry of the deflected membrane and for this reason is a more accurate predictor of performance.

The described pump and valves use a thin, flexible membrane. For this reason, it was advantageous to employ the same membrane in the capacitor design. For the described circular capacitor, V and P are defined by (2.1) and (2.7), respectively. Both of these equations are based the assumption that the deflected membrane forms a spherically curved surface.

By taking the derivative of (2.1) and (2.7), capacitance is found in terms of the radius of curvature of the membrane:

$$C = \frac{\pi r^3}{4E} \left(\frac{8r^2 - w^2 - 4r\sqrt{4r^2 - w^2}}{2r - \sqrt{4r^2 - w^2}} \right). \quad (2.10)$$

Ideally, an equation describing capacitance in terms of pressure should be found; however, since r is not readily described as a function of P , this direct equation was not found. Instead, capacitance and pressure values across a range of radii were calculated and plotted for several capacitor diameters. As can be seen in figure 2.14, this capacitor is nonlinear. It is important to mention that pressure shown in this figure is the pressure difference across the capacitor membrane.

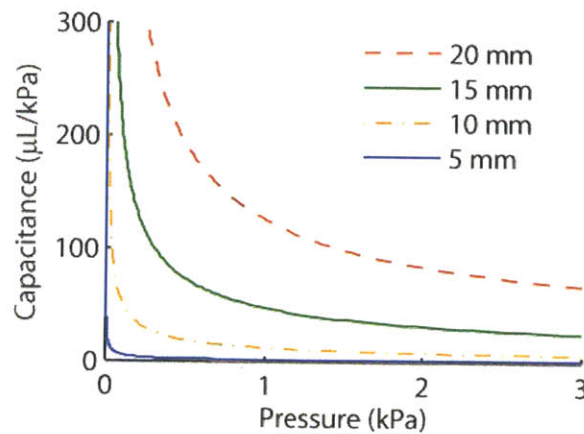


Figure 2.14: Capacitance versus pressure for capacitors of different diameters.

Pressure was calculated by multiplying average flow rate by the fluid resistance of the filter. A value for capacitance was found using this pressure. If there is another significant contributor to fluid pressure, such as hydrostatic pressure, this will cause capacitance values to drop and the following calculations will need to be adjusted. More importantly, if air pressure below the membrane is tuned to match fluid pressure, the pressure difference across the membrane will decrease and capacitance will increase.

The closer the membrane is maintained near the neutral (flat) position, by tuning air pressure under the membrane to match fluid pressure, the higher values for capacitance will be. The willingness of a flat

membrane to deflect under a small pressure (i.e., the large capacitance) is the result of the geometries involved. When the membrane is initially flat, only a small amount of deflection will result in a sizeable change in capacitor volume. As the capacitor is loaded, increasingly larger amounts of membrane strain are required to increase volume in the capacitor region. For example, a very small amount of deflection in terms of membrane strain, 0.04% strain along the centerline of a 10 mm capacitor, will hold a relatively large volume, 5 μL . This small amount of strain requires a small pressure differential, 0.0033 kPa, and thus capacitance is large. When the capacitor is initially loaded with 20 μL , an increase in membrane strain from 0.7% to 1.1% is required to deflect the membrane enough to accommodate an additional 5 μL . This requires an increase in pressure from 0.21 kPa to 0.4 kPa and thus capacitance is much lower. Ten times more strain and over 50 times more pressure are required to deflect the pre-loaded capacitor membrane. Since capacitance is change in volume per change in pressure, this increase represents an order of magnitude decrease in capacitance. If it is feasible to maintain an air pressure below the capacitor membrane that keeps the membrane relatively flat, performance of the capacitor will be significantly increased.

It is useful to briefly discuss other potential capacitor designs. Based on the above discussion it is reasonable to assume that trapping a volume of air below the capacitor membrane would increase capacitance by keeping the membrane closer to the neutral position, but unfortunately this design will have unintended consequences. Trapping an air bubble underneath the membrane is analogous to connecting two capacitors in series, thus the combined capacitance will always be lower than the lowest of the two individual capacitances. Therefore this approach is only valuable if the capacitance of the trapped air is some amount higher than the capacitance of the deflected membrane (assuming the bubble keeps the membrane perfectly flat such that membrane capacitance goes to infinity, the trapped air capacitance simply needs to be higher than the deflected membrane capacitance).

Based on the ideal gas law, the equation for capacitance is

$$C = \frac{P_i V_i}{P^2} \quad (2.11)$$

and the capacitance of a volume of air that fills the space below the capacitor (roughly 500 μL) results in a capacitance of 5 $\mu\text{L kPa}^{-1}$. Since this capacitance is lower than the capacitance of the flexible membrane, the addition of the trapped air capacitor will lower the combined capacitance below either of the two capacitors individually. In order for this method to be valuable, the total volume would need to reach at least around 2 mL (capacitance of 20 $\mu\text{L kPa}^{-1}$).

A final option for potential capacitor designs would be an open top chimney extending up from the fluidic channel between the pump and the scaffold. The capacitance for this linear capacitor is

$$C = \frac{A}{\rho g}, \quad (2.12)$$

where A is the cross sectional area of the chimney. A modest chimney with cross section diameter of 0.8 mm would result in a capacitance of 50 $\mu\text{L kPa}^{-1}$. Although this capacitance is sufficient to filter flow pulses, the height of the chimney is set by the head pressure at the pump. Initially with a debris free filter, the head pressure (50 Pa) only requires the chimney to extend 5 mm above the surface of the fluid. However, if the filter becomes clogged with debris, it is easy to envision that the chimney would soon overflow and flow would bypass the scaffold.

The time constant τ is capacitance times the fluidic resistance of the filter R , 10 $\text{kPa}/(\text{mL}/\text{s})$:

$$\tau = RC. \quad (2.13)$$

The time constant indicates how long it takes a system to respond to an input. If the input is a volume of fluid ejected from the pump into the capacitor, the time constant indicates how long before 63% of this fluid is sent from the capacitor through the fluidic resistor at the system exit. When a capacitor is

used to filter fluctuations in a signal, the time constant should be longer than the period of the longest signal the capacitor is expected to filter. For the described system, the time constant should be longer than the time to pump one cycle.

As flow rate increases, fluid pressure rises. Consequently, the time constant and performance of the capacitor decrease. With higher flows, the cycle time of the pump t_c also decreases. A flow pattern with a shorter cycle time is easier to stabilize because there is less time with no flow between pump strokes. Taking the ratio of τ / t_c allows a comparison between the ability of the system to filter flow pulses and the signal that the system is expected to filter. Figure 2.15 shows calculated values for τ / t_c for several capacitor diameters across a range of flow rates.

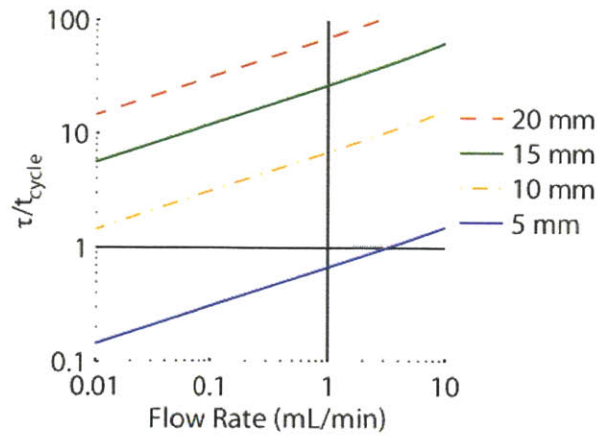


Figure 2.15: Ratio of time constant to cycle time of the pump plotted in log scale across a range of flow rates for several capacitor diameters.

The time constant ratio is dependent on a large number of parameters. A relationship between these parameters was found from the model. Each parameter was varied across a large range and power law regression was used to make correlations between different variables and τ / t_c . An equation was found to estimate this ratio describing flow stability:

$$\frac{\tau}{t_{\text{cycle}}} \approx 0.037 \frac{1}{V_{\text{stroke}}} W^{3.33} \left(\frac{QR}{Et} \right)^{0.33}, \quad (2.14)$$

where Q is the flow rate, R is the fluidic resistance at the capacitor outlet, V_{stroke} is the stroke volume, E is the Young's Modulus of the membrane, t is the membrane thickness and w is the capacitor diameter. For time constant ratios that are relatively close to 1, (2.14) closely estimates the direct calculations from the model. More importantly, (2.14) shows the relative influence of each parameter on τ / t_c , and is a useful tool when designing a pump system for continuous flow applications.

From this equation it can be seen that the diameter of the capacitor has the strongest effect on flow stabilization. The volume of the pump chamber also plays an important role. Flow stability is inversely proportional to the stroke volume. The remaining parameters (Q, R, E, t) impact performance to a lesser extent. This is because when varied they both positively and negatively impact flow stability. For example, when a higher resistance is used to increase the time constant (2.13) and thus increase flow stability, pressure inside the capacitor increases and capacitance is reduced, lowering flow stability. The combined result is only a slight increase in flow stability.

Similarly, when overall flow rate is decreased, the effects on flow stability are both positive and negative. In the described system, the cycle time of the pump must increase in order to reduce overall flow rates. This results in a flow pattern that is more difficult to filter. Coupled with this increase in cycle time is a decrease of pressure in the capacitor region. This reduced pressure positively impacts the performance of the capacitor and partially offsets the negative influence of the increased cycle time. In a study by Yang et. al.^{42, 43}, the effects of average flow and signal frequency were characterized using a system where these two parameters were separable. The results showed that increasing average flow negatively impacts capacitor performance while increasing frequency positively impacts performance. Since flow rate and frequency are coupled when using a reciprocating pump, increased flow will result in only a small net improvement in flow stability.

Flow from the capacitor was modeled using MATLAB. A flow pattern from the pump to the capacitor was constructed using the phases of the pump and the volume of the pump chamber and valves. Flow output at incremental time points was computed based on the input flow pattern. After starting the pump it takes a number of cycles to charge the capacitor. These cycles were not the subject of the simulation. Instead, it focused on operation of the fully charged capacitor.

The simulation begins by estimating the volume of the fully charged capacitor. Using (2.1), the radius of curvature of the membrane is found from this volume. From this radius, the pressure in the capacitor is determined using (2.7). This pressure drives flow through a fluidic resistor at the capacitor exit. Once flows exiting and entering the capacitor are known, a capacitor volume is found for the next time point and the process repeats. The volume of fluid exiting the capacitor is found by integrating flow over time. Comparisons between the model and measured data are shown in the next section.

For a simpler estimation of the flow pattern exiting the capacitor it is also relatively easy to linearize the capacitor model around the average (or maximal) pressure and to generate flows using the single capacitance value.

2.3.3 Capacitor Characterization

Volume of fluid in the capacitor was measured in response to fluid pressures ranging from negative to positive 6 kPa. In these measurements, a capillary was attached to the exit of the capacitor and the valves in the pump were closed. The capillary was raised or lowered to generate hydrostatic pressure in the capacitor and the corresponding volume was recorded. The results are plotted in figure 2.16 and compared with the capacitor model.

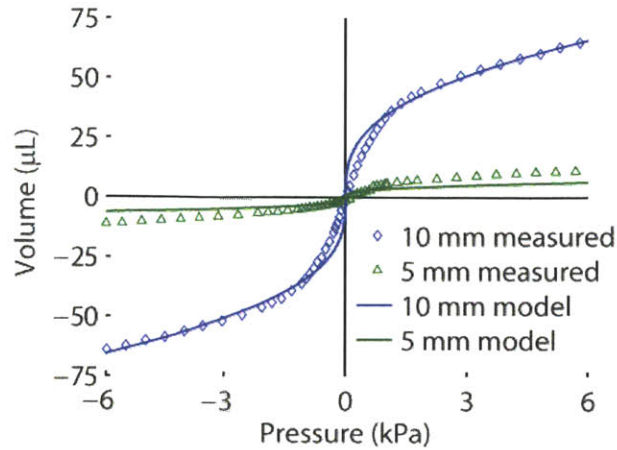


Figure 2.16: Volume displacement of the capacitor versus fluid pressure is compared against the model. Capacitors of two diameters (5 and 10 mm) were measured and modeled.

Fluidic capacitance was calculated from the measured data using central differences. Figure 2.17 compares measured capacitance with the model and shows good agreement especially at higher pressures. At lower pressures, the model underestimates capacitance. These discrepancies can be attributed to stretching the membrane across the capacitor chamber during assembly.

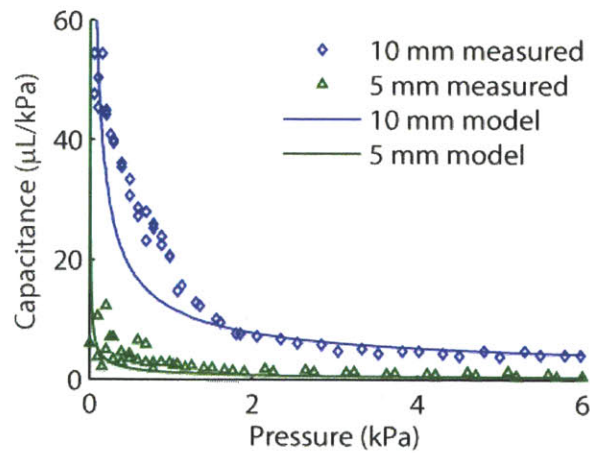


Figure 2.17: Capacitance measurements compared with the model.

In order to measure performance of the capacitor, fluid was pumped through a capillary and a high-speed video camera was used to track the end position of the fluid. A comparison was made between two different capacitor diameters (5 and 10 mm) and no capacitor. The high-speed video camera (Phantom V7.1, Vision Research, Wayne, NJ) was programmed to image at millisecond increments.

Using MATLAB, the end position was tracked and converted into a volume. Since the two capacitors were attached to pumps with slightly different pump chamber volumes (1.17 and 1.08 μL), volume measured from the larger pump chamber was scaled by 0.9 in order to facilitate the comparison of capacitors. The capillary was also attached directly to the pump exit in order to measure a system with no capacitor. Figure 2.18 compares the model with experimental results.

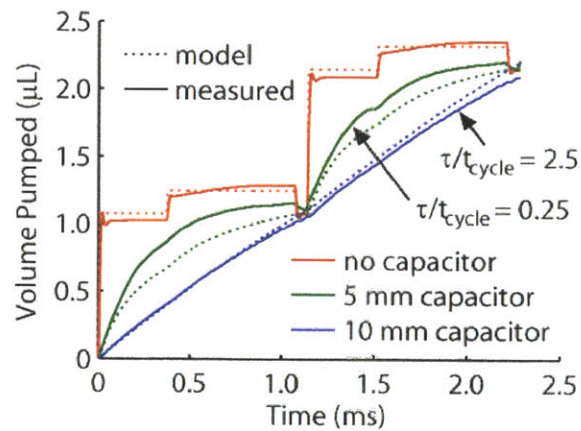


Figure 2.18: Comparison of measured capacitor performance to the capacitor model for a flow rate of 0.05 mL/min. The time constant ratio, estimated using 2.14, is shown for the two capacitors.

As is predicted by the model, the 10 mm capacitor effectively filters fluid pulses and a nearly constant flow stream is generated. The 5 mm capacitor does not completely remove pulses and the model slightly overestimates performance. This could be the result of several factors including differences between the actual fluidic resistance and resistance used in the model.

Figure 2.19 shows measurements for several other flow rates. As τ / t_c increases, flow variations decrease. Using the 10 mm diameter capacitor, fluid pulses have been eliminated from the system for all flow rates. When the 5 mm diameter capacitor is used, flow variations become less pronounced at higher flows. At 2 mL/min, the time constant ratio reaches 0.9 and flow variations are still present. However, when the time constant ratio is increased to 2.5 (figure 2.18) there is a pronounced decrease in flow variations.

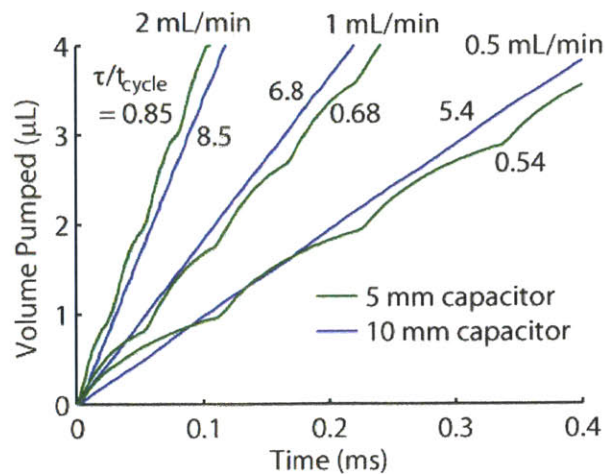


Figure 2.19: Flow from two different capacitors for several flow rates. The time constant ratio from (2.14) is shown for each curve.

2.3.4 Pressure sensing through the capacitor membrane

Since the capacitor membrane deflects in response to fluid pressure, the position of the membrane serves as an indicator of fluid pressure under the scaffold. Sensing the membrane position in real time provides a surrogate indicator that the pumps are running, or could be used to indicate if the filter begins to clog with cell debris.

The challenge is that a non-contact sensor is required. There are a number of options available for optically sensing position that range from lasers to confocal lens configurations. Generally increasing cost is associated with increasing accuracy. One economical method for position sensing uses an infrared (IR) LED and phototransistor, figure 2.20. Light from the LED reflects off a surface and intensity is measured on the photodiode. As the surface moves away from the LED the intensity of reflected light decreases and the signal declines. These sensors are used to measure position of objects in close proximity, and are often used to simply detect the presence or absence of an object.



Figure 2.20: Optical position sensor measures reflected light from a surface. The intensity of light is often correlated with the distance of the surface away from the sensor.

The capacitor membrane is 8 mm from the bottom surface of the reactor. Based on the volume measurements shown in figure 2.16, the center of the membrane is estimated to move up or down with a range of several millimeters. Therefore an optical position sensor with a linear range corresponding to the dimensions of the bioreactor is desired. From roughly 20 different sensors that were tested, one matched the desired range (TCRT 5000, Vishay Intertechnology, Shelton, Connecticut). The ADC readout for the sensor as a function of position is shown in figure 2.21.

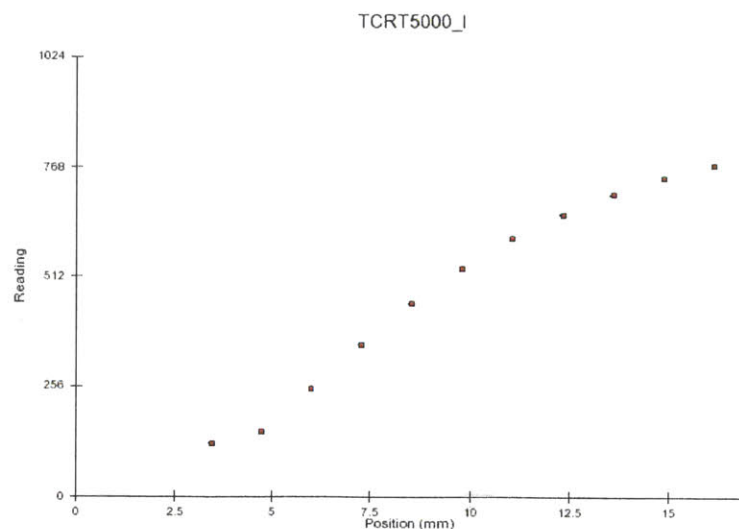


Figure 2.21: Linear range of the Vishay TCRT 5000 matches the desired range for measuring the position of the capacitor membrane during an experiment.

In order to test the performance of the sensor, the output of the pump above the capacitor was connected to a tube and the tube was extended vertically upwards. In this configuration, as fluid is pumped the level of fluid in the tube rises increasing the hydraulic pressure in the capacitor. The test was conducted by initiating the pump and position sensor, and recording the height of the fluid at regular intervals. Results are shown in figure 2.22.

When flow was initiated, a large change in the sensor readout was observed. Thus, the sensor is able to sense that the pumping system is online. The linear increase in fluid height with time indicates a constant flow rate from the pump. When the pressure at the capacitor reached roughly 13 kPa the sensor began to respond indicating that the membrane was moving closer to the sensor. Flow continued at a constant rate and the measurement on the sensor continually increased up to around 20 kPa, at which point the flow rate began to taper off. This indicates that increases in pressure in the system can be detected well before any changes in pressure will impact flow rates. As a frame of reference the pressure required to pump through a clean filter is roughly 50 Pa, several orders of magnitude below pressures where declining flow rates were observed. Since the system is actuated with 40 kPa of pneumatic pressure, and between 12 and 20 kPa are required to actuate the pumping membrane, a decline in flow at 20 kPa is reasonable.

Regular spikes in the position readouts were also observed at elevated head pressures. This could indicate that bursts of small amounts of fluid are leaking from the pump or the connections between the pump and tubing. However, the bioreactor is not designed to operate at these pressure levels, and through using a position sensor operating pressures can be monitored non-invasively in real-time. Further, pressure excursions out of range can be detected before system performance is compromised.

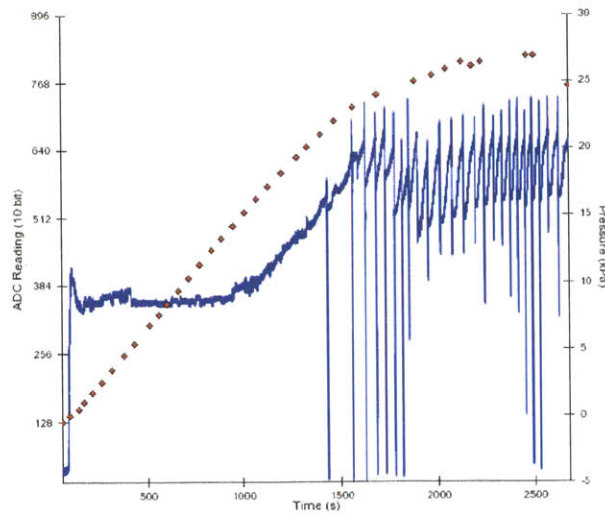


Figure 2.22: Evaluation of the position sensor response to increasing head pressure.

2.4 Auxiliary Systems

Pneumatic signals are distributed in parallel to all 12 pumps by three pneumatic lines (Fig. 1b). The lines interface with the controller through a docking station. Connectors in the docking station have spring-loaded shutoff valves (TFFD01, Colder Products Company, St. Paul, Minnesota) that automatically close when the reactor is removed. This prevents discharge of non-sterile air into the incubator or tissue culture hood and introduction of the humidified air from the incubator into the pneumatic system. Flexing membranes at the ends of the pneumatic lines indicate proper connections and functioning pneumatics (figure 1C, red membranes). Compressed air and vacuum are sourced from laboratory distribution outlets. Air is filtered, dried with desiccant, and regulated to 40 kPa. The pneumatic lines run from the docks to small electronic controllers outside the sterile environment.

2.4.1 Controller

An electronic controller, figure 2.23, actuates three solenoid valves (SMC S070B-6CC, SMC Corporation, Noblesville, Indiana) that output pressure and vacuum signals to the pump chamber and two pump

valves. The pressure and vacuum are regulated to +/- 40 kPa using Airtrol pressure and vacuum regulators (R-900-10-W/K and V-900-30-W/K, Airtrol Components, Inc. New Berlin, Wisconsin). The timing and sequence of the solenoids are controlled by an Atmel microcontroller (ATMega-88, Atmel Corporation, San Jose, California). Seven-segment displays and LEDs indicate the current operating mode of the pumps. The user interfaces to the controller through a series of buttons housed on a custom membrane switch (Technigraphics, Inc., Hunt Valley, MD). The circuit board was manufactured by Advanced Circuits (Aurora, CO).



Figure 2.23: Control panel for operating 3 bioreactors.

2.4.2 Imaging / Assay Plate

There are several endpoint assays for which the perfused bioreactor is not suitable and scaffolds must be placed in a static well. An assay plate was developed, figure 2.24, that has several advantages for these applications. The assay plate has a clear bottom which is ideal for high resolution inverted microscopy. Additionally, scaffolds are placed in fixed positions on the plate so they can be analyzed with a plate reader or an automated image acquisition system. Finally, the scaffolds are elevated from the bottom of the well to enhance oxygen exchange with the atmosphere. While this culture condition is not ideal, it can be used for assays that require the cells to remain viable for several hours.



Figure 2.24: Imaging / assay plate containing 24 wells.

2.5 Fabrication, Sterilization and Assembly

The majority of parts were fabricated by CNC machining. These include the polysulfone fluidic plate, the black Delrin covers for pneumatic indicators, the acrylic pneumatic plate, docking station and assay plate. Polystyrene scaffolds were fabricated by CNC microdrilling. Polypropylene retaining rings, PVDF filters (SVLP09050, Millipore Corp., USA) and silicone membranes for the pneumatic indicators were fabricated by punching, and the polyether aromatic polyurethane membrane (ST-625FS, Stevens Urethane, USA, and MT 2001, American Polyfilm, USA) was cut by laser machining. Solvent bonding was used to seal the pneumatic lines in the pneumatic plate. Sterile polystyrene multiwell lids were purchased from Corning, USA. The 127.8 x 85.5-mm footprint of an assembled perfused multiwell complies with standard dimensions of the 96-well microplates established by the Society for Biomolecular Screening⁴⁴.

Several methods were used for sterilizing the parts. The polyurethane membrane was sterilized using ethylene oxide. The fluidic plate, filters and retaining rings were autoclaved. The polystyrene scaffolds were soaked in 70% ethanol for 30 minutes. Following ethanol sterilization, scaffolds were rinsed in 1x phosphate buffered saline (PBS) then coated with collagen. After 2 hours in a 30 $\mu\text{g mL}^{-1}$ solution of collagen type I (rat tail, BD Biosciences, USA) in 1x PBS, the scaffolds were air-dried in a sterile dish.

PVDF filters for the reactor wells were coated in 1% bovine serum albumin (Sigma, USA) in PBS for 30 minutes.

The pneumatic plate and fluidic plate were assembled with screws tightened to 0.12 N m by a power torque driver. The screws were fitted with Belleville disc springs to provide constant sealing pressure on the thin membrane for the duration of an experiment. The bioreactors were primed with culture medium. After priming the reactor wells were fitted with filters and scaffolds secured by tightly-fitting retaining rings.

2.6 Design Parameter Selection

Cell numbers

The critical design feature of the bioreactor, around which all other parameters are chosen, is the mass of tissue contained in each well. While it is important that each well contains sufficient tissue for routine assays, minimizing the number of cells per well is important because of the high costs of human cells (~\$75 per million fresh hepatocytes), and the low efficiency of harvesting liver non-parenchymal and mouse hepatocytes.

Seeding 800 channel scaffolds with 0.8 million hepatocytes typically results in harvesting 500 µg of total protein¹⁵ or 20 µg RNA at the end of an experiment (non-published results). Among several assays routinely performed (imaging, toxicity (ATP), and gene expression), gene expression requires the largest tissue sample. Since a pharmaceutical collaborator requires 5 to 10 µg RNA for a panel of gene expression studies, a scaffold with 300 channels was selected. Assuming similar tissue yields relative to the quantity of cells seeded, a 300 channel scaffold should yield 7.5 µg of RNA.

Pump Chamber Size

The number of channels in the scaffold sets a range of flow rates that the pumps must achieve. The operating range of the pump was targeted to span the range of physiological and pathological flows observed in vivo. Shear stress in the liver sinusoid in vivo has been reported between 10 and 50 mPa⁴⁵. With a flow rate of $0.2 \mu\text{L min}^{-1} \text{channel}^{-1}$, shear stress in the scaffold is estimated to remain below 30 mPa. A flow rate of $0.2 \mu\text{L min}^{-1} \text{channel}^{-1}$ translates to $60 \mu\text{L min}^{-1}$ for a 300 channel scaffold system. The maximum diameter of the capacitor is also set by the size of the scaffold, as a round 300 channel scaffold will have a diameter of 8 mm. Since the performance of the capacitor degrades rapidly with diameter (equation 2.14), it is desirable to minimize the size of the pump chamber in order to offset the degradation in capacitance. However, with an increasingly smaller pump chamber, variations in the manufacturing process become more pronounced. A pump chamber volume of $0.5 \mu\text{L}$ was selected in order to balance capacitor performance with manufacturing consistency. Based on historical manufacturing results, less than 10% variation in pump chamber volume is expected. The time constant to cycle time ratio for this configuration is 3.2, which is comfortably above the previously mentioned cutoff of 1.0.

Bioreactor Volume

The ratio of medium volume to tissue mass is important for many reasons. This volume dictates how rapidly medium nutrients will be depleted, and how quickly byproducts will accumulate. It influences the concentration of signaling molecules that are secreted from the cells and therefore impacts the functionality of the tissue. When studying toxicology, some drugs become toxic only as a byproduct of metabolism (e.g. acetaminophen). Since the rate of accumulation is set by the total volume of culture medium, the manifestation of these toxicities may only occur when there is a high cell to volume ratio. Conversely, cells have proteins that are protective against some other toxicities (e.g. glutathione). Since the volume of medium also sets the total quantity of a drug given a certain concentration, with a high

cell to volume ratio, the protective proteins may be able to eliminate all of the toxic insult without a manifestation of toxicity, whereas when the cell to volume ratio is low, the toxicity of these compounds could be magnified.

Since the goal of any in-vitro system is generally to model the in-vivo situation, an obvious choice of ideal cell to volume ratio is what is found in the body. Since there are roughly 200 billion hepatocytes in a human liver, and there is 5L of blood – there are roughly 40 million cells per mL blood. This translates to 7.5 μ L of culture medium for the 300 channel scaffold system, clearly an unrealistic target. Table 2.2 shows the cell density and culture volume for various systems, also including some additional parameters.

Table 2.2: Parameters of various culture systems with comparison to in-vivo.

	Well Area (cm ²)	Vol Cap. (mL)	Culture Vol (mL)	Cells Seeded (k)	Cells Retained (k)	Density k cells / mL	Medium Height (mm)
96 well plate	0.32	0.37	0.10	75	9.6	96	3.1
48 well plate	0.75	1.40	-	-	-	-	-
24 well plate	2.00	3.50	0.35	350	60	171	1.8
12 well plate	3.80	6.00	-	-	-	-	-
6 well plate	9.60	15.5	1.00	500	300	300	1.0
800 Channel RXR	1.33		4.00	800	450	113	-
300 Channel RXR	0.50		1.5	300	170	113	-
Human – Blood	-	-	5,000	-	200,000M	40,000	-
Human – Plasma	-	-	3,000	-	200,000M	66,667	-
Rat – Blood	-	-	15	-	1,200M	80,000	-
Rat – Plasma	-	-	10	-	1,200M	120,000	-

Based on the above parameters, the fluid volume of the system was minimized with some constraints. The required volume for the pumping system is roughly 200 μ L, 75% of which is required for the free movement of the capacitor membrane. This volume is not directly accessible by pipette aspiration, but can be exchanged by flushing medium through the pumps. The second constraint on reducing system

volume results from oxygen requirements. The oxygen environment is also an important design parameter and is the subject of the following chapter. The surface area of the air-liquid interface directly influences the oxygen absorption capacity of the system ($Q = hA\Delta C$), and this area has been set to 460 mm^2 . Because of surface tension, it is not possible to maintain a depth of medium across this surface with an average depth below 2 mm, therefore the required volume for oxygen exchange is roughly $920 \text{ }\mu\text{L}$. Finally, when cells are seeded into the bioreactor, they are pipetted into the well above the scaffold. Roughly $200 \text{ }\mu\text{L}$ of cell suspension is used for seeding, which should all fit within the well above the scaffold, otherwise cells will be seeded in undesirable locations in the bioreactor. With this volume set to roughly $350 \text{ }\mu\text{L}$, the total volume of the system becomes 1.5 mL , with roughly 85% directly accessible by pipette.

2.7 Discussion

The approach in developing the pump was to first address the reliability requirements, then to filter the flow pulses using a fluidic capacitor. Robustness of the pump was achieved by using pneumatic pressures that reliably deflected the membrane to the contoured surfaces of the pump chamber. Flow rate can be varied across a large range by simply changing the pump frequency. The capacitor diameter is then chosen to filter fluctuations across the desired flow range.

The construction of a pumping system that can be integrated into a standard cell culture plate, can reliably operate across a wide range of flow rates insensitive to changes in head pressure, can pump indefinitely, and outputs a continuous, pulseless, flow pattern represents a significant advancement for flow based tissue culture. The described pump has enabled the transition from tissue culture systems which require a myriad of standalone pumps, culture chambers, reservoirs and connectors, to a system where all of these components can be integrated in an array format that is familiar to all experimental biologists.

3. OXYGEN ENVIRONMENT

Oxygen tension is a critical parameter in regulating tissue function⁴⁶⁻⁵⁰. Since the oxygen environment in the bioreactor is strongly influenced by scaffold design, flow rate selection, and well geometry, an understanding of these parameters is a prerequisite for creating an oxygen environment that promotes cell health and differentiated liver function. This section combines theoretical and experimental work in characterizing the oxygen environment and its influence on cellular function.

3.1 Oxygen Consumption

The functional unit of the liver in-vivo is the sinusoid shown in figure 3.1. The sinusoid is composed of parallel plates of hepatocytes, the primary liver cell type, lined with sinusoidal endothelial cells, stellate cells, Kupffer cells and other non-parenchymal cell types. The vast majority of blood supply to the liver (75 to 80%) is poorly oxygenated venous blood from the intestines with a small portion arterial blood from the hepatic artery⁵¹. As blood flows along the sinusoid oxygen is consumed by the cells, creating a gradient of oxygen concentration within the sinusoid^{2, 52, 53}. Oxygen consumption rates, concentration of many liver enzymes and the level of liver functions also vary with position along the sinusoid^{2, 3, 47, 49, 53-58}.

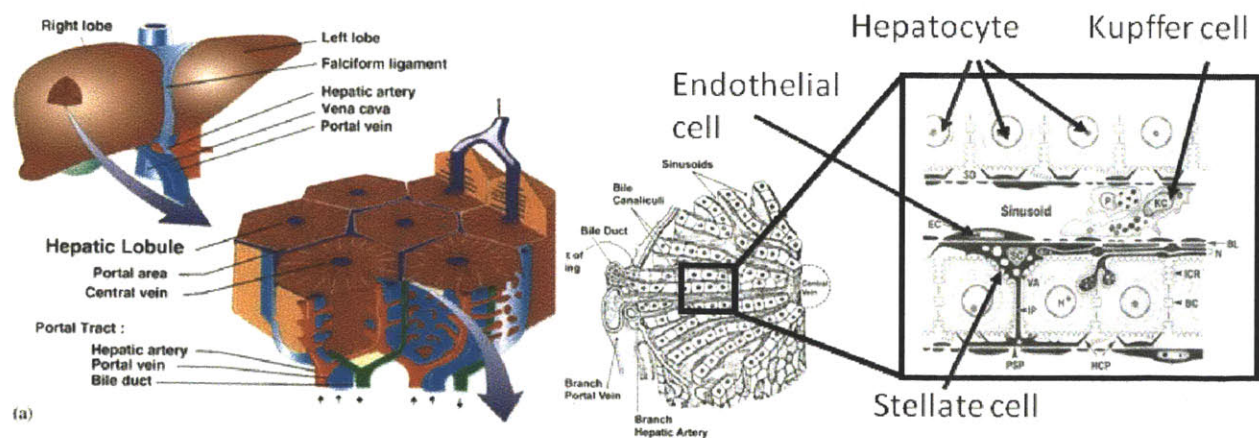


Figure 3.1: Structure of liver, from whole liver on the left to the liver sinusoid on the right^{59, 60}.

Glucose and oxygen are the two primary substrates consumed in the metabolic pathway for the production of energy in cells. There are six molecules of oxygen consumed for each molecule of glucose. Considering that the concentration of glucose in cell culture medium is 1 to 10 millimolar and the maximum solubility of oxygen in culture medium is over 60 times lower (below 200 micromolar), oxygen is by far the most rapidly depleted nutrient from medium. Fortunately, the surrounding environment continually supplies oxygen to the bioreactor. A balance between this constant depletion and reoxygenation of medium is important for a successful cell culture.

3.1.1 Preliminary Oxygen Measurements

Preliminary oxygen concentration measurements were taken to understand basic parameters governing oxygen consumption and absorption into the system. Oxygen concentration in the culture medium was measured optically using commercially available probes¹⁵. Fiber optic probes were strategically placed in the bioreactor above the scaffold and in the reservoir as shown in figure 3.2 so that the change in oxygen concentration across the scaffold could be observed. During the first 8 hours of culture flow is directed downwards through the scaffold allowing time for the cells to attach. During this time, the probe located above the scaffold measures the average concentration of medium entering the scaffold and the probe in the reservoir measures oxygen concentration in medium exiting the scaffold. No oxygen exchange takes place as medium passes through the pump. Following an initial attachment phase, the flow direction is reversed and maintained in an upward direction through the scaffold for the duration of culture. At this time, the oxygen probe in the reservoir measures concentration entering the scaffold and the oxygen probe above the scaffold measures concentration exiting the cells.

Primary rat hepatocytes were seeded into the bioreactor based on protocols that have previously been described¹⁵. Measured values of dissolved oxygen in the reactor and reservoir wells during the first 20 hours of culture are shown in figure 3.3. The culture medium is air-saturated at the time cells are

seeded in the bioreactor. After downward flow through the scaffold is initiated ($0.3 \mu\text{L channel}^{-1} \text{min}^{-1}$), consumption by the cells causes oxygen concentration to decline for several hours until equilibrium is reached between consumption and oxygen absorption at the air-liquid interface. The oxygen concentration below the scaffold C_B (corresponding to the oxygen concentration measured in the reservoir) reached a steady state value of $\sim 60 \mu\text{M}$ with a corresponding oxygen concentration above the scaffold C_A of $145 \mu\text{M}$.

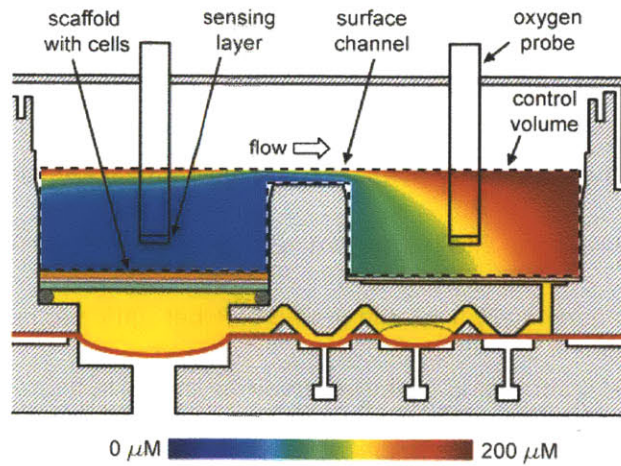


Figure 3.2: Oxygen probes are sketched as black rectangles above the scaffold (left) and in the reservoir (right). The fluid is colored to show an expected distribution of oxygen throughout the bioreactor when flow is directed up through the scaffold. This simulation is discussed in detail later in the chapter.

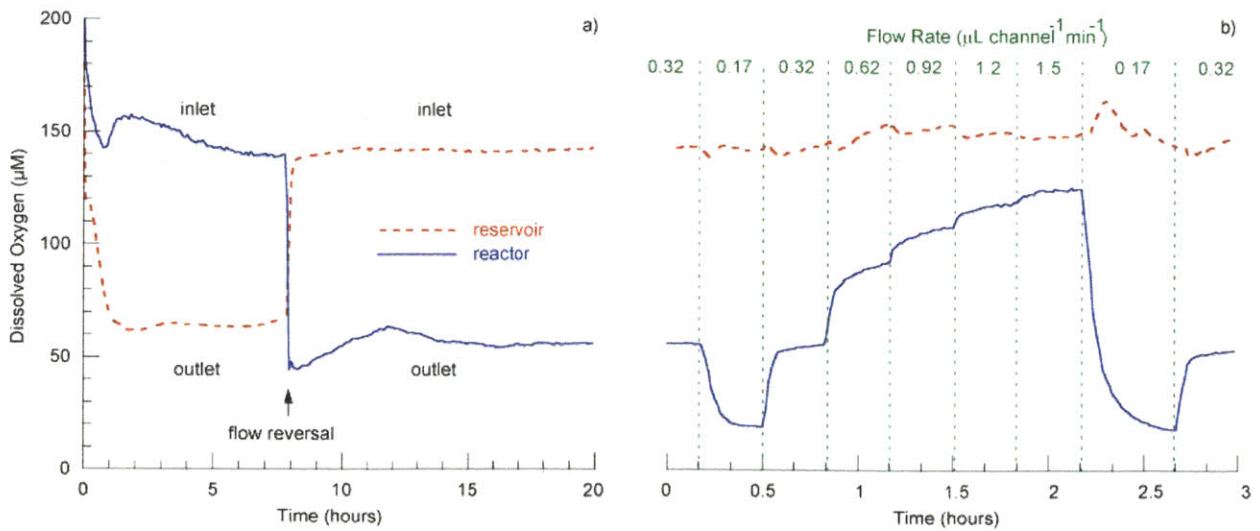


Figure 3.3: Measured concentration of dissolved oxygen in reservoir and reactor wells seeded with rat hepatocytes: (a) As a function of time post seeding with a flow rate of $0.3 \mu\text{L channel}^{-1} \text{min}^{-1}$ and a

sampling interval of 5 minutes. (b) As a function of flow rate (immediately following the time course measurement) with a sampling interval of 1 minute.

After 8 hours of an attachment phase, the flow direction was reversed while maintaining a flow rate of $0.3 \mu\text{L channel}^{-1} \text{ min}^{-1}$. Immediately following the flow reversal, oxygen-depleted medium below the scaffold and in the reservoir was passed directly back through the cells. During this time (~10 minutes) the cells were exposed to relatively low inlet concentrations, and a concomitant drop of ~25% in the outlet concentration was observed with a longer transient (~2 hr).

To estimate cellular oxygen consumption rates in this perfused culture, inlet and outlet oxygen concentrations were measured as a function of flow rate. Following the initial 20 hours plotted in figure 3.2a, flow rate was incrementally changed as shown in figure 3.2b. Table 3.1 shows the concentration readings for each flow rate along with the measured oxygen consumption.

Table 3.1: Oxygen concentration and consumption measurements as a function of different flow rates. The final column assumes $0.65 \mu\text{g protein per channel}$ in the scaffold. Oxygen consumption conversions between various systems assume 110×10^6 cells per gram of liver⁶¹ and $1 \text{ mg protein per } 10^6$ cells (observations from our laboratory).

Flow Rate $\mu\text{L min}^{-1} \text{ channel}^{-1}$	Concentration		Consumption	
	C_B (μM)	C_A (μM)	$\text{pmol s}^{-1} \text{ channel}^{-1}$	$\text{pmol s}^{-1} \mu\text{g prot}^{-1}$
0.17	142	19	0.35	0.54
0.32	144	56	0.47	0.72
0.62	153	91	0.64	0.99
0.92	153	108	0.69	1.06
1.2	150	119	0.63	0.97
1.5	149	125	0.61	0.94
Arterial O_2 ^{47, 62}	104 – 146			
Entering Liver ^{47, 62}	84 – 91			
Exiting Liver ^{47, 62}		42 – 49		
Isolated Hepatocytes ⁶³				0.69
Perfused Rat Liver ⁶⁴				0.5
Perfused Rat Liver ⁵³				0.28

The observed inlet oxygen concentration fluctuates modestly around $\sim 145 \mu\text{M}$ while oxygen concentration downstream of the tissue increases with increasing flow rate, from $\sim 19 \mu\text{M}$ to $\sim 125 \mu\text{M}$.

In human, the reported in vivo perivenous region (sinusoidal exit) dissolved free oxygen concentration is

42–49 μM ⁴⁷. Measured concentration in the bioreactor at a flow rate of $0.3 \mu\text{L channel}^{-1} \text{ min}^{-1}$ is $\sim 50 \mu\text{M}$, hence this flow rate provides a reasonable approximation of physiological oxygen. Although oxygen concentration entering the tissue is higher than values reported for the human in vivo periportal region (84–91 μM), it is within arterial blood oxygen concentration ranges (104–146 μM) and below hyperoxic levels⁴⁷. Gradients are steeper than those in vivo because culture medium does not contain hemoglobin, which serves as a depot of oxygen.

From the concentration measurements, total oxygen consumption rates within the scaffold can be found. Assuming a steady state, mass conservation requires that

$$\dot{m}_{\text{cells}} = Q(C_B - C_A) = \oint_V R dV, \quad (3.1)$$

where C_B and C_A are the oxygen concentration below and above the scaffold, Q is the flow rate and $\oint_V R dV$ is the local consumption integrated over the volume of tissue. Observed consumption levels are comparable with reported oxygen consumption rates for isolated hepatocytes, and are slightly higher than levels reported for whole liver^{53, 63, 64}.

While these initial measurements provide crude insight into the bioreactor oxygen environment, they do not provide resolution for understanding oxygen gradients in the scaffold microenvironment, or of convection patterns in the surrounding bioreactor. Several different models have been used to better understand these aspects of the oxygen environment.

3.1.2 Convection-Diffusion Reaction Equations

Oxygen transport can be described using the convection diffusion equation,

$$\frac{\partial C}{\partial t} = -\mathbf{v}\nabla C + D_{O_2}\nabla^2 C - R \quad (3.2)$$

where C is oxygen concentration, \mathbf{v} is the local fluid velocity, D_{O_2} is the diffusion coefficient of oxygen, and R is a reaction term describing the local consumption rate. The diffusion coefficient of oxygen depends on temperature and the medium it is diffusing in. Oxygen diffusion in water at 37 °C is between, $3.0^{65,66}$ and $3.4^{67} \times 10^{-3} \text{ mm}^2 \text{ s}^{-1}$, and diffusion in tissue is between 1.8^{66} and $2^{68,69} \times 10^{-3} \text{ mm}^2 \text{ s}^{-1}$. Diffusion coefficients of 2×10^{-3} and $3.2 \times 10^{-3} \text{ mm}^2 \text{ s}^{-1}$ are used depending on the medium of interest.

By normalizing all of the terms in the original equation, then dividing through by the appropriate concentration and time scale, several important dimensionless terms appear. These include the Peclet number

$$Pe = \frac{vL}{D}, \quad (3.3)$$

which relates convection to diffusion and Damkohler number

$$Da = \frac{Lk_0^{n-1}}{v} \quad (3.4a)$$

Zero Order: $Da = \frac{Lk_0}{vC_{max}} \quad (3.4b)$

First Order: $Da = \frac{Lk_1}{v} \quad (3.4c)$

Michaelis-Menten: $Da = \frac{LR_{max}}{vC_{max}} \quad (3.4d)$

relating reaction to transport (assuming transport is dominated by convection). The three ratios represent different types of reactions (zero order k_0 , first order k_1 , and Michaelis-Menten kinetics R_{max}). Using these constants, the dimensionless form of the mass transport equation with a Michaelis-Menten reaction becomes

$$\frac{\partial C^*}{\partial t^*} = -\mathbf{v}^* \cdot \nabla^* C^* + Pe^{-1} \nabla^{*2} C^* - Da \frac{C^*}{k_m^* + C^*} \quad (3.5)$$

where the * denotes that a parameter has been normalized by a characteristic scale of the problem. The formation of dimensionless numbers and intermediate steps between 3.2 and 3.5 are shown in Appendix A.2. Using these dimensionless terms a number of transport processes within the bioreactor can be understood. Also, using the dimensionless transport and reaction equation, finite differences models can be used to gain a further understanding of the oxygen environment in the bioreactor.

3.1.3 Scaffold model

Convective transport to the scaffold

The bulk transport process for oxygen delivery to the scaffold is shown in figure 3.4. Oxygen diffuses down from the air liquid interface to the scaffold, and is transported by convection through the pump up to the scaffold. Inspection of the Peclet number for this environment shows that oxygen transport to the scaffold is dominated by convection in the liquid and diffusion from the air-liquid interface is negligible. The appropriate length scale here is the depth of the scaffold below the air-liquid interface. The velocity is the fluid velocity normal to the surface of the scaffold, or the flow rate divided by the scaffold surface area ($\pi/4 d^2 \approx d^2$). Using these parameters the Peclet becomes,

$$Pe = \frac{(Q/d^2)h}{D_{O_2}}, \quad (3.6)$$

where D_{O_2} is $3.2 \times 10^{-3} \text{ mm}^2 \text{ s}^{-1}$, d is 8 mm for a 300 channel scaffold, Q is $1 \mu\text{L s}^{-1}$ for a 300 channel scaffold and h is 6 mm. The Peclet number for this configuration and flow rate is nearly 30 which indicates that transport of oxygen to the tissue is dominated by convection.

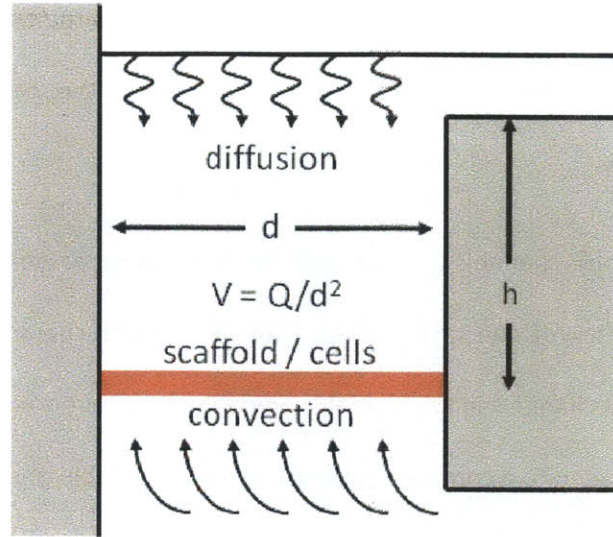


Figure 3.4: Schematic of bulk oxygen transport length and velocity scales to the scaffold for comparison of diffusion to convection using the Peclet number.

Oxygen transport plays an important role in the total measured reaction rate

Given the relative importance of diffusion from the air-liquid interface is low, total delivery of oxygen to the scaffold is calculated using the flow rate Q and inlet concentration C

$$\dot{m}_{flow} = QC. \tag{3.7}$$

For a typical set of operating conditions, 150 μM oxygen entering the scaffold at a flow of 0.32 $\mu\text{L min}^{-1}$ channel⁻¹, the delivery of oxygen to the scaffold is 0.8 pmol s^{-1} channel⁻¹. This value sets an upper limit on consumption by the tissue. Interestingly, this value is only slightly above the maximum measured consumption 0.7 pmol s^{-1} channel⁻¹ shown in table 3.1. Hence, oxygen consumption is likely influenced by both the intrinsic metabolic activity of cells in the channel and by the capacity of the system to provide oxygen.

1D cylindrical diffusion and consumption within the channel

Once oxygen is delivered to the scaffold, a portion is consumed by the tissue and the rest passes through the scaffold. Oxygen transport and reaction process within the tissue in the scaffold will influence the ratio of oxygen that is consumed versus what simply passes through the scaffold. Oxygen

is convected to the tissue surface but must diffuse from the surface of the tissue through several layers of cells in order to provide nutrients for the entire tissue mass. This presents a second potential limitation to oxygen delivery.

When cells are seeded into channels in the scaffold they form tissue structures that although constrained by the geometry of the channel have an amorphous character. Figure 3.5 shows a representative image of ~20 channels in the scaffold. Since there are hundreds of channels in a scaffold, these irregularities are averaged to a constant but imperfectly predictable phenotype.

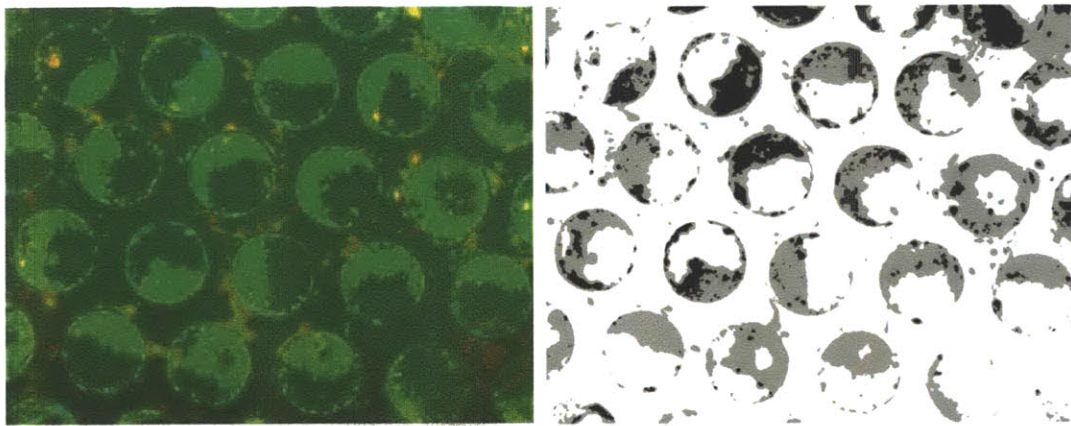


Figure 3.5: A representative image of a scaffold looking down into the channels. This image shows a variety of common tissue structures. The left hand image shows live cells stained green and dead cells stained red. The image on the right shows the same cells, but is analyzed to find the average cross section of the flow path in the channel.

Tabulating the cross-sectional measurements from the 21 channels shown in the image, the average cross-section of the clear area is found to be 0.04 mm^2 equivalent to a $230 \text{ }\mu\text{m}$ diameter circle. The standard deviation of the equivalent diameters is roughly $45 \text{ }\mu\text{m}$, with a range from $150 \text{ }\mu\text{m}$ up to $300 \text{ }\mu\text{m}$. Comparing the average area with the cross-section of the $340 \text{ }\mu\text{m}$ diameter channels and assuming the tissue to be $200 \text{ }\mu\text{m}$ deep, the average volume of tissue in a single channel is estimated at roughly 10 nL . For reference, on average $0.65 \text{ }\mu\text{g}$ protein is retained per channel in the scaffold¹⁵.

Although individual tissue architecture varies, a single channel in the scaffold was modeled as a cylindrical annulus where cells adhere to the walls of the channel and form a ring of tissue with constant thickness. Assuming that convective transport to the surface of the tissue is not limiting results in a constant oxygen concentration at the cell surface on the inside of the ring (this assumption is re-visited in the following section). Since no oxygen diffuses through the plastic scaffold, this surface is insulated. This model reduces to one dimensional diffusion and reaction in cylindrical coordinates.

In eukaryotes, oxygen is reduced to water in an enzymatic reaction which drives the production of chemical energy (in the form of adenosine triphosphate, ATP). A simplistic model of this enzymatic reaction uses Michaelis-Menten kinetics

$$-\frac{dC}{dt} = \frac{R_{max}C}{k_m + C}, \quad (3.8)$$

where the rate of oxygen depletion is related to the maximal volumetric consumption rate R_{max} by a nonlinear function of the local concentration of oxygen. (Typically R_{max} is denoted V_{max} , but R is used to avoid confusion with fluid velocity v and volume V). k_m , the inverse enzyme affinity constant, describes the concentration under which the reaction will proceed at a maximum rate. For oxygen in mitochondria this concentration is very low, between 1 and 5 μM ^{2, 3, 52, 53, 56, 63, 70, 71}. Although significantly higher values of k_m have been reported for tissue, these increases are likely artifacts from measuring concentration outside the tissue. Since a concentration gradient is required for oxygen flux into the tissue, concentration within the tissue will necessarily be lower than concentration measured outside the tissue. Because diffusion is handled explicitly it is appropriate to use the k_m measured for mitochondria. Combining one dimensional cylindrical diffusion with a Michaelis-Menten reaction leads to

$$\frac{\partial C}{\partial t} = D_{O_2} \frac{1}{r} \frac{\partial}{\partial r} \left(r \frac{\partial C}{\partial r} \right) - \frac{R_{max}C}{k_m + C} \quad (3.9)$$

where C is the concentration of oxygen and r is the radial position in the channel. Since this equation is nonlinear with concentration, it is easiest to solve a discrete equation using finite differences. A discrete grid with 20 equally spaced nodes is shown in figure 3.6.

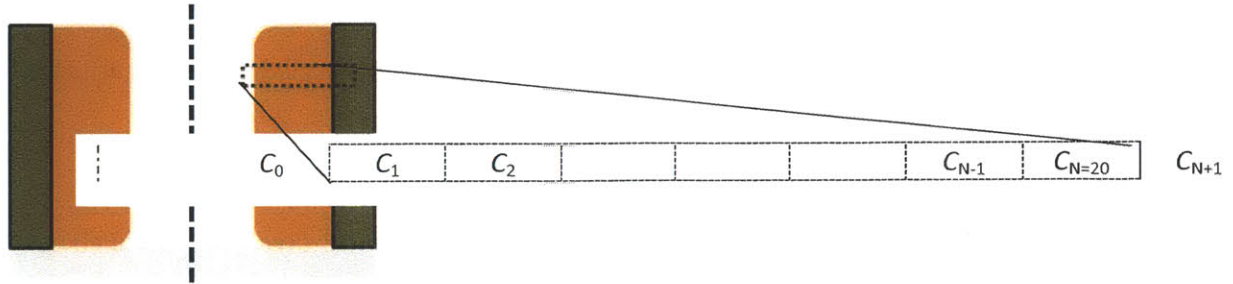


Figure 3.6: Grid layout for finite differences estimation of oxygen consumption in a channel of the scaffold. Concentration estimates are found at equally spaced intervals along the radius of the tissue in the channel. The concentration at the fluid-tissue interface is fixed.

Each of the internal nodes is solved using the discrete equation

$$C_p^{t+1} = C_p + \Delta t \left[D \left(\frac{(r_w+r_p)C_w - (r_w+2r_p+r_e)C_p + (r_p+r_e)C_e}{2r_p\Delta r^2} \right) - \frac{R_{max}C_p}{k_m+C_p} \right], \quad (3.10)$$

where C_w and C_e represent discrete points to the left (west) and right (east) of a center point C_p . A fixed concentration is used for the boundary condition of the inside wall, so the average of C_0 and C_1 is held constant ($C_0 = 2C_{wall} - C_1$). The interface between the tissue and the channel is insulated thus the concentration gradient between $C_{N=20}$ and C_{N+1} must be zero ($C_{N+1}=C_N$). Consumption is nonlinear so it is not possible to set up and solve a system of equations (with $dC/dt = 0$), therefore iterations in time are required. An arbitrary initial concentration is used, and the model iterates using forward differences until steady state is reached. Further details of this simulation along with corresponding Python code is provided in appendix A.3. Results for the concentration profile as a function of total tissue mass (as determined by the annulus inner diameter) are shown in figure 3.5. R_{max} is assumed to be $60 \mu\text{M s}^{-1}$ (or $60 \text{ pmol s}^{-1} \mu\text{L}^{-1}$), k_m is $2 \mu\text{M}$ and the diffusion coefficient is $2 \times 10^{-3} \text{ mm}^2 \text{ s}^{-1}$.

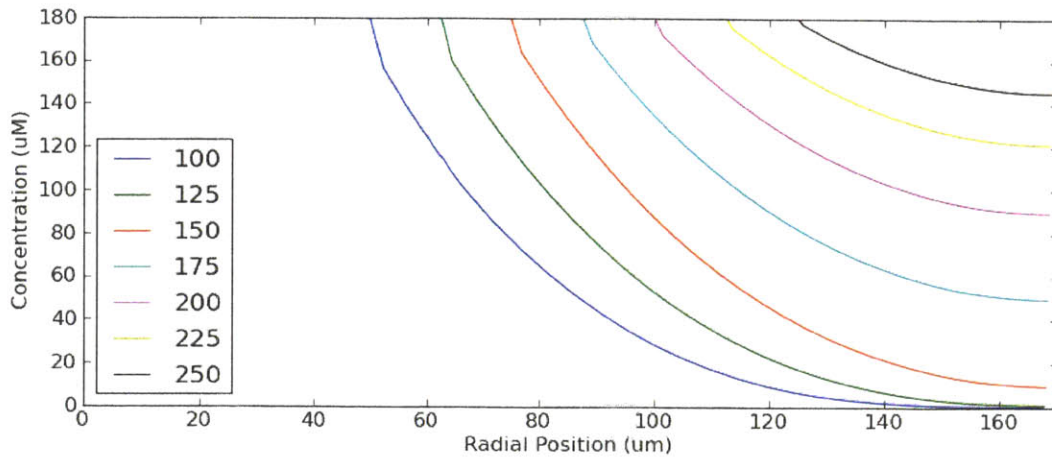


Figure 3.7: Distribution of O_2 concentration in a simplified model of a channel in the scaffold. Channel diameter is $340\ \mu\text{m}$. The different lines represent different inner diameters of the tissue annulus. The legend shows annulus diameter in microns. O_2 Concentration at the tissue surface is $180\ \mu\text{M}$.

Total consumption can be determined by integration of equation 3.1 on a discrete grid. Consumption as a function of tissue mass is shown in figure 3.8 with the height of tissue in the channel assumed to be $200\ \mu\text{m}$. Seen in this figure, total consumption generally increases with the amount of tissue contained in the channel.

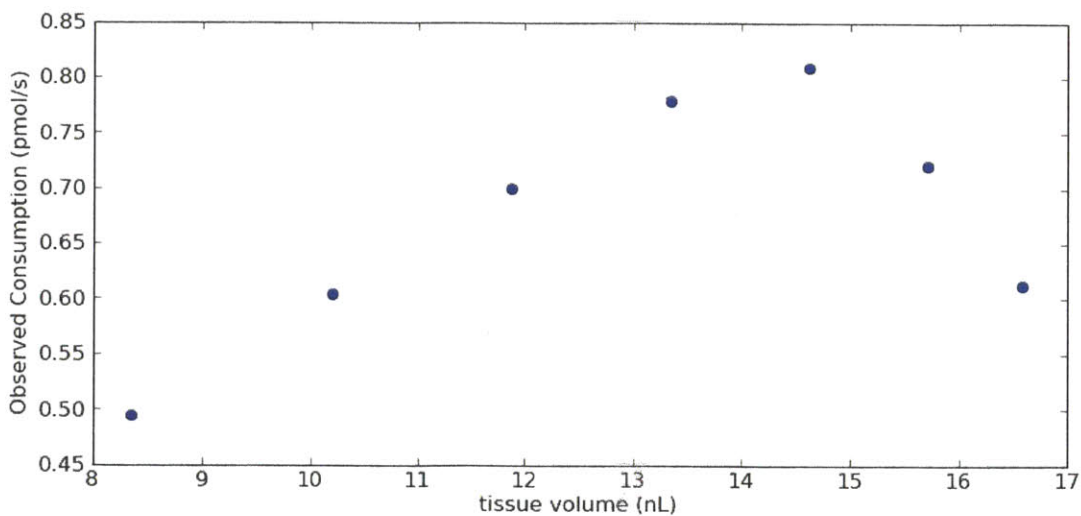


Figure 3.8: Total oxygen consumption increases with increasing tissue volume until diffusion limitations restrict oxygen transport to the outside edge of the channel. Values were obtained by integration of equation 3.1 for a channel height of $200\ \mu\text{m}$.

However, as the inner diameter of the annulus decreases to the point where diffusion does not adequately deliver oxygen to the entire thickness of the tissue, decreasing the inner radius will decrease the volume of tissue that oxygen is delivered to. It would seem to present a serious complication to interpretation of bulk oxygen consumption measurements if increasing the tissue mass could truly decrease consumption. However, the true system is self limiting, as cells deprived of oxygen do not survive.

The oxygen concentration in figure 3.7 shows that oxygen can be delivered to roughly the first 100 μm of tissue before concentration falls below $\sim 5 \mu\text{M}$. This corresponds to an inner diameter for fluid flow of roughly 150 μm and agrees with the experimental range of observed channel diameters shown in figure 3.5. Although reducing the inner diameter of the tissue beyond this limit increases the tissue volume in the model, the surface area available for oxygen transport is reduced, and consequently the volume of tissue that is supplied with oxygen is also reduced. This phenomenon is illustrated in figure 3.9. It is important to realize that although oxygen delivery in the true system is self limiting in this respect, different channel geometries will exhibit different limitations to diffusion.

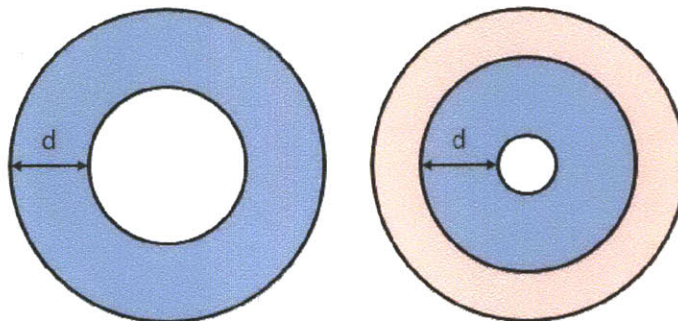


Figure 3.9: Increasing the amount of tissue in the channel beyond oxygen diffusion limits (denoted by d) effectively reduces the volume of tissue that is provide with sufficient oxygen. Although the total volume of tissue (denoted by blue and red color) is greater in the channel on the right, the volume of tissue with adequate oxygen supply, shown in blue, is greater for the channel on the left.

Based on this analysis the last two points in figure 3.8 can be ignored and consumption rates remain positively correlated with tissue volume.

Seen in figure 3.8, the maximal consumption rate is roughly 0.8 pmol s^{-1} . This consumption rate is the same rate that was calculated earlier for the total oxygen delivery to the scaffold. Since it is unreasonable to expect that convection transports oxygen entering the scaffold to the surface of the tissue with 100% efficiency, both convection transport to the scaffold and diffusion limitations within the scaffold will influence observed oxygen consumption rates.

2D cylindrical convection, diffusion and consumption

In order to analyze combined convection diffusion and consumption, the one dimensional model was extended to two dimensions and convection was added. This simulation first models the local flow profile within the channel, then simulates mass transfer using the flow field, diffusion and consumption parameters. Simulations were performed across a wide range of input parameters channel geometry, flow rate, metabolic rate and inlet oxygen concentration.

The model first calculates the flow profile from Navier-Stokes and continuity equations. The Navier-Stokes equations were solved on a staggered rectangular grid by breaking the equations up into substeps⁷². The simulation iterates forward in time until the flow profile stabilizes. Details of this model are provided in Appendix A.4. Once the flow profile is known, a mass transport and reaction are simulated using the same method that was described in the previous section with the addition of convection and a vertical dimension. The addition of convection and second dimension adds several terms to the mass transport equation,

$$\frac{\partial c}{\partial t} = -\left(v_r \frac{\partial c}{\partial r} + v_z \frac{\partial c}{\partial z}\right) + D \left(\frac{1}{r} \frac{\partial}{\partial r} \left(r \frac{\partial c}{\partial r}\right) + \frac{\partial^2 c}{\partial z^2}\right) - \frac{R_{max}C}{k_m + C} \quad (3.6)$$

The primary difference in analyzing this equation on a discrete grid is that when the first derivative terms (for convective transport) are computed for two adjacent nodes, the resulting derivative is centered on the edge between the two nodes. The solution in this scenario is to take the derivative

between the point of interest and the adjacent node on the up-stream side in terms of local velocity. In other words, if flow is moving from left to right and the concentration gradient is desired at some node C_p , this derivative should be evaluated using the concentration difference between C_p and the point to the left rather than between C_p and the point to the right. This technique is called upwinding.

The results of three simulations are shown in figure 3.10. As expected, oxygen concentration does vary with vertical position in the scaffold as well as horizontal position away from the fluid path. This gradient along the flow path is analogous to the gradient of oxygen in the liver, although the gradient here is steeper because there is no hemoglobin in the medium.

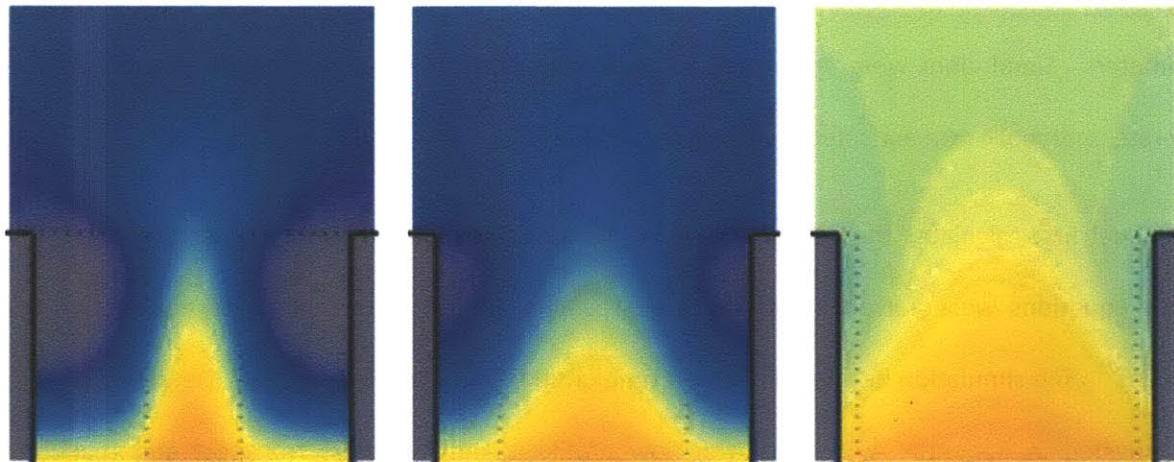


Figure 3.10: Simulation of consumption within one channel of the scaffold. The images show cross-sections of the circular channels. Dotted lines depict where tissue is contained in the scaffold. Fluid flow is constrained to the center of the channel where no cells reside. The colormap shows the concentration of oxygen. The model uses polar coordinates so is an axi-symmetric 3D representation.

An attempt was made to correlate bulk consumption rates with different flow rates, geometries, consumption parameters and oxygen inlet concentrations, but given the number of different parameters that influence total oxygen consumption it was not possible to find a simple relationship governing bulk oxygen consumption as a function of metabolic activity, tissue mass, flow rate and inlet oxygen concentration.

Flow patterns in the filter below the tissue were also simulated. These simulations use Darcy's law instead of Navier-Stokes because the hydraulic permeability of the filter is low. Although analysis is not presented here, information about the simulation is provided in the Appendix A.5.

3.2 Formulation of interfacial absorption analysis

A complete analysis of the absorption of oxygen into the culture medium involves transport from the environment of the incubator into the space between the lid and the surface of the bioreactor, gas transport to the air-liquid interface and transport from the air-liquid interface into the culture medium.

Transport of oxygen into the space above the bioreactor is governed by

$$\dot{m} = D_{O_2-air} \frac{A}{l} (\Delta C), \quad (3.10)$$

where D_{O_2-air} is the diffusion coefficient of oxygen in air ($23 \text{ mm}^2 \text{ s}^{-1}$ at 37° C), A is the cross-sectional area of the space between the lid and the walls of the bioreactor and l is the length oxygen must diffuse along this cross-section. The total resistance to oxygen diffusion is $\sim 2 \times 10^{-3} \text{ s } \mu\text{L}^{-1}$. Assuming 12 individual bioreactors contained in each plate, and 800 channel scaffolds in each bioreactor with $0.6 \text{ pmol s}^{-1} \text{ channel}^{-1}$ oxygen consumption, the required change in concentration between the incubator environment and the space underneath the bioreactor lid is roughly $10 \text{ } \mu\text{M}$. If there are 300 channels in the scaffold a concentration difference of $4 \text{ } \mu\text{M}$ will drive sufficient oxygen transport rates. Since this change in concentration is low, oxygen absorption into the bioreactor is governed by mass transfer in the culture medium and a constant concentration near saturation C_{sat} at the air-liquid interface is assumed.

3.2.1 Non-dimensionalization of mass transport inside the bioreactor

Similar to oxygen consumption in the tissue, oxygen absorption in the bioreactor is a complicated process that is influenced both by diffusion and convection. Before launching into computer simulations

it is important to understand the underlying processes and the different driving forces for oxygen absorption.

Cell culture medium continually flows in a loop through the bioreactor, figure 3.1. Oxygen depleted medium exiting the scaffold flows across a surface channel where medium is exposed to air in the incubator. During this time oxygen diffuses into the medium and is subsequently transported away from the air-liquid interface. Oxygen rich medium is mixed as it flows through the micropump and into a chamber below the scaffold. Oxygen is consumed by the cells as medium passes through the scaffold.

Oxygen concentration is measured above the scaffold and in the reservoir. Oxygen measurements in the reservoir give the concentration after oxygen absorption into the system has stopped (for a Lagrangian fluid element) but before oxygen is consumed by the tissue. Oxygen concentration in the center of the reservoir is equal to the oxygen concentration below the scaffold C_B within 5%. Oxygen measurements above the scaffold C_A show concentration immediately following oxygen consumption by the tissue. These concentrations will stabilize once there is a balance between the quantity of oxygen consumed by the cells and the ability of the bioreactor to absorb oxygen before medium flows back to the scaffold. Therefore, both the oxygen consumption and absorption process will influence the measured concentrations in the system.

Oxygen absorption into the bioreactor is driven by cellular consumption. This creates a concentration gradient between oxygen saturation at the air-liquid interface and the concentration of oxygen exiting the scaffold. The geometry of the system, the flow rate of medium and the diffusion coefficient of oxygen in medium (for a given temperature) will also influence oxygen absorption.

It is readily apparent that at steady state, total oxygen absorption into the system \dot{m}_U is equal to total oxygen consumption by the cells \dot{m}_C and that both are equal to the product of flow rate Q and the concentration difference between the reservoir well and above the scaffold

$$\dot{m}_a = \dot{m}_c = Q(C_B - C_A). \quad (3.11)$$

However, since oxygen absorption is driven by the low concentration of oxygen exiting the scaffold, total oxygen absorption is not independent of the metabolic state of the tissue. In order to eliminate the influence of the tissue, concentration is normalized using

$$\theta = \frac{C - C_A}{C_{sat} - C_A}, \quad (3.12)$$

where the concentration of fluid exiting the scaffold (inherently the lowest concentration in the system) is pinned to zero and the highest concentration in the system (oxygen saturation) is pinned to one. Thus if the dimensionless concentration of oxygen in the reservoir is found θ_B , C_B can be anticipated for any set of C_A and C_{sat} . This dimensionless concentration, which is defined here as the absorption potential ϕ , describes how close the medium comes to saturation as it passes across the surface channel

$$\phi = \frac{C_B - C_A}{C_{sat} - C_A}. \quad (3.13)$$

The oxygen absorption potential represents the percent return of oxygen depleted medium to saturation and is fully specified by geometry, flow and the oxygen diffusion coefficient. Using ϕ , total oxygen absorption into the system becomes

$$\dot{m}_a = Q\phi(C_{sat} - C_A). \quad (3.14)$$

Although $(C_{sat} - C_A)$ is clearly influenced by the metabolic state of the tissue, the absorption potential is only influenced by operational aspects of the bioreactor. When the flow rate is increased, the time for a fluid element to flow across the surface channel is reduced, limiting the time available for the fluid to regain oxygen saturation. Increasing the flow rate reduces the oxygen absorption potential but does not reduce total oxygen absorption because, for a given concentration gradient, total absorption is the

product of flow rate and absorption potential. The depth of culture and the surface area of the air-liquid interface will also influence oxygen absorption.

Analysis of the convection mass transport equations is useful in understanding the absorption potential.

Convection of oxygen is governed by

$$\frac{\partial C}{\partial t} = -v\nabla C + D_{OM}\nabla^2 C \quad (3.15)$$

where v is the fluid velocity field and D_{O_2} is the diffusion coefficient of oxygen in medium. Proper scaling of this equation results in

$$\frac{D\theta}{Dt} = 1/Pe \nabla^2 \theta \quad (3.16)$$

where bold face indicates a normalized value and the Peclet number is the ratio of the characteristic length multiplied by the characteristic velocity to the diffusion coefficient of oxygen in medium. The material derivative (indicated by capital D) incorporates the convection term by following an element of fluid. The equation states that during the time of transport through the region where oxygen absorption occurs, the total change in the dimensionless concentration (defined here as the oxygen absorption potential) is a function of the inverse of the Peclet number. The remaining task is to normalize the length and time scales using the characteristic length and velocity.

The characteristic length for a problem involving diffusion is generally the length over which a substance is expected to diffuse, therefore it is reasonable to select the depth of the surface channel shown in figure 3.1. The relevant velocity for the problem is the velocity component normal to the free surface, represented by the flow rate divided by the surface area. (The tangential velocity is irrelevant if there is never any movement away from the air-liquid interface.) Using these quantities to scale the governing equation, the Peclet number is found to be

$$Pe = \frac{(Q/A_{\text{surface}})\delta}{D_{O_2}}, \quad (3.17)$$

where δ is the depth of the surface channel. The identical result is obtained by scaling the dimensionless time directly from equation 3.15. Using this method, the depth is used to scale the diffusion term and the dimensionless time is found by dividing the volume of the region involved in oxygen transport (the surface area multiplied by the surface channel depth) by the flow rate. An increase in the surface area or the diffusion coefficient will increase the oxygen absorption potential, and conversely an increase in the flow rate or surface channel depth should decrease the oxygen absorption potential. (Remember, increasing the flow rate doesn't decrease the total mass transfer, only the oxygen absorption potential. The oxygen absorption potential indicates how much oxygen can diffuse into a fluid 'particle' as it is transported around the bioreactor, and the oxygen absorption potential is multiplied by the flow rate and concentration gradient to find the total oxygen absorption).

3.3 Oxygen absorption modeling for finding oxygen absorption potential

Oxygen transport and consumption were simulated with a 2D finite differences model that accounts for a variable depth in the third dimension. To understand the model development, consider the path of fluid flowing clockwise in figure 3.1, starting at the bottom of the reservoir. Fluid velocity exiting the reservoir is constant due to a high-impedance filter; however, the oxygen concentration varies with position. As fluid passes through the pump it is completely mixed. Oxygen transfer into culture medium through the low-permeability polyurethane membrane can be neglected. The mixed concentration is calculated from flux across the reservoir filter. Thus, fluid enters the lower face of the scaffold (i.e., scaffold inlet) at a uniform concentration C_B . Fluid velocity entering the scaffold is also uniform due to a filter below the scaffold. Oxygen is consumed by the cells as fluid passes upward through the scaffold. As fluid progresses upward, velocity and concentration profiles evolve in response to the boundary conditions on the walls, convection, and diffusion from the gas/liquid interface. Fluid then flows across

an open channel into the reservoir generating a non-uniform oxygen concentration profile in the reservoir, where the cycle is completed.

The control volume for the model, shown in figure 3.11, extends from the air-liquid interface down to the scaffold in the reactor well and the filter in the reservoir well.

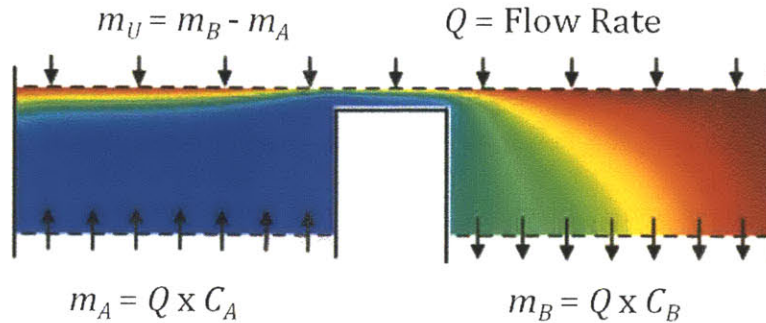


Figure 3.11: oxygen absorption schematic

The oxygen transport model was based upon existing MATLAB code⁷² with an added mass transport equation as previously described. The model first calculates a flow profile from Navier-Stokes and continuity equations and iterates solutions until the profile stabilizes. The flow profiles are then used in convection diffusion equations to find oxygen concentration.

The model uses a variable node depth in the direction normal to the cross-section to satisfy the continuity equations for a variable profile depth. Since only one node is used in the z-direction, the model does not account for any velocity gradient in that direction and slip walls are assumed for these node faces. The model was compared with a more computationally expensive, fully-3D finite-elements model for a range of conditions, and determined these simplifications result in minimal error. No-slip boundaries are prescribed at the walls that appear in the cross-section, and a free surface is prescribed at the air-liquid interface. Saturated oxygen concentration is maintained at the air-liquid interface ($\theta = 1$). Minor geometrical features including the well tapers, side pockets in the wells for extracting scaffolds, retaining rings and a meniscus in the fluid are neglected.

Analysis of several hundred simulations across a range of design and operating conditions (surface channel geometry, fluid depth and flow rates) shows a high correlation between the Peclet number for each simulation and the oxygen absorption potential (figure 3.12).

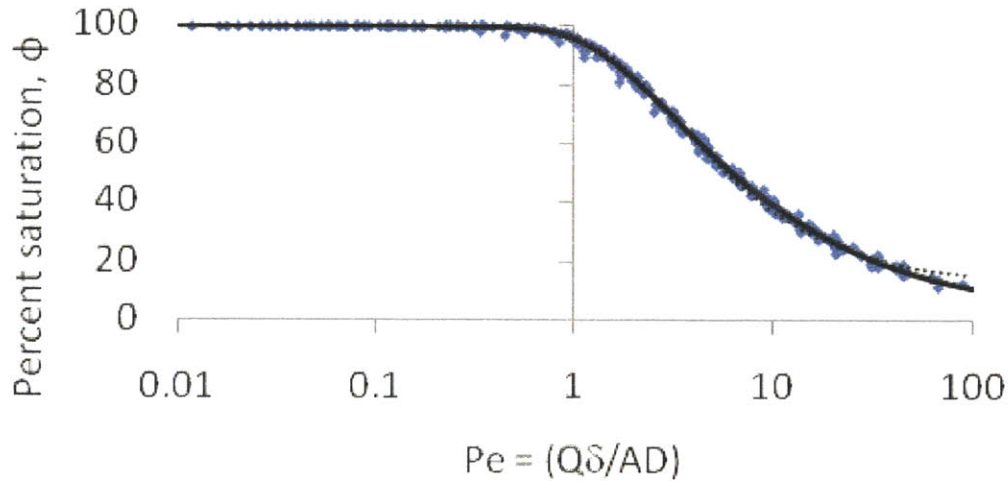


Figure 3.12: Oxygen absorption potential across a wide range of design and operating conditions shows high correlation with the Peclet number for oxygen transport across the surface channel.

Based on the schematic shown in figure 3.11 the region for oxygen absorption is primarily located over the surface channel and extends to roughly half way into each well. Therefore the surface area used to calculate the Peclet number only includes half of the surface area of each well. Figure 3.12 shows that for simulations with a Peclet number below one, the oxygen absorption potential approaches 100% (diffusion of oxygen from the atmosphere into the system dominates over transport of medium away from the air-liquid interface).

Using a combination of the hill function and an exponential function,

$$\phi = 100 - 75e^{-3/Pe} - \frac{20Pe}{20+Pe} \quad (3.18)$$

the oxygen absorption potential for a given system can be predicted (solid line) directly from the Peclet number. For oxygen absorption potential above 20% a simple exponential decay function,

$$\phi = 100 - 87e^{-10/3Pe} \quad (3.19)$$

can be used with good accuracy (dashed line).

The oxygen absorption potential is related to the total mass transport by equation 3.14 which is also includes the total gradient of oxygen concentration and the flow rate through the system. Assuming all other parameters are constant, an increasing flow rate will always increase the total mass transfer from the air-liquid interface into the system. The result of multiplying the oxygen absorption potential (as calculated using 3.19 from the Peclet number) with the flow rate for constant depth and surface area is shown in figure 3.13. From this figure it is clear that total oxygen delivery always increases with increasing flow rate.

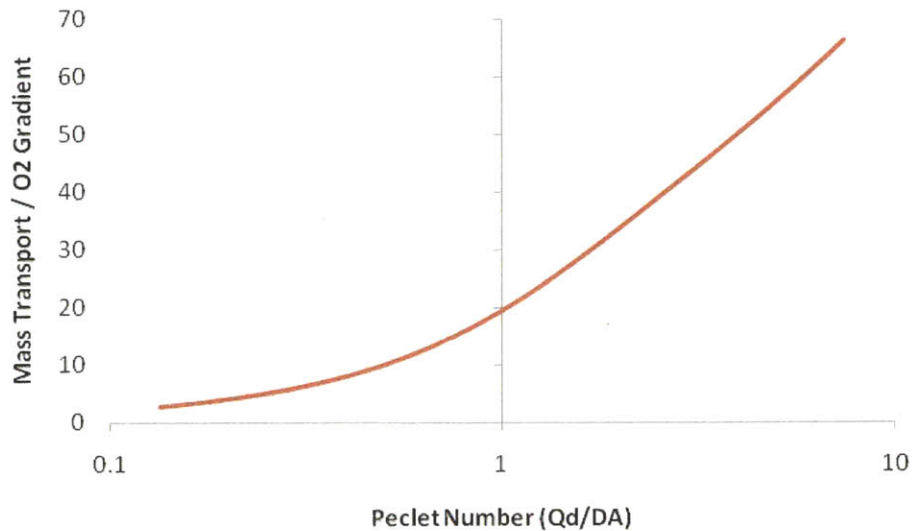


Figure 3.13: Total absorption into the system normalized to the difference between oxygen saturation and the concentration of oxygen exiting the scaffold increases with increasing Peclet number.

3.4 Bioreactor design

Blood is supplied to the liver in vivo from the hepatic artery (~80%) and from the portal vein (~20%)⁵¹. Because of the large percentage of venous blood supply, oxygen concentration levels in the liver are significantly below the arterial oxygen concentration. It is reasonable to assume that an ideal oxygen

environment for liver tissue could be well below saturated oxygen concentration. However, since culture medium has a lower oxygen carrying capacity than blood (due to a lack of hemoglobin), it is also possible that oxygen supply to the tissue should be maximized. In order to determine the ideal oxygen environment for the bioreactor, a special bioreactor was designed to incorporate several different oxygen environments onto a single plate.

3.4.1 Discussion of design parameters influencing oxygen absorption capacity

Literally any oxygen concentration at the tissue inlet is attainable with any bioreactor configuration using an incubator with oxygen regulation. However, with a higher oxygen absorption capacity, the concentration of oxygen entering the tissue can be set with increasing precision. When the oxygen absorption capacity is 99%, the concentration of oxygen entering the tissue will always remain within 99 and 100% of saturation regardless of the concentration of oxygen exiting the tissue. When oxygen absorption capacity is only 50%, the oxygen concentration entering the tissue can fluctuate across a much broader range between 50% and 100% of oxygen saturation.

Additionally, based on the shape of the curve in figure 3.12, oxygen absorption capacity is sensitive to changes in the Peclet number when the Peclet number is between 1 and 10. Of the design parameters that make up the Peclet number the variables that are set by design include the flow rate, fluid surface area and the fluid depth. Of these, the depth of fluid is the most prone to variation during an experiment. Changes in fluid depth can occur during medium exchange or because of evaporation. Flow rate is generally set by the amount of tissue seeded into the bioreactor, but is also susceptible to variation. Inter-well flow variability in a plate is within 5%¹⁵.

There are also drawbacks to systems designed for a high oxygen absorption capacity. Although a lower flow rate will increase the oxygen absorption capacity, it will decrease the total oxygen delivery to the scaffold as shown in figure 3.13. Another method for increasing oxygen absorption capacity is to

Increase the surface area of the fluid. However, a large air-liquid interface limits the number of bioreactors that can fit on the footprint of a standard tissue culture plate, and the larger surface area requires more fluid volume for each bioreactor. This is not desirable for reasons discussed in section 2.6.

A third method for increasing the oxygen absorption capacity is to decrease the depth of fluid in the surface channel. The drawback is that surface tension is dominant at shallow depths, so depths below roughly 1 mm are not achievable in practice. In these situations the center of the channel dries out and all fluid travels along the edge formed at the vertical channel walls. Additionally, since the Peclet number is not linearly related to the channel depth, the influence of fluid depth on the Peclet number increases as the fluid level decreases (e.g. an increase in depth by 0.5 mm changes the Peclet number by 50% at an initial depth of 1 mm versus 10% at an initial depth of 5 mm).

Finally, it is possible to develop a system that does not follow the relationship presented in figure 3.8, potentially by mixing the fluid at the surface. Although active mixing would require an additional actuation system, it may be possible to mix the fluid by inserting baffles along the flow path. As fluid with certain Reynolds number moves through corners, rotational flow circulates fluid across the surface. Unfortunately, this phenomenon is negligible with the low Reynolds number for flow across the channel.

3.4.2 Oxygen test bioreactors designed with three different oxygen absorption capacities

Given the uncertainties surrounding the nature of how oxygen concentration influences tissue function, a bioreactor array was designed that incorporates three different bioreactor designs with three different oxygen absorption capacities. The purpose was to determine both the ideal oxygen environment for the bioreactor and also to gain some understanding for the sensitivity of the culture environment to variations in oxygen concentration. A schematic of this bioreactor is shown in figure 3.14. The depth of

the wells (from the bottom of the surface channel to the scaffold) in the three different designs is adjusted so that each design holds the same total medium volume (1.5 mL).

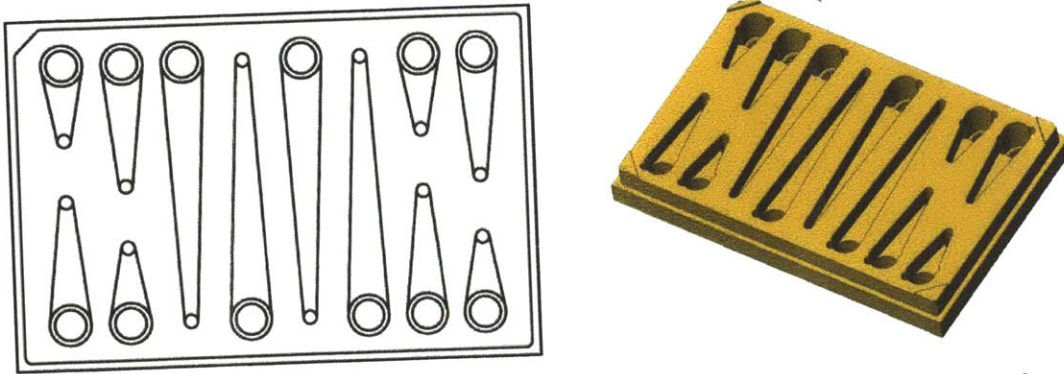


Figure 3.14: Bioreactor plate with three different designs used to study the influence of oxygen concentration on liver cell cultures. A schematic is shown on the left with the solid model on the right.

Because some uncertainty in oxygen supply levels is likely acceptable (oxygen saturation concentrations vary by 3% due to changes in atmospheric pressure), and because the oxygen concentration in liver in vivo is well below saturating oxygen concentration in cell culture medium, it was reasoned that bioreactors with low oxygen absorption capacity may be well suited for liver culture. This design would allow for a dense array of bioreactors on the plate and could be used to minimize the volume of cell culture medium. Bioreactors with a mid range oxygen absorption capacity were included to increase the precision with which inlet oxygen concentration can be controlled, and high oxygen absorption bioreactors would maximize the oxygen delivery to the tissue, and can be operated to precisely set the inlet oxygen concentrations using specialized incubators.

Oxygen absorption potential was set by varying the surface area available for oxygen absorption. While the bioreactors are designed to operate with a depth of 2mm, the oxygen absorption capacity can also be adjusted using this parameter. However, changing the depths by some amount in designs with different surface areas will require differences in total medium volume which is undesirable for a direct comparison. Table 3.2 shows the surface areas of the three different designs and the corresponding absorption potential.

Table 3.2: Design parameters for bioreactors with varying oxygen absorption potential. The reported surface area is the total surface area of the fluid. For calculation of the Pelcet number, 0.4 cm² should be subtracted from this number to account for ½ the surface area of the two wells.

	Surface Area (cm ²)	ϕ (2 mm depth)
Low O ₂ Design	1.7	90%
Med O ₂ Design	2.4	67%
High O ₂ Design	4.6	50%

3.5 Influence of oxygen environment on rat liver cell culture

Three different bioreactor configurations were investigated using cultures of primary rat and mouse hepatocytes. The oxygen environment in each of the bioreactor configurations was confirmed through concentration measurements. Total albumin production and total bile acid production was analyzed for the different bioreactor configurations and the total protein in each scaffold was measured at the end of the incubation period. Culture protocols and assay protocols have previously been reported¹⁵.

3.5.1 Oxygen environment evaluation

In order to validate that differences in design do translate to differences in oxygen concentration, a device for simultaneously measuring oxygen concentration in six bioreactors (12 sensor locations) was developed. Since oxygen concentration is measured optically and an optical fiber connects the sensing material (sensor probe) with the electronic sensor equipment, a device was developed that switches between optical fiber connections so that one set of sensing equipment can cycle between different sensor probes. The optical splitter connects four sensor ports from a commercially available sensor (Precision Sensing GmbH, Regensburg, Germany) to twelve optical sensors. A schematic and photos of the devices are shown in figure 3.15. This device allows monitoring of six bioreactors (2 bioreactors for each oxygen condition) throughout the duration of culture.

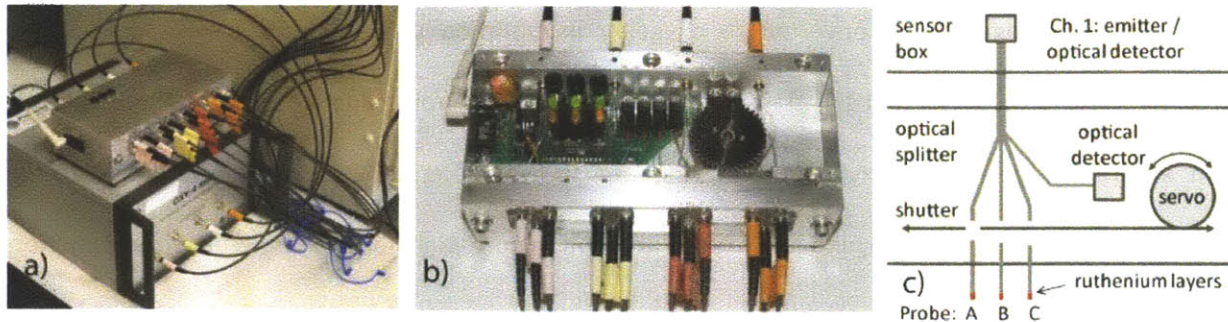


Figure 3.15: Oxygen sensor multiplexor designed to cycle sensing equipment between three different oxygen probes. After oxygen is recorded on one probe, the multiplexor automatically reconnects the sensing equipment with the next probe and waits for a measurement to be taken. Once a measurement is taken, the multiplexor connects the sensing equipment with the next sensor in the series. The process can repeat indefinitely.

A 2 mm diameter optical fiber is split in the optical splitter (3.15C) into 3, 1 mm diameter fibers and several 0.5 mm diameter fibers. The 1 mm diameter fibers have ruthenium layers attached to the terminal end and the 0.5 mm diameter fibers connect to a photodetector in the optical splitter. Light emitted from the sensor box (3.15A bottom) travels along the 2 mm diameter optical fiber into the optical splitter. A shutter allows light to travel along one of the three 1 mm diameter fibers to the ruthenium sensing layer attached at the end of the fiber (the oxygen probe). Light emitted from the excited ruthenium travels back along the optical fiber and intensity is recorded in the sensor on one of the four channels. A photodetector in the optical splitter senses when a measurement has been taken. After measurements have been recorded on all active channels, a servo moves the shutter to the next set of oxygen probes for a reading. The process is repeated throughout the duration of an experiment. Electronic control is achieved using a custom designed circuit powered by a microcontroller (ATMega-48, Atmel Corporation, San Jose, California).

Calibration measurements are recorded in oxygen saturated medium as well as oxygen depleted medium. Calibrations for each individual sensor are used to generate reference equations (Stern-Volmer, discussed in the following chapter) for converting phase readings to oxygen partial pressure. Oxygen measurements for each 5 minute time interval (roughly 6 individual measurements per interval)

are grouped, averaged, and converted to oxygen concentration using Henry's Law. Total oxygen consumption and the oxygen absorption potential are calculated from concentration readings. Results from a 48 hour period of oxygen monitoring are shown in figure 3.16. Oxygen concentration measurements in high, medium, and low oxygen absorption potential bioreactors agree with predictions from the models.

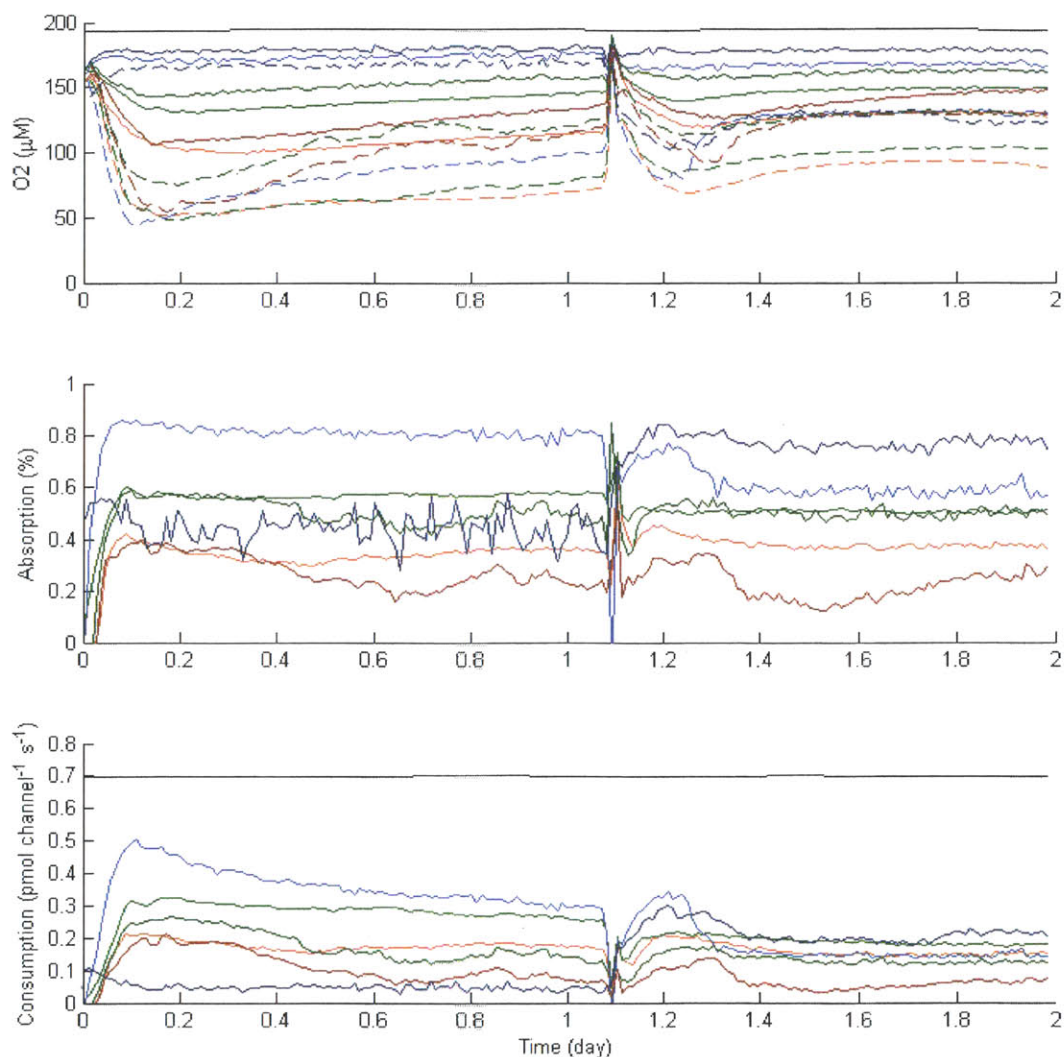


Figure 3.16: Shows two days of oxygen concentration measurements for rat cell culture. The top plot shows concentration measurements from 12 sensors placed in 6 bioreactors. The black line is saturating oxygen concentration as predicted from atmospheric pressure. Blue curves are from reactors with the

highest oxygen absorption potential, green are from bioreactors with mid range absorption potential and red are from bioreactors with the lowest oxygen absorption potential. The initial high concentration and spike at day 1 result from medium exchanges where oxygen saturated medium was added to the bioreactor. The oxygen sensor above the scaffold in one of the high oxygen bioreactors (blue lines) appears not to have been completely submerged in the medium during the first day. Absorption potential and metabolic activity during this day are therefore not representative. During the second day, absorption potential (middle plot) agrees with predictions from the models. The gradual decline in consumption (bottom plot) indicates a progressively decline in metabolic activity. The black line in this plot is the product of flow rate and saturating oxygen concentration, indicating the total amount of oxygen that would be available for consumption if absorption potential is driven to 100%.

3.5.2 Biological results

Total protein measurements from 4 culture experiments comparing various oxygen environments are shown in figure 3.17. This figure shows one experiment with mouse hepatocytes and three with rat hepatocytes. Figure 3.18 shows production of albumin and bile acids from an experiment with rat hepatocytes.

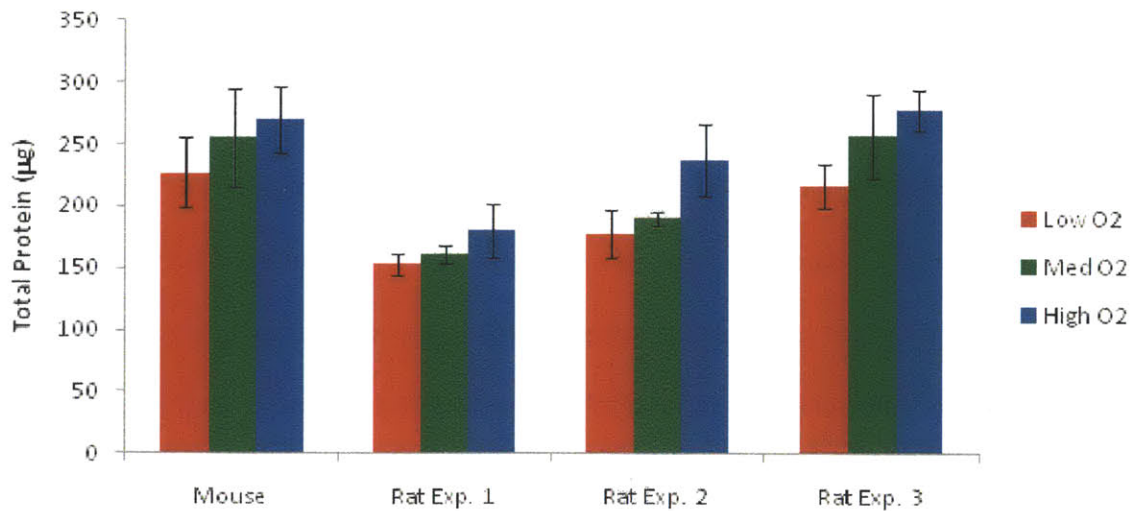


Figure 3.17: Total protein retained in the scaffold at the end of culture. A small but consistent trend shows that high oxygen content bioreactors retain more cells as measured by total protein.

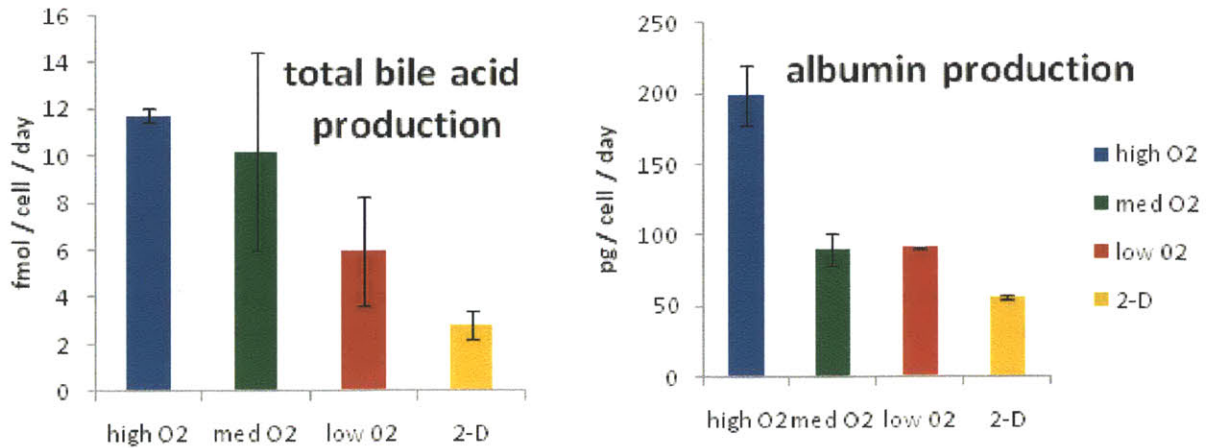


Figure 3.18: Albumin production and total bile acid production in different oxygen environments.

Seen from these experiments, the high oxygen environment fosters increased cellular retention and higher activity as measured by albumin production.

3.5.3 High oxygen capacity bioreactor

Based on the results obtained from rat studies, an array of high oxygen bioreactors was developed. A schematic of the plate is shown in figure 3.19. Each bioreactor is identical to the high oxygen capacity system investigated in the above studies. This bioreactor delivers a maximum amount of oxygen to the tissue when used in a standard CO₂ incubator. Low oxygen levels can be achieved in specialized incubators. This bioreactor configuration offers the highest degree of control of the oxygen environment and minimizes sensitivity to variations in experimental parameters such as medium depth. As mentioned previously, the drawbacks of this configuration include the volume of culture medium required in each well, and the reduced density of bioreactors on the plate. Even with constraints on array density, the spacing between bioreactors is exactly 9 mm, the same distance between wells on a 96-well plate, which allows use of a standard 12 channel pipette and facilitates cell seeding and sampling.

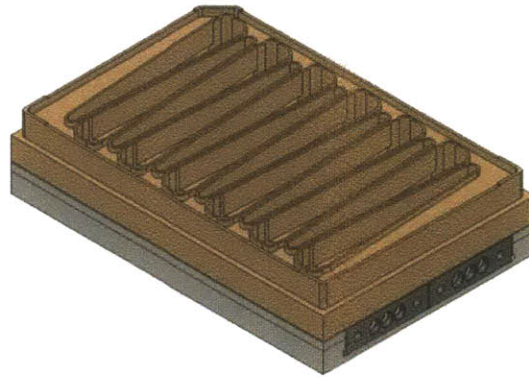


Figure 3.19: High oxygen content bioreactor

3.6 Experimental application of oxygen sensors

Online sensing of oxygen concentration is also useful for understanding the full timecourse of the response to an experimental treatment. This utility was demonstrated in a toxicology study where the cells were treated with varying concentrations of a drug that has been found toxic to the liver, perhexiline⁷³. After three days in culture, rat hepatocytes were treated with a range of dosing conditions expressed as a multiple of the maximum concentration measured in human plasma after a single dose C_{\max} ($0.6 \mu\text{g mL}^{-1}$)⁷⁴.

Oxygen concentration in the treated cultures was monitored during the 24 hour period following the initial dose, figure 3.20. Seen in this figure there is an immediate response followed by a stabilization of metabolic activity after roughly 12 hours. By monitoring the oxygen concentration the full timecourse of the response is available rather than a discrete sampling instant.

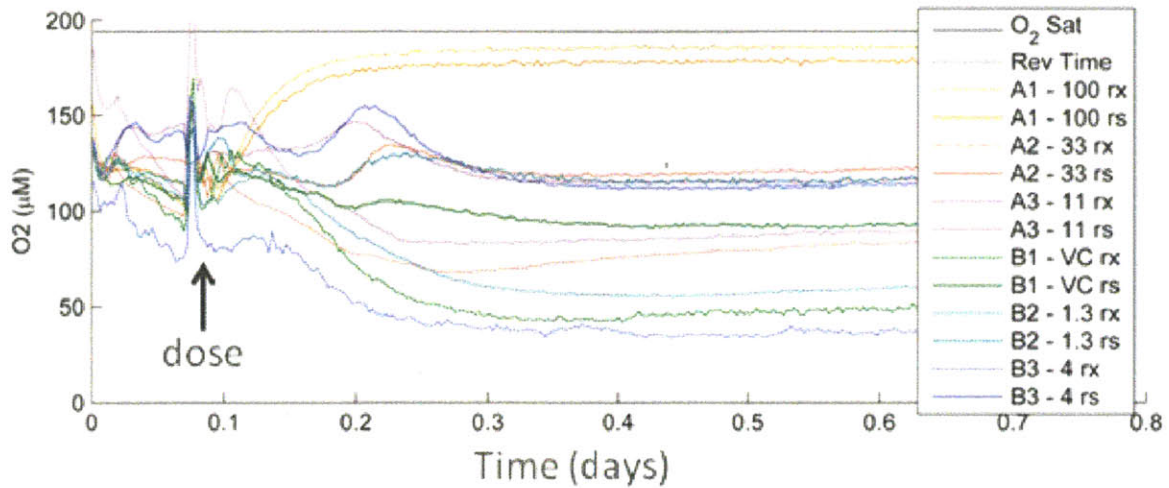


Figure 3.20: Oxygen concentration measurements following drug dose (day 3) show an immediate drug response, followed by stabilization in metabolic activity after roughly 12 hours.

Metabolic activity as measured by oxygen consumption at the end of the experiment, figure 3.21, shows a dose related response over the conditions tested. This indicates that oxygen consumption measurements have resolution to identify differences across the treatment conditions.

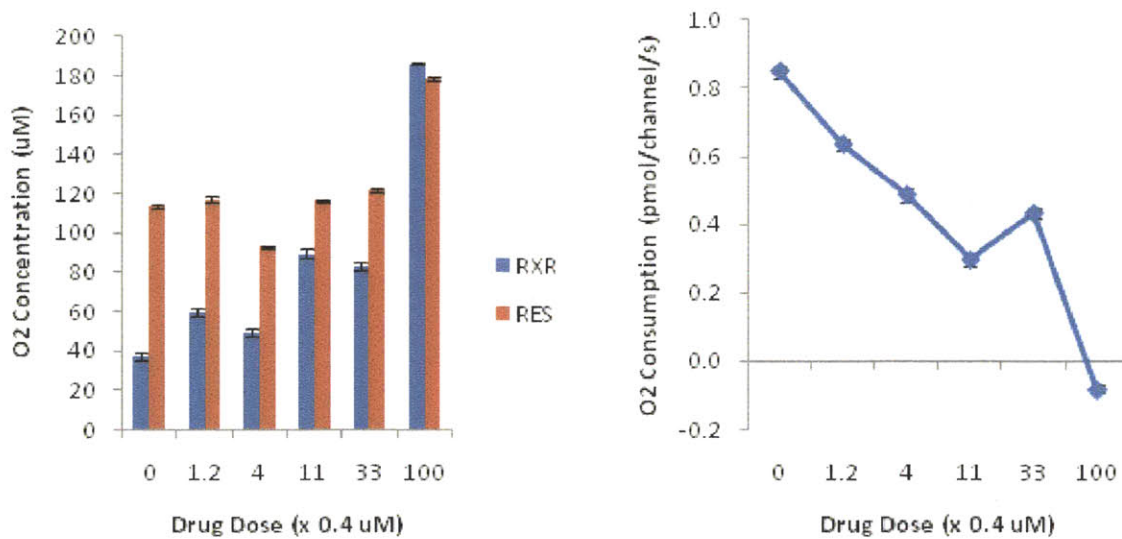


Figure 3.21: Oxygen concentration and oxygen consumption at the end of the drug incubation show a clear dose response to the drug. Error bars indicate the standard deviation in consumption measurements over the last 7 hours of culture.

3.7 Discussion

Oxygen consumption by the cells is influenced by the oxygen delivering capacity of the bioreactor system. The oxygen environment of the system can be modulated by the design of the surface area for oxygen exchange. The influence of differences in the oxygen environment on tissue function was investigated and an optimal design was selected. Oxygen measurements provide a real-time readout of tissue activity and bioreactor characteristics. These measurements allow access to the full time-course of a treatment response. This information could provide value for dose-response experiments such as drug toxicity studies.

4. OXYGEN SENSORS

4.1 Introduction

There is a growing recognition for the value of noninvasive, real-time data collection in cell culture experiments²⁰⁻²². Non-invasive, online data collection increases the yield from each experiment by offering insight into the full time-course of a treatment rather than discrete sampling intervals. Maximizing the amount of information collected in an experiment is particularly important for studies involving precious materials such as primary human cells, or when using advanced culture environments geared towards recreation of complicated tissue function. Online system monitoring also allows instant validation of experimental parameters, potentially allowing for adjustments to the current experiment, rather than a follow on experiment which could be several weeks delayed.

Optical sensors that can measure the excitation characteristics of an indicator material have received a large amount of attention over the past decade^{20-27, 75}. Indicator materials are selected such that their fluorescent properties are predictably influenced by the surrounding environment. These types of sensors can provide non-invasive, cost effective means for continuous monitoring of key culture conditions including oxygen, CO₂, and pH²³. Oxygen concentration can be measured by examination of the fluorescent intensity or decay time of an excited ruthenium complex^{34, 76-78}. Oxygen concentration is an indicator of metabolism for eukaryotic cells and is therefore an ideal candidate for online monitoring. Measurement of oxygen provides a sensitive, instant (real-time), non-invasive, and quantitative readout of cellular metabolism and bioreactor operational performance.

Significant advances have been made in development of mechanically and chemically stable sensing materials^{28, 29}, but relatively few developments have been made in the sensing techniques used for measurement. Currently three measurement techniques are employed. The first is to measure the

total emission intensity for a given excitation signal^{22, 24-27}. This method suffers from signal drift, is particularly sensitive to the intensity of excitation and requires frequent re-calibration. The second method is to measure the phase lag between a sinusoidal reference signal and the response signal^{30, 31}. This method is problematic because it assumes that the fluorescence decay exactly fits a first order exponential decay and only measures phase at a single frequency³². The final method is to excite the material with an impulse from a laser or a light emitting diode (LED) and to measure the response^{20, 33-35}. This method is able to identify the time response to an impulse, but is subject to noise and averaging multiple signals (to reduce noise) can be a slow process. Both the phase and impulse response techniques are also used in fluorescence lifetime imaging microscopy (FLIM). For FLIM analysis simultaneous excitation with multiple frequencies has also been investigated but only with a limited number of excitation frequencies, typically fewer than five⁷⁹.

This thesis describes an alternative approach where sensors excite a layer of ruthenium using a stochastic signal. The stochastic signal simultaneously excites the sensor at all frequencies of interest. Stochastic excitation allows rapid identification of the decay lifetime with relatively low noise.

The sensor employs a standard blue LED for exciting the ruthenium, a photodiode for recording the emission signal and several optical filters for separating the LED excitation from the ruthenium emission. The sensor has an 8.5 x 17.5 mm footprint so multiple sensors can be integrated into the lid of a tissue culture plate for continual oxygen measurements in multiple wells (for reference the well to well spacing in the bioreactor and in a 96-well plate is 9 mm).

This chapter contains a description of the oxygen sensor and discussion of the system identification techniques employed to measure oxygen concentration.

4.2 Optical oxygen sensor background

Ruthenium complex materials (e. g. tris(2,2'-bipyridine)ruthenium dichloride) are often used to sense the partial pressure of oxygen in an environment^{34, 76-78}. When the ruthenium complex absorbs a photon of light the absorbed energy promotes an electron from the ground state to an excited state. The ruthenium complex will remain in the excited state for a short period of time and will return to the ground state through one of several mechanisms. One such mechanism is through the emission of a second photon, which can be observed by measuring emitted light. A second mechanism for returning to the ground state is through quenching, in which no light is emitted. Since excited ruthenium is quenched by molecular oxygen, the rate at which excited ruthenium returns to the ground state, or the rate of fluorescence decay, is influenced by the degree of access between excited ruthenium and molecular oxygen, or the local partial pressure of oxygen at the sensor. A third method for returning to a ground state is through fluorescence resonance energy transfer (FRET), but this mechanism is not applicable for the oxygen sensor.

The release of light for a simple fluorophore, and consequent return to the ground state, can be described by a first order reaction

$$\frac{dM^*}{dt} = -kM^* \propto \text{fluorescent intensity} \quad (4.1)$$

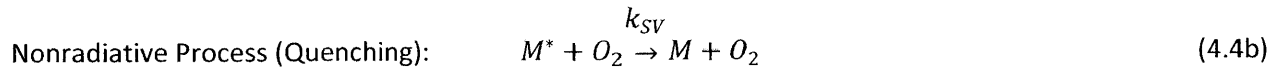
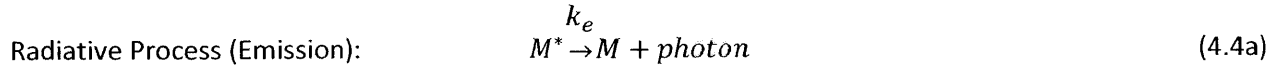
where M^* denotes the number of molecules in the excited state⁸⁰ and k is the rate constant. The solution to this equation is

$$I = I_{t0}e^{-t/\tau} \quad (4.2)$$

where $\tau = 1/k$ is the time constant for decay and I denotes the emission intensity. The time constant and emission intensity are related to the partial pressure of oxygen by the Stern-Volmer equation,

$$\frac{I_0}{I} = \frac{\tau_0}{\tau} = 1 + K_{SV}O_2 \quad (4.3)$$

where O_2 is the concentration of oxygen, K_{SV} is the Stern-Volmer constant, and τ_0 and I_0 are the time constant and emission intensity in the absence of oxygen. This equation can be derived from the rate equations for the two processes for returning to ground state



$$\text{Combined Decay Rate:} \quad \frac{dM^*}{dt}_{\text{decay}} = -k_e M^* - k_{SV} O_2 M^* = -(k_e + k_{SV} O_2) M^* \quad (4.5)$$

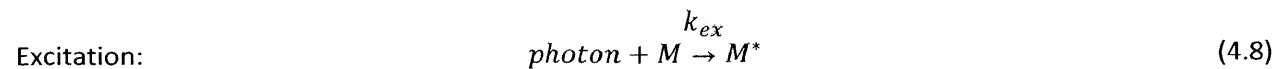
$$\text{Time Constant at Zero Oxygen:} \quad \tau_0 = \frac{1}{k_e} \quad (4.6)$$

$$\text{Time Constant at arbitrary Oxygen:} \quad \tau = \frac{1}{k_e + k_{SV} O_2} \quad (4.7)$$

The Stern-Volmer equation for relating a time constant to the time constant for decay at zero oxygen concentration can now be formed,

$$\text{Stern-Volmer Equation:} \quad \frac{\tau_0}{\tau} = 1 + \tau_0 k_{SV} O_2 = 1 + K_{SV} O_2$$

The Stern-Volmer equation expressed as a ratio of fluorescent intensity to fluorescent intensity in the absence of oxygen can be found using a similar approach. Excitation of ruthenium by the LED can be described in a format similar to 4.4,



where in this case the photon is incident on the ruthenium layer. If $u(t)$ is used to quantify the amount of incident photons, the differential equation describing the excitation process is

$$\frac{dM^*}{dt} \text{ excitation} = k_{ex}u(t)M \quad (4.9)$$

which relates the contribution of incident light from the LED to the excitation of ruthenium. Assuming that the total amount of ruthenium M_t is the sum of ruthenium in the excited and ground states, that this number is constant, and that there is vastly more ruthenium at the ground state than the excited state results in

$$\frac{dM^*}{dt} \text{ excitation} = k_{ex}u(t)(M_t - M^*) \approx (k_{ex}M_t)u(t) \quad (4.10)$$

where the product of $k_{ex}M$ is approximately constant. Combining this equation with 4.5 gives,

$$\frac{dM^*}{dt} = -(k_e + k_{SV}O_2)M^* + k_{ex}u(t) \quad (4.11)$$

which combines the excitation and emission processes. When a steady state is reached under constant excitation $\frac{dM^*}{dt}$ becomes 0. By rearranging the terms on the right hand side the Stern-Volmer equation (4.1) is expressed as a ratio of fluorescent intensity (where $I = k_e M^*$). More importantly, 4.11 is a complete relationship between the input signal from the LED and the quantity of excited ruthenium as a function of the concentration of oxygen. A state space model for the system is now available

$$\dot{x}(t) = -(k_e + k_{SV}O_2)x(t) + k_{ex}u(t) \quad (4.12)$$

$$y(t) = k_{pd}x(t) \quad (4.13)$$

where k_{pd} represents the gain between emission and a measurement taken by the ADC. In practice the Stern-Volmer equation 4.3 is used to deal with calibration constants and for converting dynamic measurements of the system to oxygen concentrations.

4.3 Calibrations and oxygen readouts

The two unknown constants in the Stern-Volmer equation τ_0 and k_{SV} are found from calibration at two or more known oxygen concentrations, typically zero oxygen and oxygen saturation in liquid. The measurement at zero oxygen is a direct measure of τ_0 . The measurement at oxygen saturation is then used in

$$K_{SV} = \frac{1}{[O_2]_{100}} \left(\frac{\tau_0}{\tau_{100}} - 1 \right) \quad (4.14)$$

to find the Stern-Volmer constant. Additional time constant readings can be converted to oxygen concentration using the two calibration values with

$$O_2 = \frac{1}{K_{SV}} \left(\frac{\tau_0}{\tau} - 1 \right) \quad (4.15)$$

Since this is a nonlinear equation it is important to understand how the sensitivity of oxygen readouts to error changes as a function of oxygen concentration. A plot of oxygen concentration versus the measured time constant is shown in figure 4.1. Based on the shape of the curve, estimation error for the time constant will have a large influence in the concentration measurement for high oxygen concentrations, and will result in minimal error at low oxygen concentration. Calibration errors are also have the same relationship. A 5% calibration error for high oxygen concentration will create an error in the concentration measurement of roughly 6%, whereas the same error for the low calibration value will only impact low oxygen concentration readings by roughly 2%.

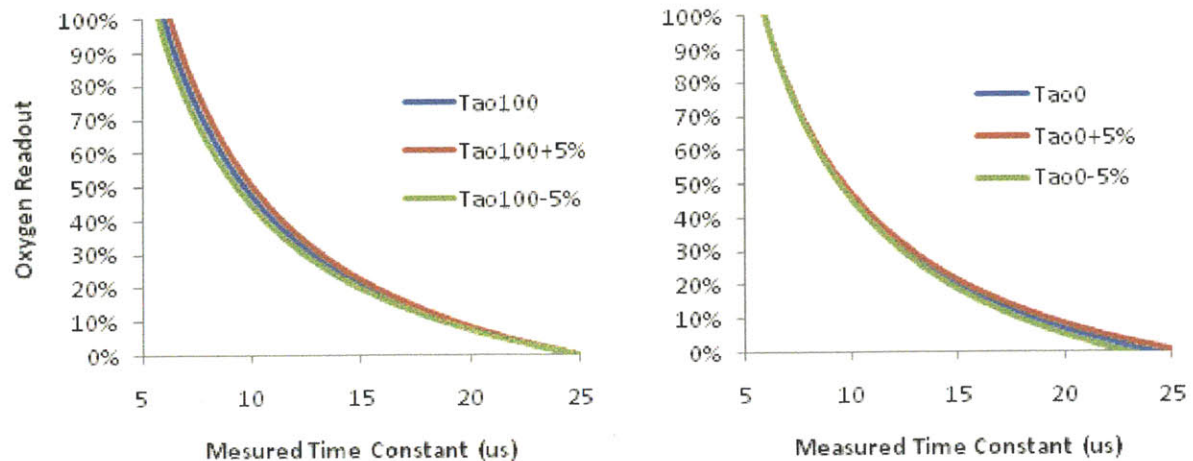


Figure 4.1: Influence of time constant measurement error on predicted oxygen concentration.

4.4 Optical oxygen sensor design

The ruthenium probe is excited using a blue LED and emitted fluorescence is measured using a photodiode (Optek, Carrollton, Texas). Light from the LED passes through an optical filter (Chroma, Bellows Falls, Vermont) then a plastic lens (Optima Precision, West Linn, Oregon) focuses the light into an optical fiber (Industrial Fiber Optics, Tempe, Arizona). A layer of ruthenium (Precision Sensing, Regensburg, Germany) attached to the end of the fiber excites in response to the LED signal and emitted light travels back along the optical fiber. The light emitted from the ruthenium is optically filtered and luminescence is recorded using a photodiode. The optical properties of the filters, LED, photodiode are shown in figure 4.2 along with a typical emission and excitation spectrum for a ruthenium complex^{77, 81}.

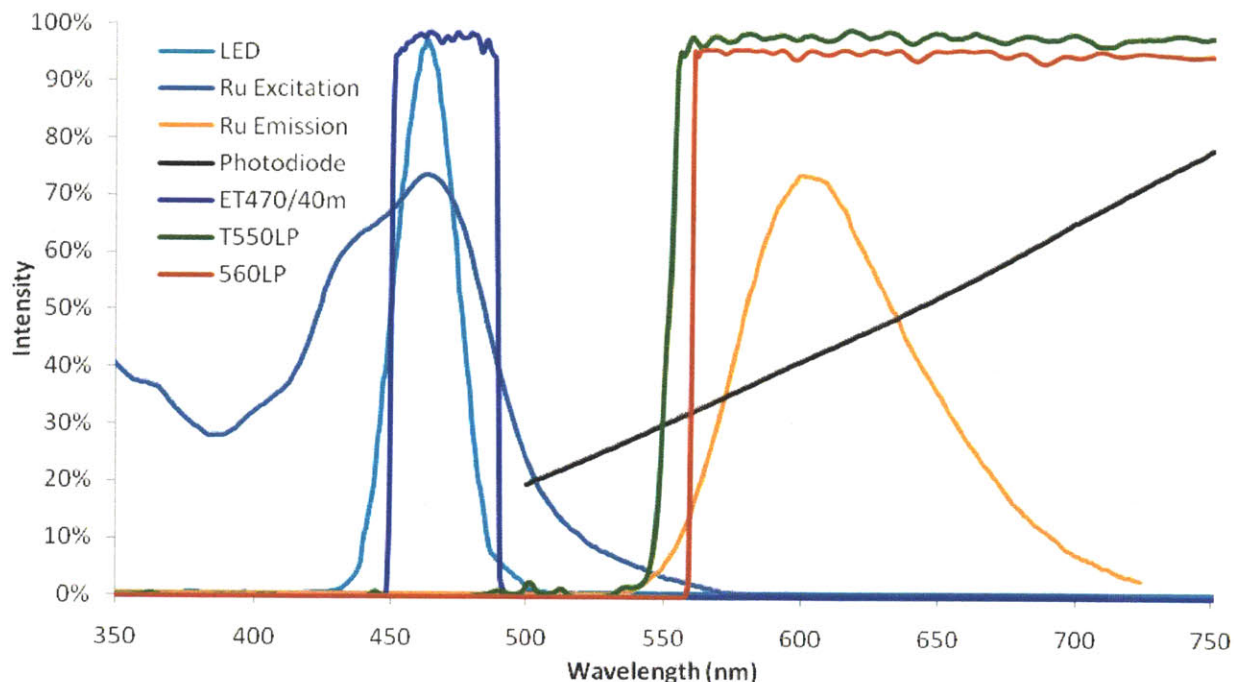


Figure 4.2: Optical properties of relevant sensor components and typical excitation and emission spectrum of ruthenium complexes⁷⁷.

Electrical current from the photodiode is fed into a transimpedance amplifier (Texas Instruments, Dallas, Texas) with a gain of 10^7 . Voltage is measured using an ADC (Analog Devices, Norwood, Massachusetts) and each reading is recorded using a microcontroller (Atmel, San Jose, California). The sensor circuit is shown in figure 4.3. A maximum sampling rate of 2 MHz is achievable on the ADC and microcontroller, and the response time of the LED and photodiode are in the nanosecond range.

The sensing probe was designed to be integrated onto the lid of a bioreactor so that oxygen can be measured in each well. The footprint of the sensor is 8.5 x 17.5 mm in order to accommodate the 9 mm spacing between wells. A photograph of the sensor is shown in figure 4.4. Optical filters and mirrors are housed in a custom filter cube fabricated in house by 3D printing (Connex 500, Objet, Billerica, MA). Mirrors in the filter cube are aligned so the photodiode and LED attach from a single printed circuit board (Advanced Circuits, Aurora, CO). A cross section of the filter cube is shown in figure 4.5.

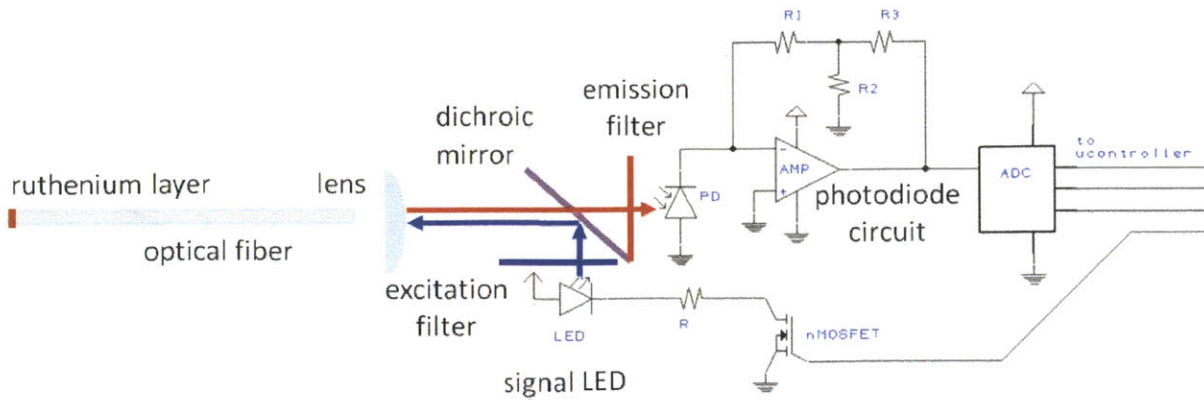


Figure 4.3: Schematic representation of the oxygen measuring sensor. The ruthenium layer on the left side of the schematic is placed in medium for oxygen analysis. The electronic circuit is controlled by a microcontroller and readings from the ADC are sent to a computer for signal processing.

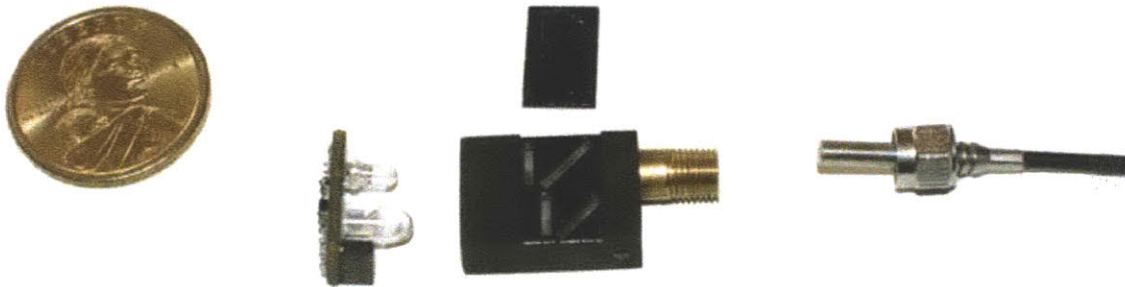


Figure 4.4: Oxygen sensor breakout showing LED and photodiode attached to the excitation, amplification and measurement circuit board. The filter cube with lid removed shows placement of the optical filters and mirrors. The optical fiber and ruthenium layer (not shown) attach to the filter cube.

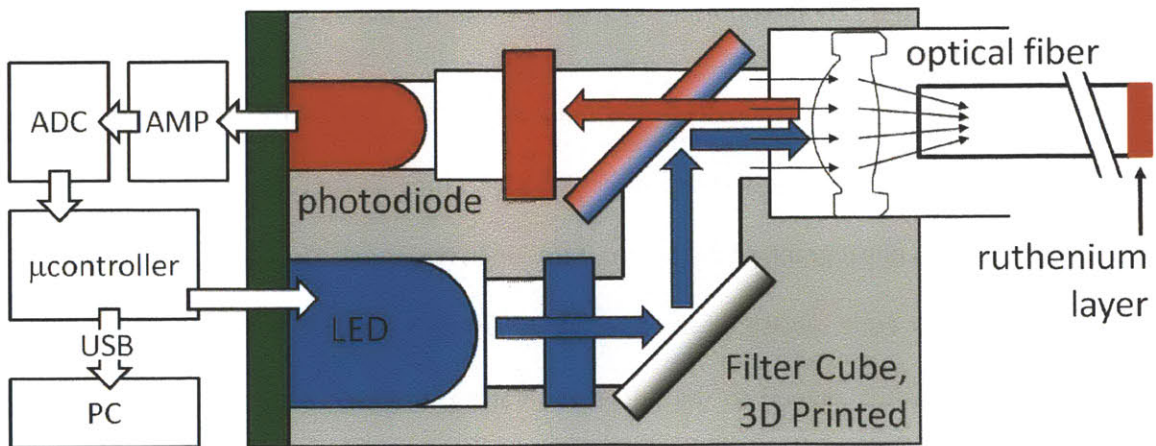


Figure 4.5: Schematic of filter cube showing blue LED and blue excitation filter. A first surface mirror is used to reflect blue light to a dichroic mirror. Blue light reflected off the dichroic is sent through a lens into the end of an optical fiber. Red light from the ruthenium probe is columnated by the lens, passed through the dichroic and through an emission filter before intensity is measured on the photodiode.

4.5 Measurement method

A stochastic binary sequence is generated by first creating a Gaussian sequence of random numbers with zero mean and a standard deviation of 1. This sequence is then low pass filtered using a first order filter with a time constant of 5x the sample frequency. Filtering is done to minimize overlap between excitation frequency and sampling frequency. This signal is then centered around the mean and values above zero are set to one with negative values set to zero. A binary pattern maximizes the average amplitude of the input signal because the LED cycles between zero and full power throughout the cycle, generally reducing the signal to noise ratio for the response. A segment of the resulting signal is shown in figure 4.6.

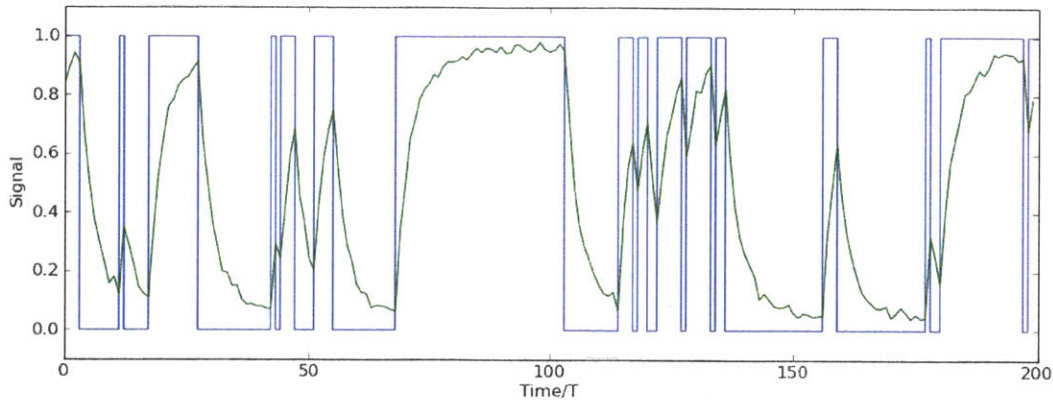


Figure 4.6: Stochastic binary pattern applied to the LED for excitation of the ruthenium sensor and response of the sensor for a short time segment. The x-axis shows time normalized by the sampling interval (typically 1 to 10 μs).

The autocorrelation and power spectrum of the input signal are shown in figure 4.7. The method for calculation of the correlation function is

$$R_{xy}(\tau) = \frac{1}{N} \sum_{t=\tau}^{N-1} x(t)y(t - \tau), \quad (4.16)$$

where wide-sense stationary is assumed for $t \geq 0$. Since no periodic functions were used in this work, and the power spectrum is used to calculate exponentially decaying functions, it was calculated on a

finite interval and values outside of the interval were truncated to zero. Using the relationship between correlation functions $R_{xy}(-\tau) = R_{yx}(\tau)$, cross-spectrum and power-spectrum were calculated by

$$\phi_{xy}(\omega) = \sum_{\tau=-\infty}^{\infty} R_{xy}(\tau) e^{-i\tau\omega} \approx F[R_{xy}(\tau)] + \overline{F[R_{yx}(\tau)]} - R_{yx}(0) \quad (4.17)$$

where the overbar denotes the complex conjugate and $F[\cdot]$ represents the discrete Fourier transform.

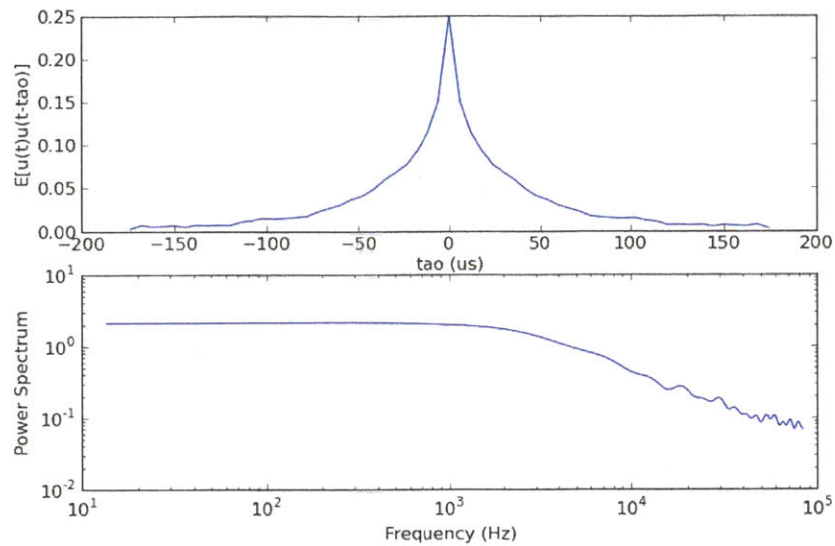


Figure 4.7: Autocorrelation and power spectrum of the excitation signal. The sample interval is $6 \mu\text{s}$ and the time constant for the first order low pass filter is $30 \mu\text{s}$. The power spectrum of the excitation signal is not exactly representative of a first order low pass filter because it has been hard limited.

The emission from the excited ruthenium is sensed on a photodiode and sampled using a 12-bit ADC. A maximum of 12,288 (0x3000) 12-bit values can be stored on the microcontroller, so this sets the length of the excitation signal. Upon completion of an excitation and measurement sequence, data is sent from the microcontroller to a computer over the universal serial bus (USB).

4.5.1 System identification, selection of the model

Since the signal is sampled at discrete intervals, the continuous state space equation 4.12 is converted to a discrete form using forward differences (Euler's approximation¹),

$$\left(\frac{q-1}{T}\right)x(t) = \frac{x(t+1)-x(t)}{T} = -(k_e + k_{SV}O_2)x(t) + k_{ex}u(t) \quad (4.18)$$

where q is a time shift operator such that $q^k x(t) = x(t+k)$. Rearranging this equation yields

$$x(t) = \frac{k_{ex}Tq^{-1}}{1-(1-Tk-Tk_{SV}O_2)q^{-1}}u(t) \quad (4.19)$$

which can be substituted into equation 4.13 for a relationship between measurement y and input u

$$y(t) = \frac{k_{pd}k_{ex}Tq^{-1}}{1-(1-Tk-Tk_{SV}O_2)q^{-1}}u(t) \quad (4.20)$$

To simplify notation two constants are introduced

$$A_{O_2} = 1 - Tk - Tk_{SV}O_2 \quad (4.21a)$$

$$B = k_{pd}k_{ex}T \quad (4.21b)$$

where O_2 is considered a constant because it varies on time scales much greater than the duration of a single measurement. The notation A_{O_2} is used as a reminder that A is a function of oxygen concentration. Re-arranging 4.20 and adding a noise term yields

$$y(t) = A_{O_2}y(t-1) + Bu(t-1) + v(t) \quad (4.22)$$

A second model structure can also be formed starting from 4.20 and using the solution for an infinite geometric series²,

¹ A different approximation for this derivative could have been selected such as Tustin's formula $(2/T^*(q-1)/(q+1))$

$$y(t) = \frac{Bq^{-1}}{1-A_{O_2}q^{-1}}u(t) = Bq^{-1}\sum_{k=0}^{\infty}A_{O_2}^kq^{-k}u(t) \quad (4.23)$$

After re-arranging terms and adding a noise term the second model is formed,

$$y(t) = B\sum_{k=1}^{\infty}A_{O_2}^{k-1}u(t-k) + v(t) \quad (4.24)$$

which leaves a choice between two model structures, a finite impulse response (FIR) with 4.24 and autoregressive with exogenous input (ARX) with 4.22. The fundamental difference between these two structures is that the FIR predicts measurements using only the input sequence into the system. The ARX structure predicts the next measurement based on the input to the system and the previous state of the system, i.e. the previous measurement. While the ARX structure only estimates two terms for a first order model, the FIR model must estimate an infinite series. In practice however this series of terms decays to zero over a finite interval.

The advantage of the FIR structure is that the parameter involving oxygen A_{O_2} is not directly linked to a measurement which will always have some noise level associated with it, but is instead tied to a deterministic input sequence u . The second advantage is that it is better equipped to handle errors in the model structure. If for example, the time constants for the electronic sensing equipment begin to influence the measurement the FIR model structure can seamlessly shift towards a second order model, whereas ARX would require re-formulation. There are several problems with this model structure however. The first is that it requires estimation of multiple parameters, although this is not a limitation in practice because the excitation signal is persistent to a very high order. The second problem is that the time constant $A_{O_2}^{-1}$ is not directly estimated by minimization of error using the original data, but is instead based on minimizing error by fitting a non-linear first order impulse response curve to the series of measured FIR coefficients.

² $\sum_{k=0}^{\infty} a^k = 1/(1+a)$, assuming $|a| < 1$

The second model is advantageous in that it requires the estimation of only two parameters and directly minimizes the prediction error as a result of selecting the time constant. However, as mentioned above it is more sensitive to noise from the measurement of y .

4.5.2 Least squares estimation of model parameters

Both 4.22 and 4.24 are equations that linearly combine known system inputs with constant coefficients.

This system can be represented them using,

$$y(t) = \varphi^T(t)\theta + v(t) = \theta^T \varphi(t) + v(t) \quad (4.25)$$

where the constant coefficients are contained in θ and the appropriate inputs are represented using φ ,

$$\theta = [b_1, \dots, b_{n_b}, \quad a_1, \dots, a_{n_a}]^T \quad (4.26)$$

$$\varphi = [u(t-1), \dots, u(t-n_b), \quad y(t-1), \dots, y(t-n_a)]^T \quad (4.27)$$

For equation 4.24 the coefficients for the infinite series decay to zero over some interval n_b , and the number of y terms in $\varphi(t)$, n_a , is zero. A measurement predictor can now be formed from the model

$$\hat{y}(t|\hat{\theta}) = \varphi^T(t)\hat{\theta} \quad (4.28)$$

and the model coefficients that minimize error between the data set $[y^N, u^N] \in Z^N$ and the prediction $\hat{y}(t|\hat{\theta})$. This is done by quantifying error using a cost function

$$V_N(\hat{\theta}|Z_N) = \frac{1}{2N} \sum_{t=1}^N (\hat{y}(t|\theta) - y(t))^2 \quad (4.29)$$

then solving $dV_N/d\theta = 0$ to find the model $\hat{\theta}$ that minimizes the function.

At this point it is simpler to use vector notation for the measurements and input sequences

$$\hat{Y} = [\hat{y}(1) \quad \dots \quad \hat{y}(N)]^T \quad (4.30a)$$

$$Y = [y(1) \quad \dots \quad y(N)]^T \quad (4.30b)$$

$$v = [v(1) \quad \dots \quad v(N)]^T \quad (4.30c)$$

$$\Phi = [\varphi(1) \quad \dots \quad \varphi(N)] \quad (4.31)$$

and so the cost function (4.29) becomes

$$V_N(\hat{\theta}|Z_N) = \frac{1}{2N} [\hat{Y} - Y]^T [\hat{Y} - Y] = \frac{1}{2N} [\Phi^T \theta - Y]^T [\Phi^T \theta - Y] \quad (4.32)$$

and taking the derivative

$$\frac{d}{d\theta} V_N(\hat{\theta}|Z_N) = \frac{1}{2N} \frac{d}{d\theta} [\Phi^T \theta - Y]^T [\Phi^T \theta - Y] = \frac{1}{N} \Phi [\Phi^T \theta - Y] = 0 \quad (4.33)$$

which leads to an important equality

$$\frac{1}{N} \Phi \Phi^T \hat{\theta} = \frac{1}{N} \Phi Y \quad (4.34)$$

Substituting $P^{-1} = \frac{1}{N} \Phi \Phi^T$ and $B = \frac{1}{N} \Phi Y$ into 4.33 and solving for $\hat{\theta}$ yields the least squares solution,

$$\hat{\theta} = PB \quad (4.35)$$

It is important at this point to understand the potential sources of error that could bias the estimation of

$\hat{\theta}$. By substituting a representation of the true system (4.36) into equation 4.34 and rearranging terms,

$$y(t) = \varphi^T(t) \theta_0 + v(t) \quad (4.36)$$

$$\frac{1}{N} \Phi \Phi^T \hat{\theta} = \frac{1}{N} \Phi (\Phi^T \theta_0 + v) \quad (4.37a)$$

$$\frac{1}{N} \Phi \Phi^T \hat{\theta} - \frac{1}{N} \Phi \Phi^T \theta_0 = \frac{1}{N} \Phi [v] \quad (4.37b)$$

results in

$$\hat{\theta} - \theta_0 = PF \quad (4.38)$$

where $F = \frac{1}{N} \Phi[v]$. So the bias between the estimated model $\hat{\theta}$ and the true system dynamics θ_0 is influenced by the noise term $v(t)$ in equation 4.36 and the parameters that are selected as inputs to the model, $\varphi(t) = [u(t-1), \dots, u(t-n_b), y(t-1), \dots, y(t-n_a)]^T$. While the excitation pattern $u(t)$ and noise should always be uncorrelated, thus the expectation of their product is zero, it is not clear that a previous sample of the system will be uncorrelated with noise in the current sample. Because the primary goal is to measure the true dynamics of the ruthenium, and an accurate noise predictor is less important, the low possibility of measurement bias in the FIR structure is of critical importance.

4.5.3 Computation of P, B, F using auto-and cross correlations

The final step is to compute $P^{-1} = \frac{1}{N} \Phi \Phi^T$ and $B = \frac{1}{N} \Phi Y$, then to solve for $\hat{\theta}$. The simplest approach is to first compute the auto and cross correlation for the input and measurement sequences using 4.16. The matrices P^{-1} and B can be formed from the first several terms in these correlation functions. This approach is demonstrated by stepping through the calculation of $\frac{1}{N} \Phi \Phi^T$.

The sequence of data has been set up such that the first u value in the excitation sequence occurs at $t = 0$ and the data is stored in $u[0]$. The first measurement occurs at $t = 1T$ where T is the sample interval, and the data is stored in $y[0]$. The excitation pattern and the sequence of observations have the same length but all observations are time shifted one sample interval forwards. This time shift is important for the following notation.

For a measurement sequence with N observations of y , each of the N columns in the input matrix Φ contain the relevant inputs for a particular measurement,

$$\Phi = \begin{bmatrix} \text{Column 1} & \cdots & \text{Column } N \\ u(1-1) & \cdots & u(N-1) \\ \vdots & \cdots & \vdots \\ u(1-n_b) & \cdots & u(N-n_b) \\ y(1-1-1) & \cdots & y(N-1-1) \\ \vdots & \cdots & \vdots \\ y(1-1-n_a) & \cdots & y(N-1-n_a) \end{bmatrix} \quad (4.39a)$$

where the first number is associated with the column (the first column is the input history for the first measurement and so on) and each of the y values are shifted backwards one time step to align with the input. Since the system is initially at rest all $u(t < 0)$ and $y(t < 0)$ are zero. This is a useful matrix for understanding the total number of parameters that can be predicted. Essentially a system of N equations (measurements) with $n_b + n_a$ unknowns (model terms) has been created. If $N = n_b + n_a$ then the system of equations can be solved to exactly specify the model parameters in θ . Generally there are more measurements (equations) than model terms so the system is over constrained and an exact solution is not possible; thus the model parameters are estimated by minimizing the error associated with a cost function. If however, there are fewer independent columns in Φ than rows, there is no unique solution for parameters that minimize a certain cost function, and the measurements do not provide enough information to uniquely identify the model parameters.

Recognizing that each row of 4.39a represents the entire input sequence shifted by a constant amount, a time shift operator q can be factored out

$$\Phi = \begin{bmatrix} q^{1-1}[u(0) \quad \cdots \quad u(N-1)] \\ \vdots \\ q^{1-n_b}[u(0) \quad \cdots \quad u(N-1)] \\ q^{0-1}[y(0) \quad \cdots \quad y(N-1)] \\ \vdots \\ q^{0-n_a}[y(0) \quad \cdots \quad y(N-1)] \end{bmatrix} \quad (4.39b)$$

The final step is to compute $\frac{1}{N} \Phi \Phi^T$ and $\frac{1}{N} \Phi Y$ from equation 4.34,

$$\frac{1}{N} \Phi \Phi^T = \frac{1}{N} \begin{bmatrix} q^0[u] \cdot q^0[u] & \cdots & q^0[u] \cdot q^{1-nb}[u] & q^0[u] \cdot q^{-1}[y] & \cdots & q^0[u] \cdot q^{-na}[y] \\ \vdots & \ddots & \vdots & \vdots & \ddots & \vdots \\ q^{1-nb}[u] \cdot q^0[u] & \cdots & q^{1-nb}[u] \cdot q^{1-nb}[u] & q^{1-nb}[u] \cdot q^{-1}[y] & \cdots & q^{1-nb}[u] \cdot q^{-na}[y] \\ q^{-1}[y] \cdot q^0[u] & \cdots & q^{-1}[y] \cdot q^{1-nb}[u] & q^{-1}[y] \cdot q^{-1}[y] & \cdots & q^{-1}[y] \cdot q^{-na}[y] \\ \vdots & \ddots & \vdots & \vdots & \ddots & \vdots \\ q^{-na}[y] \cdot q^0[u] & \cdots & q^{-na}[y] \cdot q^{1-nb}[u] & q^{-na}[y] \cdot q^{-1}[y] & \cdots & q^{-na}[y] \cdot q^{-na}[y] \end{bmatrix} \quad (4.40)$$

Using the property that for a wide sense stationary input with large N ,

$$\lim_{N \rightarrow \infty} \frac{1}{N} \sum_{t=1}^N u(t) = E[u(t)] \quad (4.41)$$

the terms in the above matrix 4.40 can be represented by terms of the auto and cross correlation functions

$$P^{-1} = \frac{1}{N} \Phi \Phi^T = \begin{bmatrix} R_u(1-1) & \cdots & R_u(n_b-1) & R_{uy}(2-1) & \cdots & R_{uy}(n_a+1-1) \\ \vdots & \ddots & \vdots & \vdots & \ddots & \vdots \\ R_u(1-n_b) & \cdots & R_u(n_b-n_b) & R_{uy}(2-n_b) & \cdots & R_{uy}(n_a+1-n_b) \\ R_{yu}(0-1) & \cdots & R_{yu}(n_b-1-1) & R_y(0) & \cdots & R_y(n_a-1) \\ \vdots & \ddots & \vdots & \vdots & \ddots & \vdots \\ R_{yu}(0-n_a) & \cdots & R_{yu}(n_b-1-n_a) & R_y(1-n_a) & \cdots & R_y(0) \end{bmatrix} \quad (4.42)$$

The formation of and $\frac{1}{N} \Phi Y$ follows the same procedure and the result is

$$B = \frac{1}{N} \Phi Y = \frac{1}{N} \begin{bmatrix} y(t) \cdot u(t) \\ \vdots \\ y(t) \cdot u(t+1-n_b) \\ y(t) \cdot y(t-1) \\ \vdots \\ y(t) \cdot y(t-n_a) \end{bmatrix} = \begin{bmatrix} R_{yu}(0) \\ \vdots \\ R_{yu}(n_b-1) \\ R_y(1) \\ \vdots \\ R_y(n_a) \end{bmatrix} \quad (4.43)$$

and the residual error (bias) term from 4.38 can be represented in the same format,

$$F = \frac{1}{N} \Phi \mathbf{v} = \frac{1}{N} \begin{bmatrix} v(t) \cdot u(t) \\ \vdots \\ v(t) \cdot u(t + 1 - n_b) \\ v(t) \cdot y(t - 1) \\ \vdots \\ v(t) \cdot y(t - n_a) \end{bmatrix} = \begin{bmatrix} R_{vu}(0) \\ \vdots \\ R_{vu}(n_b - 1) \\ R_{vy}(1) \\ \vdots \\ R_{vy}(n_a) \end{bmatrix} \quad (4.44)$$

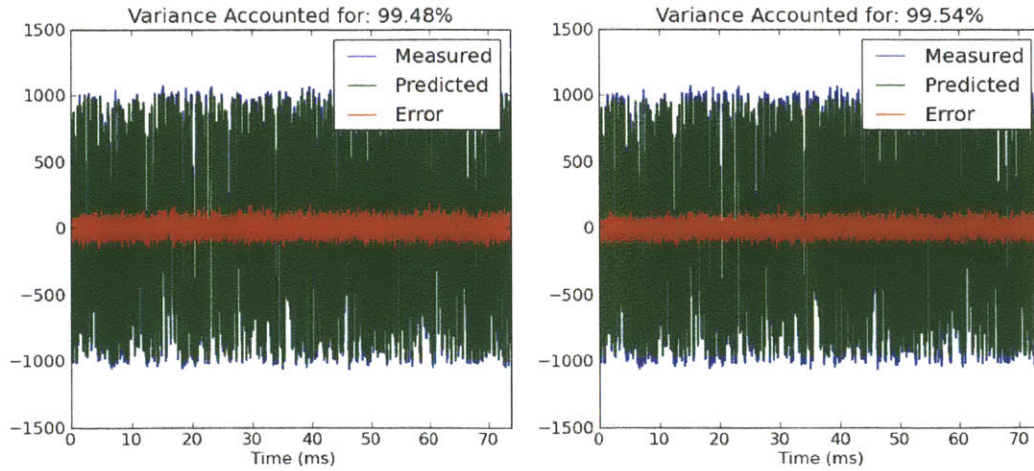
Formation of these matrices using values from the auto-correlation and cross-correlations offers a very simple method for quickly estimating parameters in multiple different model structures without recalculating P^{-1} and B from scratch. It also may be possible to set up conditions for determining an optimal model structure directly through inspection of the autocorrelation and cross correlations although this was not investigated.

4.5.4 Computing model parameters

Once measurements have been taken with the sensor, the data is sent to the computer for processing. The excitation signal and measured response are first centered around their mean and the magnitude of the binary input is set to 1024. The auto and cross-correlations of the two signals are then found using 4.16. Depending on the model, either ARX (4.22) or FIR (4.24) the appropriate P and B matrices are formed and the model parameters are found using 4.35. A prediction of the measured signal is found by convolving the b parameters in 4.26 with the input spectrum using the discrete convolution integral,

$$(f * g)(t) = \sum_{\tau=0}^{\infty} f(\tau)g(t - \tau) \quad (4.45)$$

A vector of the a terms in 4.26 is formed with a zero inserted before the first term. This vector is then convolved with the measured signal and added to the measurement prediction. Because the first term in the a vector is zero the predicted signal at any point only depends on previously measured values. Figure 4.8 shows a comparison between the measured signal and predicted signal for both model structures, with the difference between prediction and measurement shown in red.



ARX: $n_a = 1, n_b = 1$

FIR: $n_a = 0, n_b = 15$

Figure 4.8: Measured signal and predicted signal for two different model structures, the ARX model is on the left and FIR is on the right. The prediction error is shown in red which is comparable for both models.

The variance of the measured signal that is accounted for by the model is comparable for both structures, suggesting both models accurately describe the system. Additionally, there is a highly linear relationship between the physical measurement for a given time point and the corresponding measurement prediction based on the model, figure 4.9.

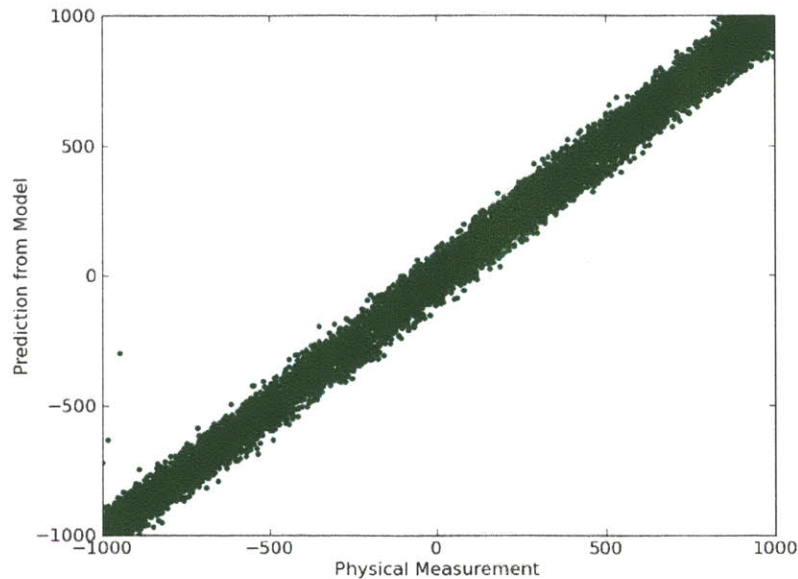


Figure 4.9: The relationship between measurement and model prediction indicates a linear system.

System dynamics were analyzed in the frequency domain by the ratio of the cross spectrum between the measured output and input signal and the power spectrum of the input signal ϕ_{yu}/ϕ_u . The magnitude and phase of this complex number is used to create the Bode plot, figure 4.10.

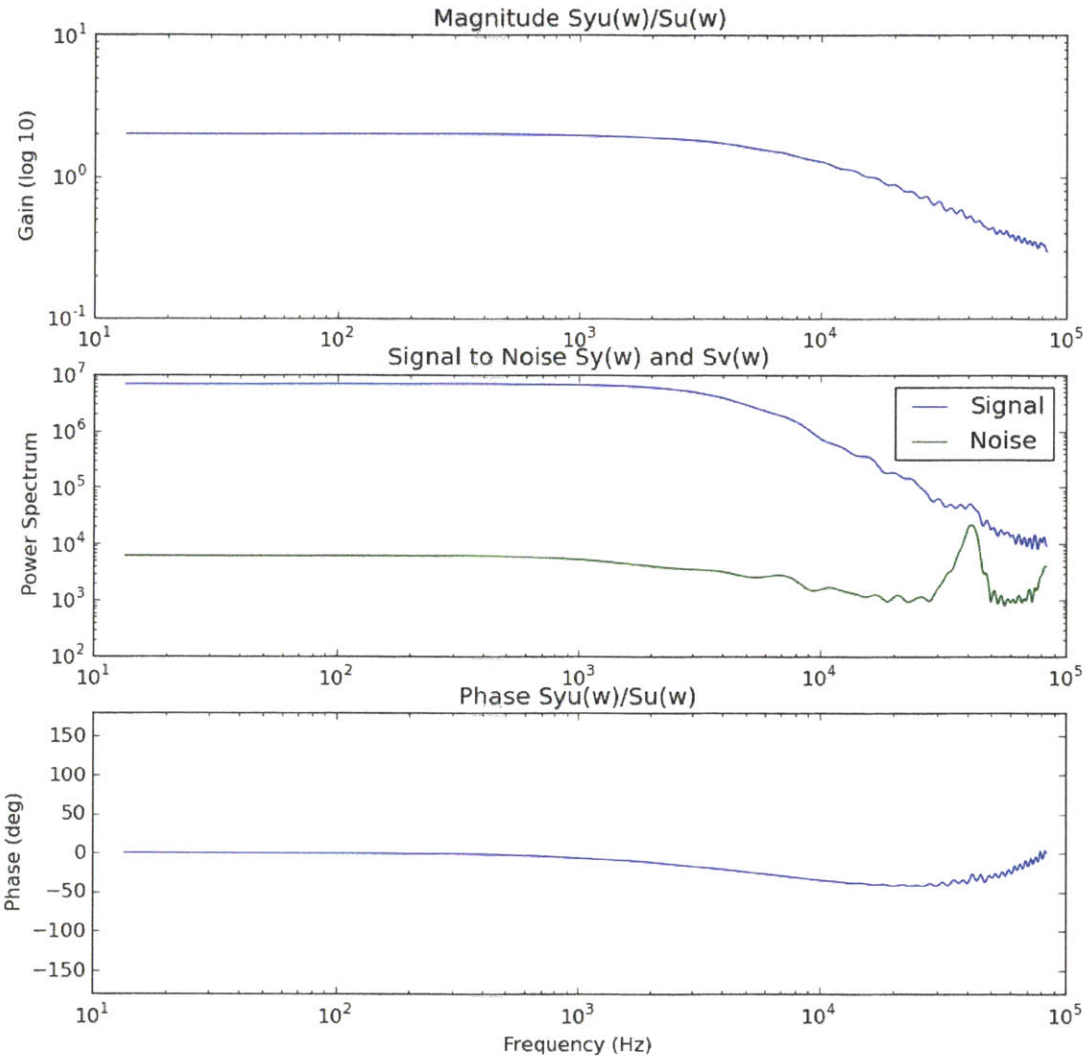


Figure 4.10: Dynamics of the ruthenium sensor presented in the frequency domain. The top and bottom charts show the gain and phase portions of the Bode plot. The middle plot compares the power spectrum of the measured signal to the power spectrum of the noise that is not predictable based on the FIR model.

The power spectrum of the measured signal and power spectrum of the noise were also analyzed. The noise referenced here is not noise in the true sense, but simply the portion of the signal that is not predictable by the model. Since a FIR model was used in this scenario, noise is the portion of the signal that is not predicable based on the excitation pattern. These plots are shown in figure 4.10. Seen in this figure there is some noise in the measured signal between 10 and 100 kHz, but generally the magnitude of the signal is well above noise.

4.5.5 Analysis of noise

Several additional properties of the noise were investigated, the autocorrelation and probability density, figure 4.11. Seen here, the noise follows a Gaussian distribution. Also, there is a correlation between the noise in one sample and the noise in the following series of samples. As was previously shown in equation 4.38 this could introduce a bias in the estimation of the true system model.

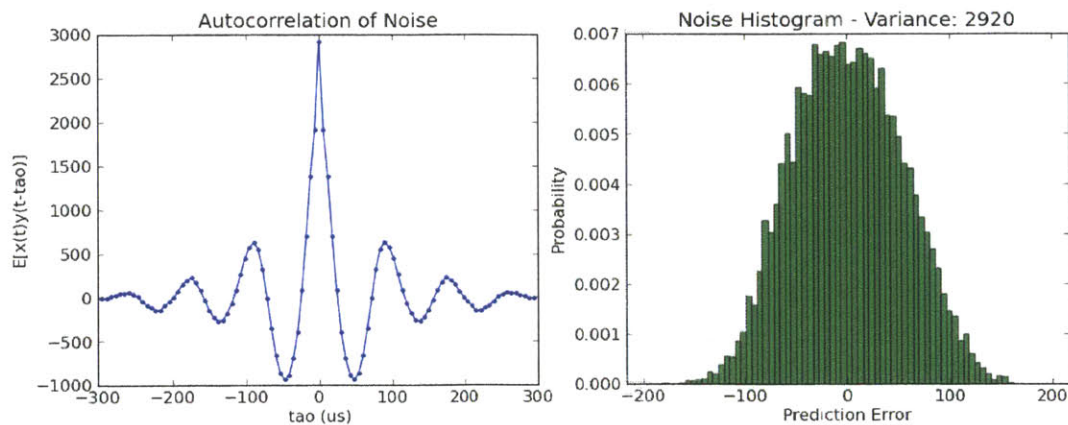


Figure 4.11: Autocorrelation of the measured noise and probability density histogram.

Performing the same analysis using the ARX model leads to a very different result because this model has access to previous measurements and thus estimates the noise dynamics. Figure 4.12 shows the autocorrelation of the prediction error for an ARX structure with two parameters and one with 100 parameters. By giving the model a huge number of degrees of freedom the level of noise that is

completely unpredictable can be determined. The variance of completely random noise is below 1,500, which is roughly 0.3% of the variance of the measured signal, indicating a very good signal to noise ratio.

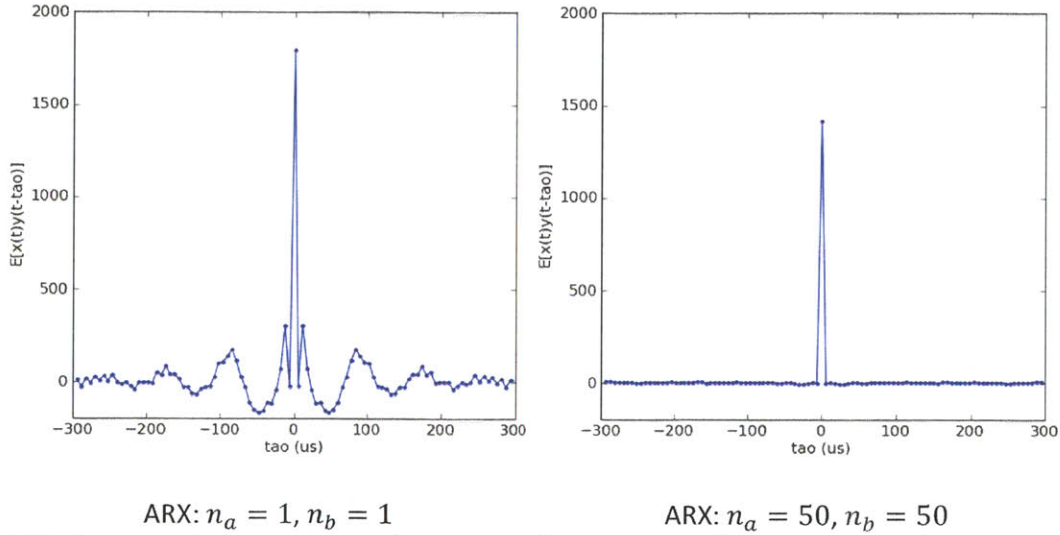


Figure 4.12: Autocorrelation of the prediction error for an ARX model structures with 2 parameters and for a structure with 100 parameters.

4.5.6 Computing the time constant

Two models to describe the system have now been developed. In order to use these models to predict oxygen concentration the first order time constant is found. The output of the FIR model is the impulse response of the system, shown in figure 4.13. The first order impulse is characterized by two parameters, the gain and time constant. These parameters (A and B from equation 4.24) are estimated using the Levenberg–Marquardt algorithm for non-linear least squares. Once A and B have been found, both the FIR and ARX models are completely characterized by only two parameters. Unfortunately, fitting the terms found using the FIR model to a first order time constant means that the time constant is not determined directly by the data set, but indirectly through the terms in the FIR model. It is not guaranteed that the time constant found through this method will minimize the original least squares cost function 4.29 based on the data set.

The impulse response for a representative data set is shown in figure 4.13. This figure plots the 25 measured FIR terms directly from the model and also shows a first order exponential decay fit to these terms. The plot also shows the impulse response as measured by the ARX model. The ARX and fit FIR curves are basically overlapping.

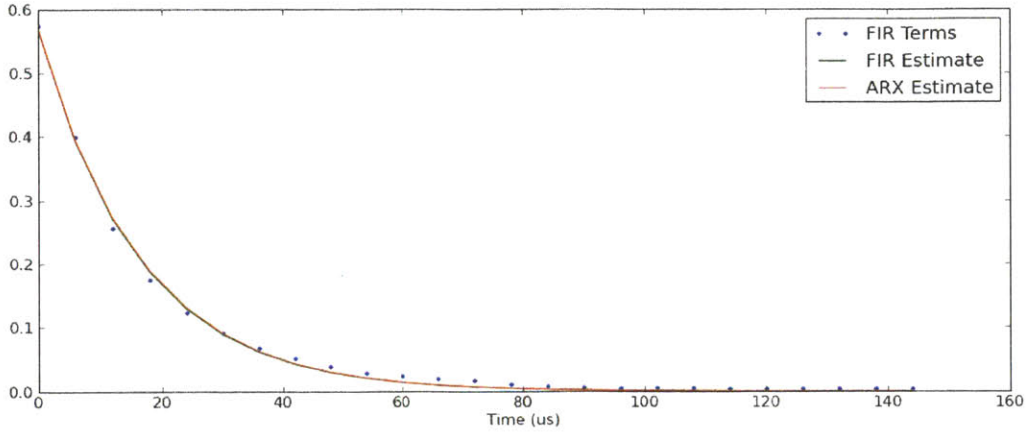


Figure 4.13: Measured impulse response at atmospheric oxygen.

Since the system was sampled at discrete intervals, the final step is to convert the A coefficient to a time constant. Measurements of an event with initial magnitude U at discrete time intervals kT following the event, as predicted by first order decay are

$$y_{k=1} = Ue^{-(T-\delta)/\tau} = \left(Ue^{\delta/\tau} \right) \left(e^{-T/\tau} \right)^1 \quad (4.46a)$$

$$y_{k=2} = Ue^{-(2T-\delta)/\tau} = \left(Ue^{\delta/\tau} \right) \left(e^{-T/\tau} \right)^2 \quad (4.46b)$$

$$y_k = B \left(e^{-T/\tau} \right)^k = BA^k \quad (4.46c)$$

$$A = e^{-T/\tau} \text{ and } \tau = \frac{T}{\ln A^{-1}} \quad (4.47)$$

where δ represents a constant time difference between the original event and the sample intervals. The final equation, 4.47 shows the relation between the time constant and the A_{O_2} term in the models.

4.5.7 Oxygen measurement

The oxygen sensor was enclosed in a vacuum, figure 4.14, and measurements were made across a range of pressures. The measured time constant using an FIR model and the measured gain were used in the Stern-Volmer equation 4.3 to estimate oxygen partial pressure. Calibration coefficients K_{SV} and τ_0 were found by nonlinear curve fitting of the data.

Figure 4.15 shows the oxygen partial pressure as predicted by the oxygen sensor plotted against the oxygen partial pressure as measured on the gauge ($P_{O_2} = 0.2095P_{atm}$). There is a very good correspondence between oxygen measured on the sensor and the partial pressure as calculated from the gauge. There is a slight downward curvature to the fit. This curvature has also been observed by other groups⁸².

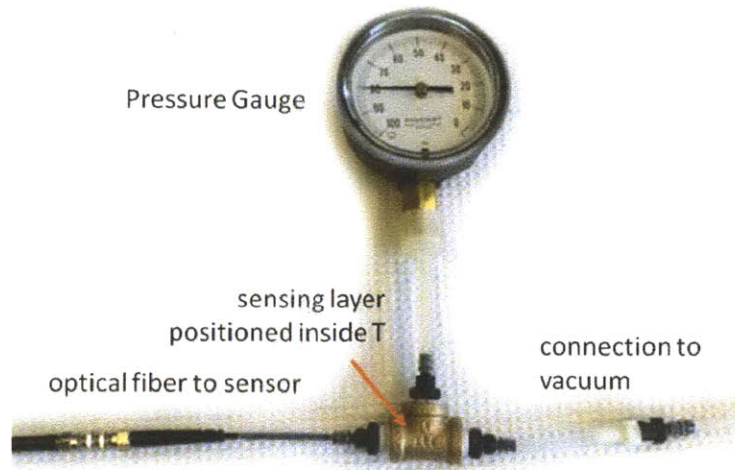


Figure 4.14: Oxygen calibration environmental chamber. The oxygen sensor is contained inside the fitting and regulated pressure is measured on an analog gauge.

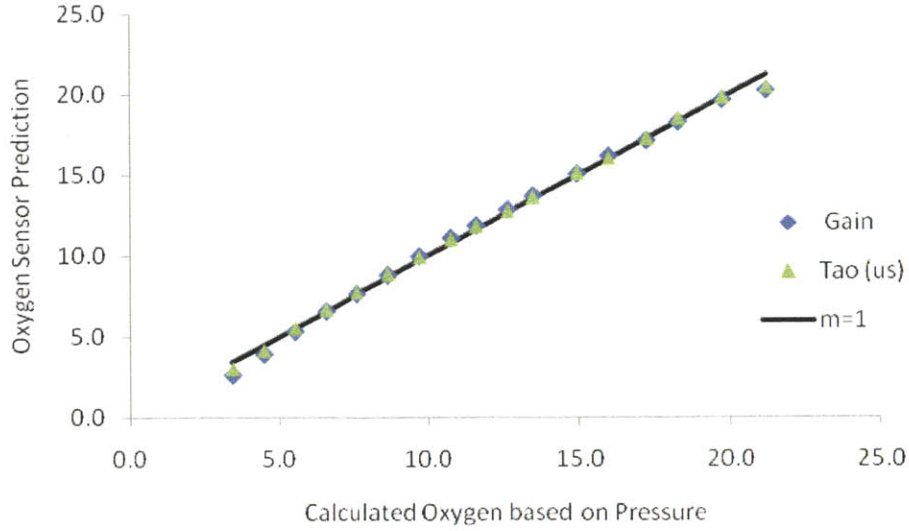


Figure 4.15: Oxygen partial pressure as measured by the optical sensor is compared with oxygen partial pressure measured using a pressure gauge.

4.5.8 Minimizing the excitation period

These sensors are expected to measure oxygen concentration for a very long period of time (~week timescale experiments) at short sampling intervals (~minute timescale) requiring ~10,000 measurements for each experiment. They are expected to be reusable, thus it is highly desirable to minimize the possibility of photo-bleaching the sensor by minimizing the excitation period.

In order to observe the convergence of the parameter estimations, the recursive least squares algorithm was used to calculate the time constant and gain for each sample. After an initial estimation of model parameters $\hat{\theta}_0$ using the first ~100 measurements, the model iterates using the following equations

$$K = \frac{P_{t-1}\varphi_t}{1+\varphi_t^T P_{t-1}\varphi_t} \in R^{m \times 1} \quad (4.48)$$

$$\hat{\theta}_t = \hat{\theta}_{t-1} + K(y_t - \varphi_t^T \hat{\theta}_{t-1}) \quad (4.49)$$

$$P_t = P_{t-1} - \frac{P_{t-1}\varphi(t)\varphi^T(t)P_{t-1}}{1+\varphi^T(t)P_{t-1}\varphi(t)} \quad (4.50)$$

Term convergence using three different models was traced using this method and the results are shown in figure 4.16. The first two models have an FIR structure with 25 and 15 terms, and the third model uses the ARX structure. Seen in the figure, the different model structures are fairly consistent in their estimation of the time constant and rate of convergence. The parameters stabilize after roughly 6,000 samples, indicating the need for a 36 ms excitation period. The error variance for the parameter estimates is overlaid on the top x-axis. It appears that none of the models perfectly minimize the error in the time constant. This discrepancy is because the ARX model has been converted to an FIR structure with no access to previous measurements, and the FIR models have been fit to a first order exponential.

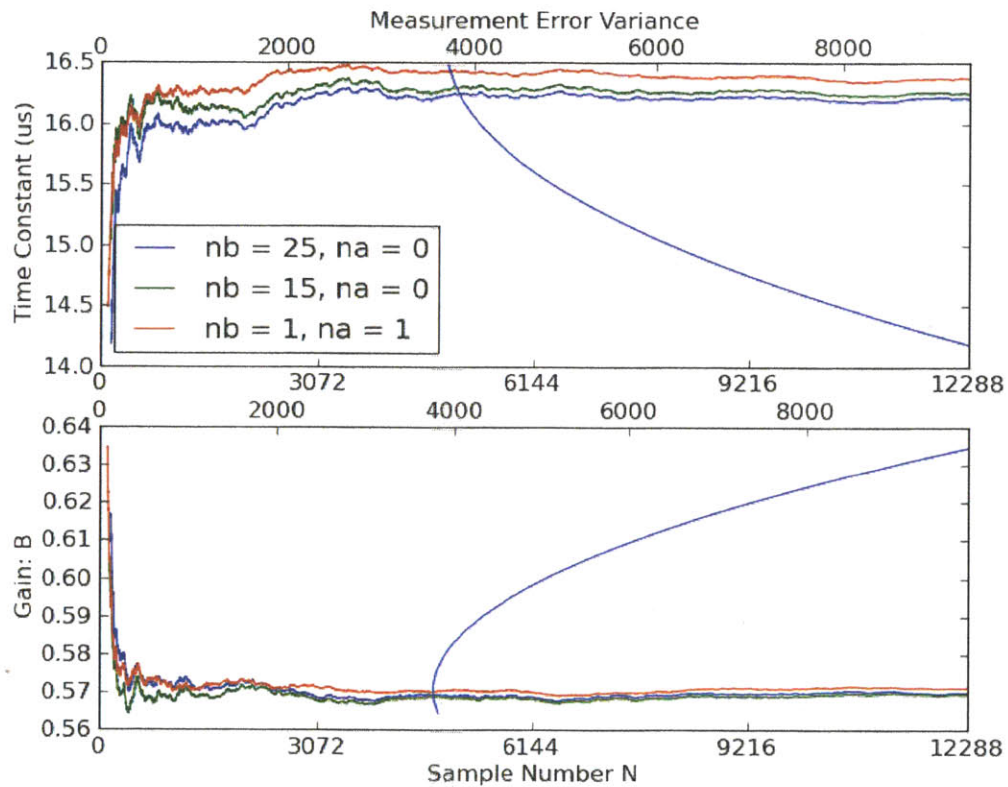


Figure 4.16: Observation of the convergence of the estimated time constant overlaid with error variance for an FIR model fit to a first order decay.

This analysis was preformed for 16 measurements at atmospheric oxygen. The intensity of the signal at atmospheric oxygen is lowest, so these measurements likely represent a worst case scenario based on a

low signal to noise ratio. Figure 4.17 shows the convergence of model parameters for a number of individual measurements, each using the ARX structure. Again, convergence is observed after around 6,000 samples. The time constant estimates have a total range of 500 ns or 3%, with a variance of 20 ns or 0.1%.

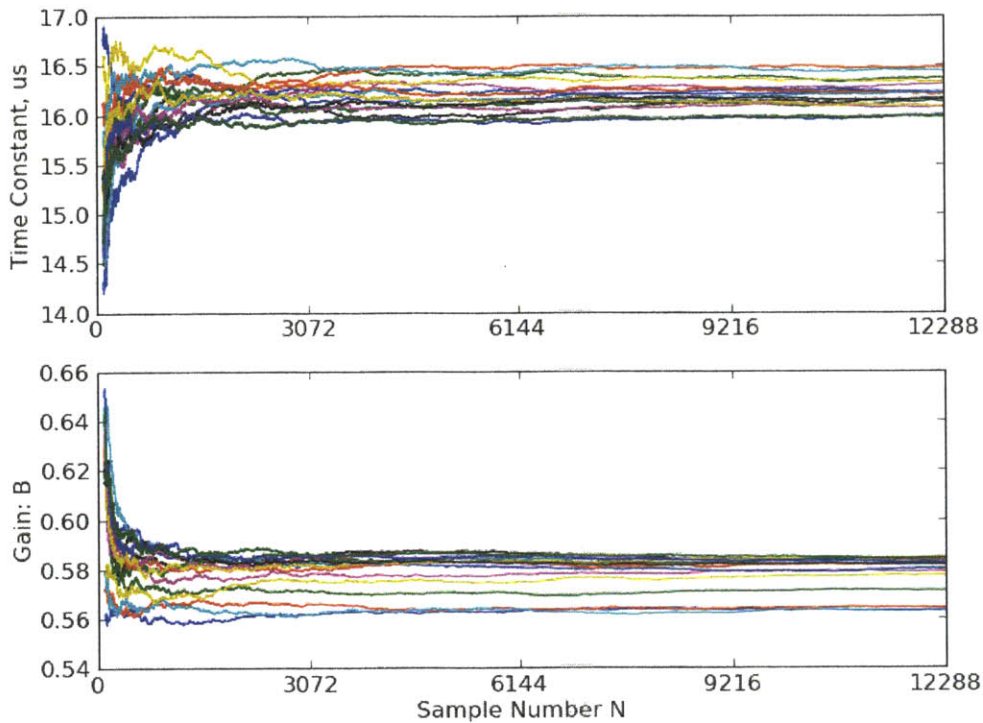


Figure 4.17: Convergence of model parameters for 16 individual measurements at atmospheric oxygen.

4.5.9 Multiplexing sensors with different input signals

Since the sensor is excited using a stochastic pattern it is possible to measure emission from multiple samples using the same photodiode. This can be demonstrated by adding the recorded signals from measurements were the excitation patterns were independent, then performing the system identification technique as usual. Since the excitation patterns are independent, emission from one sensor will appear as noise when analyzed according to the first excitation pattern. If two sensors are multiplexed together the signal to noise ratio (SNR) should be close to 1; for three sensors SNR should

decrease to a half and so on. Figure 4.18 shows the ‘measurement’ which is the true measurement using one pattern corrupted by a second the measurement using an independent excitation pattern. The signal to noise ratio has decreased to 1 as indicated by 50% variance accounted for, yet model parameters are still predicted accurately.

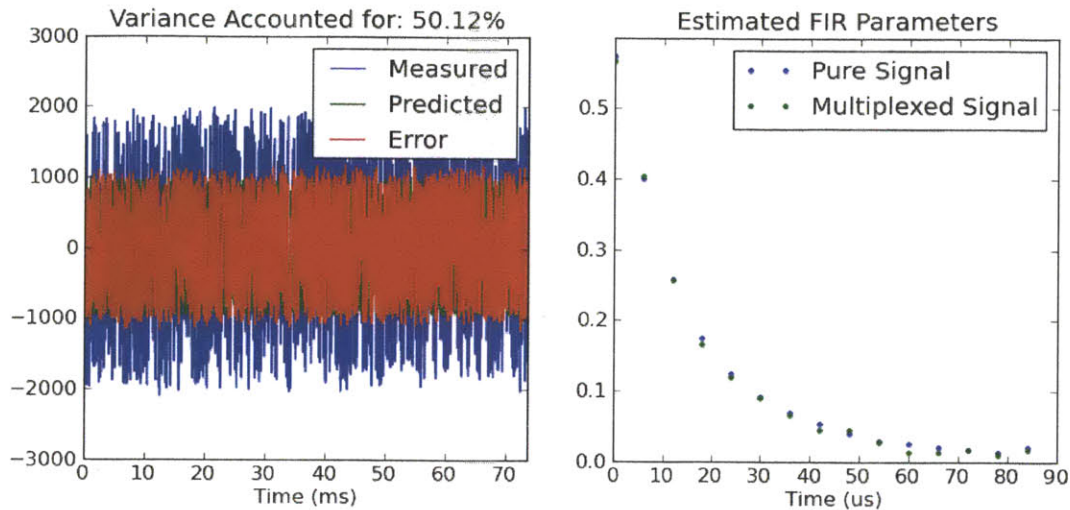


Figure 4.18: Multiplexing two sensors results in low SNR but model parameters are accurately predicted. Although in practice it is difficult to implement this using the current configuration of LED’s and photodiodes it is easy to envision a configuration where this technique could be useful.

4.6 Discussion

An oxygen sensor that can be integrated onto the lid of a bioreactor or tissue culture plate to measure oxygen concentration during cell culture experiments has been developed. Multiple oxygen sensors can be integrated into a single lid in order to measure concentration in all wells. The sensors excite a layer of ruthenium using a stochastic binary signal from a LED. This approach allows rapid identification of the system dynamics of the ruthenium, from which oxygen concentration measurements are obtained. The sensors exhibit very low noise levels and above 99% of the variance in measurements can be accounted for using models with only two parameters.

System identification algorithms based on the autocorrelation and cross-correlations of the input signal and measured response are used. With these correlations, all of the information needed for parameter estimation is contained in a surprisingly small number of terms from the autocorrelation and cross correlation functions. In the case of the ARX model with $n_a = 1$, $n_b = 1$ the entire system model is found using only 5 terms as shown in 4.55

$$\hat{\theta} = \begin{bmatrix} Gain \\ e^{-T/\tau} \end{bmatrix} = \begin{bmatrix} R_u(0) & R_{uy}(1) \\ R_{uy}(1) & R_y(0) \end{bmatrix}^{-1} \begin{bmatrix} R_{yu}(0) \\ R_y(1) \end{bmatrix} \quad (4.55)$$

Although this approach has been demonstrated using ruthenium for sensing oxygen, a number of other materials are available that could be used to sense pH and CO₂ and possibly many more environmental factors²³.

5. CONCLUSIONS

This thesis describes the development of a perfusion bioreactor that fosters the three dimensional culture of liver tissue. The system provides continuous flow of culture medium through a bed of tissue contained in the scaffold. Micro-fluidic pumping systems have been integrated into the device so that the entire culture environment is contained in the format of a standard tissue culture plate. The system integrates seamlessly into existing cell culture facilities.

The robust nature of the pumping system has been demonstrated through extensive characterization. Constant, reliable flow rates are produced by setting a deterministic pump stroke volume and modulating the pump cycle frequency. The pulsatile output from the pumping system is converted to a continuous flow through the use of a fluidic capacitor. Performance of the capacitor has been validated using high-speed imaging to capture the flow output from the pump on a millisecond time scale.

The oxygen environment within the system has been carefully evaluated using a combination of models and measurements. Models were used to predict how bioreactor geometry influences oxygen concentration. With this knowledge, a bioreactor was designed to create several different oxygen environments and this bioreactor was used to determine ideal culture conditions for liver cells. Based on the results from these studies, an ideal oxygen environment was selected and bioreactors that create this environment were fabricated. The utility of online oxygen concentration measurements as an indicator of cell health was also demonstrated.

Optical oxygen sensors were developed. These sensors utilize a stochastic excitation pattern to identify microsecond time scale quenching dynamics of ruthenium complexes by molecular oxygen. Measured fluorescence decay rates can be used to determine the local concentration of oxygen. Stochastic excitation is a novel approach for this class of chemical sensors. The stochastic excitation approach could potentially be used for a variety of additional environmental sensors including CO₂ and pH.

REFERENCES

1. N. J. Hewitt, M. J. Lechon, J. B. Houston, D. Hallifax, H. S. Brown, P. Maurel, J. G. Kenna, L. Gustavsson, C. Lohmann, C. Skonberg, A. Guillouzo, G. Tuschl, A. P. Li, E. LeCluyse, G. M. M. Groothuis and J. G. Hengstler, *Drug Metabolism Reviews*, 2007, **39**, 159-234.
2. H. Meren, T. Matsumura, F. C. Kauffman and R. G. Thurman, *Advances in experimental medicine and biology*, 1986, **200**, 467-476.
3. T. Matsumura, F. C. Kauffman, H. Meren and R. G. Thurman, *A. J. Physiol.*, 1986, **250**, G800-G805.
4. R. Chang, J. Nam and W. Sun, *Tissue Engineering: Part C*, 2008, **14**, 157-166.
5. S. Ostrovidov, J. Jiang, Y. Sakai and T. Fujii, *Biomed. Microdevices*, 2004, **6**, 279-287.
6. J. W. Allen and S. N. Bhatia, *Biotechnol. Bioeng.*, 2003, **82**, 253-262.
7. A. Sin, K. C. Chin, M. F. Jamil, Y. Kostov, G. Rao and M. L. Shuler, *Biotechnol. Prog.*, 2004, **20**, 338-345.
8. P. J. Lee, P. J. Hung, V. M. Rao and L. P. Lee, *Biotechnol. Bioeng.*, 2006, **94**, 5-14.
9. P. J. Lee, P. J. Hung and L. P. Lee, *Biotechnol. Bioeng.*, 2007, **97**, 1340-1346.
10. J. H. Sung and M. L. Shuler, *Lab Chip*, 2009, **9**, 1385-1394.
11. M. J. Powers, K. Domansky, M. R. Kaazempur-Mofrad, A. Kalezi, A. Capitano, A. Upadhyaya, P. Kurzawski, K. E. Wack, D. B. Stolz, R. Kamm and L. G. Griffith, *Biotechnol. Bioeng.*, 2002, **78**, 257-269.
12. K. Domansky, A. Sivaraman and L. G. Griffith, in *Lab-on-Chips for Cellomics-Micro and Nanotechnologies for Life Science*, eds. H. Andersson and A. v. d. Berg, Kluwer Academic Publishers, 2004, pp. 319-346.
13. E. Leclerc, Y. Sakai and T. Fujii, *Biochem. Eng. J.*, 2004, **20**, 143-148.
14. Y.-C. Toh, C. Zhang, J. Zhang, Y. M. Khong, S. Chang, V. D. Samper, D. Noort, D. W. Hutmacher and H. Yu, *Lab Chip*, 2007, **7**, 302-309.
15. K. Domansky, W. Inman, J. Serdy, A. Dash, M. H. M. Lim and L. G. Griffith, *Lab on a Chip*, 2010, **10**, 51-58.
16. A. Rotem, M. Toner, S. Bhatia, B. D. Foy, R. G. Tompkins and M. L. Yarmush, *Biotechnol. Bioeng.*, 1994, **43**, 654-660.
17. L. Kim, Y. Toh, J. Voldman and H. Yu, *Lab Chip*, 2007, **7**, 681-694.
18. A. Rotem, M. Toner, R. G. Tompkins and M. L. Yarmush, *Biotechnol. Bioeng.*, 1992, **40**, 1286-1291.
19. C. H. Cho, J. Park, D. Nagrath, A. W. Tilles, F. Berthiaume, M. Toner and M. L. Yarmush, *Biotechnol. Bioeng.*, 2007, **97**, 188-199.
20. F. G. Gao, A. S. Jeevarajan and M. M. Anderson, *Biotechnology and Bioengineering*, 2004, **86**, 425-433.
21. G. Mehta, K. Mehta, D. Sud, J. Song, T. Bersano-Begey, N. Futai, Y. S. Heo, M.-A. Mycek, J. Linderman and S. Takayama, *Biomedical Microdevices*, 2007, **9**, 123-134.
22. V. Nock, R. J. Blaikie and T. David, *Lab on a Chip*, 2008, **8**, 1300-1307.
23. B. Higgins, B. A. DeGraff and J. N. Demas, *Inorganic Chemistry*, 2005, **44**, 6662-6669.
24. E. Sinkala and D. T. Eddington, *Lab on a Chip*, 2010, **10**, 3291-3295.
25. Y.-E. Koo Lee, E. E. Ulbrich, G. Kim, H. Hah, C. Strollo, W. Fan, R. Gurjar, S. Koo and R. Kopelman, *Analytical Chemistry*, 2010, **82**, 8446-8455.
26. Y. Kuang and D. R. Walt, *Biotechnology and Bioengineering*, 2007, **96**, 318-325.
27. S. Lee, B. L. Ibey, G. L. Coté and M. V. Pishko, *Sensors and Actuators B: Chemical*, 2008, **128**, 388-398.

28. M. H. Keefe, K. D. Benkstein and J. T. Hupp, *Coordination Chemistry Reviews*, 2000, **205**, 201-228.
29. D. Parker, *Coordination Chemistry Reviews*, 2000, **205**, 109-130.
30. I. Klimant, M. Köhl, R. N. Glud and G. Holst, *Sensors and Actuators B: Chemical*, 1997, **38**, 29-37.
31. G. Holst, R. N. Glud, M. Köhl and I. Klimant, *Sensors and Actuators B: Chemical*, 1997, **38**, 122-129.
32. S. J. Payne, J. N. Demas and B. A. DeGraff, *Appl. Spectrosc.*, 2009, **63**, 437-441.
33. B. T. Glazer, A. G. Marsh, K. Stierhoff and G. W. Luther, *Analytica Chimica Acta*, 2004, **518**, 93-100.
34. M. Krihak, M. T. Murtagh and M. R. Shahriari, in *Chemical, Biochemical, and Environmental Fiber Sensors VIII*, SPIE, Denver, CO, USA, 1996, pp. 105-115.
35. M. R. Shahriari, M. T. Murtagh and H.-C. Kwon, in *Chemical, Biochemical and Environmental Fiber Sensors IX*, SPIE, Munich, Germany, 1997, pp. 40-51.
36. A. Sivaraman, K. L. J, S. Townsend, T. Iida, B. J. Hogan, D. B. Stoltz, R. Fry, L. D. Samson, S. R. Tannenbaum and L. G. Griffith, *Curr. Drug. Metab.*, 2005, **6**, 569-591.
37. A. M. Young, T. M. Bloomstein and S. T. Palmacci, *Journal of Biomechanical Engineering*, 1999, **121**, 2-6.
38. Y. Xia and G. M. Whitesides, *Annual Review of Materials Science*, 1998, **28**, 153-184.
39. M. Hecke and W. K. Schomburg, *Journal of Micromechanics and Microengineering*, 2004, **14**, R1.
40. F. Goldschmidtboing and et al., *Journal of Micromechanics and Microengineering*, 2005, **15**, 673.
41. R. Zengerle and M. Richter, *Journal of Micromechanics and Microengineering*, 1994, **4**, 192.
42. B. M. J. L. Q. Yang, *18th IEEE Int. Conf. Micro Electro Mechanical Systems (MEMS 2005)*, 2005, 706.
43. B. L. Q. Yang, *Proc. 9th Int. Conf. on Miniturized Systems for Chemistry and Life Sciences (M₁TAS)*, 2005, 1118.
44. T. W. Astle, *Molecules*, 1996, **1**, 106-113.
45. P. F. Lalor and D. H. Adams, *J. Clin. Pathol: Mol. Pathol.*, 1999, **52**, 214-219.
46. P. P. C. Poyck, G. Mareels, R. Hoekstra, A. C. W. A. Van Wijk, T. V. Van Der Hoeven, T. M. Van Gulik, P. R. Verdonck and R. A. F. M. Chamuleau, *Artificial Organs*, 2008, **32**, 116-126.
47. K. Jungermann and T. Kietzmann, *Hepatology*, 2000, **31**, 255-260.
48. S. Kidambi, R. S. Yarmush, E. Novik, P. Chao, M. L. Yarmush and Y. Nahmias, *Proceedings of the National Academy of Sciences*, 2009, **106**, 15714-15719.
49. T. A. Broughan, R. Naukam, C. Tan, C. J. Van De Wiele, H. Refai and T. K. Teague, *Journal of Surgical Research*, 2008, **145**, 150-160.
50. I. Martinez, G. Nedredal, C. Oie, A. Warren, O. Johansen, D. Le Couteur and B. Smedsrod, *Comparative Hepatology*, 2008, **7**, 4.
51. R. S. McCuskey, *The Anatomical Record: Advances in Integrative Anatomy and Evolutionary Biology*, 2008, **291**, 661-671.
52. D. P. Jones and H. S. Mason, *Journal of Biological Chemistry*, 1978, **253**, 4874-4880.
53. T. Matsumura and R. G. Thurman, *Gastrointest. Liver Physiol.*, 1983, **7**, G656-G659.
54. T. Matsumura and R. G. Thurman, *European Journal of Biochemistry*, 1984, **140**, 229-234.
55. R. G. Thurman and F. C. Kauffman, *Hepatology*, 1985, **5**, 144-151.
56. L. E. Costa, G. Mendez and A. Boveris, *American Journal of Physiology - Cell Physiology*, 1997, **273**, C852-C858.
57. T. Matsumura, H. Yoshihara, R. Jeffs, Y. Takeji, S. Nukina, T. Hijioka, R. K. Evans, F. C. Kauffman and R. G. Thurman, *Gastrointest. Liver Physiol.*, 1992, **25**, G645-G650.
58. K. O. Lindros, *General Pharmacology: The Vascular System*, 1997, **28**, 191-196.

59. H. P. Rani, T. W. H. Sheu, T. M. Chang and P. C. Liang, *Journal of biomechanics*, 2006, **39**, 551-563.
60. D. W. Fawcett and W. Bloom, *A Textbook of Histology*, 1968.
61. K. Ito and J. B. Houston, *Pharmaceutical Research*, 2004, **21**, 785-792.
62. K. Lee, R. A. Roth and J. J. LaPres, *Pharmacology & Therapeutics*, 2007, **113**, 229-246.
63. P. T. Schumacker, N. Chandel and A. G. N. Agusti, *Am. J. Physiol.*, 1993, **265**, L395-L402.
64. A. C. Boretto-Biazon, F. Bracht, L. Bracht, A. M. Kelmer-Bracht and A. Bracht, *Acta Pharmacol. Sin.*, 2009, **30**, 90-97.
65. P. Vaupel, *Pflügers Archiv European Journal of Physiology*, 1976, **361**, 201-204.
66. L. G. Cima, H. W. Blanch and C. R. Wilke, *Bioprocess and Biosystems Engineering*, 1990, **5**, 19-30.
67. M. Horner, W. M. Miller, J. M. Ottino and E. T. Papoutsakis, *Biotechnology Progress*, 1998, **14**, 689-698.
68. J. Grote, R. Süsskind and P. Vaupel, *Pflügers Archiv European Journal of Physiology*, 1977, **372**, 37-42.
69. M. Radisic, J. Malda, E. Epping, W. Geng, R. Langer and G. Vunjak-Novakovic, *Biotechnology and Bioengineering*, 2006, **93**, 332-343.
70. J. P. Kirkpatrick and M. W. Dewhirst, *Radiation Research*, 2008, **169**, 350-354.
71. T. D. Lagerlund and P. A. Low, *American Journal of Physiology - Regulatory, Integrative and Comparative Physiology*, 1991, **260**, R430-R440.
72. G. Strang, *Computational Science and Engineering*, Wellesley-Cambridge Press, 2007.
73. J. J. Xu, P. V. Henstock, M. C. Dunn, A. R. Smith, J. R. Chabot and D. de Graaf, *Toxicological Sciences*, 2008, **105**, 97-105.
74. A. G. B. Amoah, B. J. Gould, D. V. Parke and J. D. F. Lockhart, *Xenobiotica*, 1986, **16**, 63.
75. S. Pillai and P. C. v. d. Vliet, *FRET and FLIM Techniques*, Elsevier, Amsterdam, 2009.
76. Z. Wei and et al., *Journal of Physics D: Applied Physics*, 2003, **36**, 1689.
77. S. J. Payne, G. L. Fiore, C. L. Fraser and J. N. Demas, *Analytical Chemistry*, 2010, **82**, 917-921.
78. I. Klimant and O. S. Wolfbeis, *Analytical Chemistry*, 1995, **67**, 3160-3166.
79. Squire, Verveer and Bastiaens, *Journal of Microscopy*, 2000, **197**, 136-149.
80. P. J. Verveer, Q. S. Hanley and T. W. J. Gadella, in *Laboratory Techniques in Biochemistry and Molecular Biology*, Elsevier, 2009, pp. 59-94.
81. S. Shi, J. Zhou, R. Zong and J. Ye, *Journal of Luminescence*, **122-123**, 218-220.
82. E. Vander Donckt, B. Camerman, F. Hendrick, R. Heme and R. Vandeloise, *Bulletin des Sociétés Chimiques Belges*, 1994, **103**, 207-211.

APPENDIX

Appendix A.1: Generations of bioreactor devices

Reactor A: 2 devices fabricated

- Fluidic plate is made from polysulfone and can be sterilized by autoclave
- 13 mm diameter capacitor
- Pneumatic lines are sealed with tape
- Pneumatic connections to controller through nozzles
- Narrow surface channels connect the reactor and reservoir wells
- Filter supports and gaskets are required for reservoir wells

Reactor B: 1 device fabricated

- Capacitor is covered with dome to ensure the gasket below the scaffold does not slip into the capacitor region

Reactor C: 2 devices fabricated

- Capacitor dome is removed but diameter is reduced to 10 mm to prevent gasket from slipping

Reactor D: 3 devices fabricated

- fluidic channels are drilled at angles to prevent pneumatic leaks between pump features
- filter supports are integrated into reservoir wells, eliminates need for reservoir gaskets

Reactor E: 7 devices fabricated

- extraction pockets on the sides of the scaffold do not reach the bottom of the well, this prevents gasket from slipping out into the pockets

Reactor F: 11 devices fabricated

- pneumatic plates fabricated using solvent bonding, pneumatic indicators added
- pneumatic connections to the controller are made with auto-shut off valves in docking stations
- surface channel widened to increase oxygen absorption
- membranes fabricated by laser machining

Reactor G: 6 devices fabricated

- devices no longer fabricated in house
- screw placement adjusted to improve seals

Reactor H: 3 devices fabricated

- variable oxygen environment: long, medium and short surface channels
- scaffold diameter reduced to 10 mm, capacitor diameter reduced to 8 mm
- filter support integrated into reactor well completely eliminates gaskets
- no filter is used in the reservoir well

Reactor I: 10 devices fabricated

- all high oxygen capacity
- well to well spacing is 9 mm

Appendix A.2: Scaling the mass transport equation

The governing transport equation is

$$\frac{\partial C}{\partial t} = -v\nabla C + D\nabla^2 C - R$$

In order to reduce it to dimensionless form, relevant length and velocity scales should be selected and the first two terms on the right hand side of the equation should be scaled. The ∇ denotes the gradient operator which reduces to $\nabla = \frac{\partial}{\partial x}$ for one dimension in rectangular coordinates.

$$v^* = v/\bar{v}, \nabla^* = L\nabla$$

using these scales, the transport equation becomes

$$\frac{\partial C}{\partial t} = -\left(\frac{\bar{v}}{L}\right)v^*\nabla^*C + \left(\frac{D}{L^2}\right)\nabla^{*2}C - R.$$

Scaling of concentration and reaction terms depends on the order of the reaction and the range of possible concentrations for the problem of interest. Concentration is generally scaled using

$$C^* = \frac{C - C_{min}}{C_{max} - C_{min}},$$

where if there is any reaction term, the minimum concentration is zero. The order of the reaction n influences the scaling of the reaction parameter. There are three types of reactions worth considering, zero order, first order and Michaelis-Menten. In zero order kinetics the reaction rate is a constant $R = k_0$, for first order the reaction rate is proportional to the local concentration $R = k_1C$, and for Michaelis-Menten the reaction rate $R = \frac{R_{max}C}{k_m + C}$ could fall into either a zero or first order regime depending on a characteristic concentration k_m . Where concentrations appear in these rate equations (C and k_m), they should be scaled using the same maximum concentration shown above. After dividing through by C_{max} the governing equation becomes

Zero Order:
$$\frac{\partial C^*}{\partial t} = -\left(\frac{\bar{v}}{L}\right)v^*\nabla^*C^* + \left(\frac{D}{L^2}\right)\nabla^{*2}C^* - \left(\frac{k_0}{C_{max}}\right)$$

First Order:
$$\frac{\partial C^*}{\partial t} = -\left(\frac{\bar{v}}{L}\right)v^*\nabla^*C^* + \left(\frac{D}{L^2}\right)\nabla^{*2}C^* - (k_1)C^*$$

Michaelis-Menten:
$$\frac{\partial C^*}{\partial t} = -\left(\frac{\bar{v}}{L}\right)v^*\nabla^*C^* + \left(\frac{D}{L^2}\right)\nabla^{*2}C^* - \left(\frac{R_{max}}{C_{max}}\right)\frac{C^*}{k_m^* + C^*}$$

Each of the constant coefficients for terms on the right hand side of the equation represents the inverse of the time scale for that process (l/\bar{v} is the time scale for flow). The largest of these coefficients represents the dominant process that maximally influences the rate of change of concentration. The three ratios for each of these terms give several common dimensionless numbers that can be used in order of magnitude analysis of a given transport-reaction scenario.

$$\text{Peclet Number: } Pe = \frac{\text{convective transport}}{\text{diffusive transport}} = \frac{\text{diffusion time}}{\text{convection time}} = \frac{\bar{v}L}{D}$$

$$\text{Thiele Modulus: } \phi^2 = \frac{\text{reaction}}{\text{diffusive transport}} = \frac{\text{diffusion time}}{\text{reaction time}} = \frac{L^2 k C_0^{n-1}}{D}$$

$$\text{Damkohler Number}^3: Da = \frac{\text{transport}}{\text{reaction}} = \frac{\text{diffusion time}}{\text{transport time}} = \frac{LkC_0^{n-1}}{\bar{v}}$$

When the Michaelis-Menten reaction is used, care should be given to the unknown concentration term $\frac{C^*}{k_m^* + C^*}$ when formulating the Thiele Modulus and the Damkohler number. Depending on the ratio of C^* to k_m^* , the time scale for the reaction should or should not include a concentration.

Once the dominant time scale has been selected, all terms are multiplied by the characteristic time scale. Typically the dominant time scale (fastest – smallest) time scale is used. The resulting equation will have one term on the right hand side with no coefficient and two terms with the above dimensionless numbers for coefficients. The smallest time scale is used such that the terms either remain close to unity or are multiplied by very small coefficients and thus can be removed from the equation without a significant impact on the result (the alternative of selecting long time scales pushes some terms to ‘explode’ and is thus undesirable). The final equation, assuming convection is dominant and using Michaelis-Menten kinetics becomes

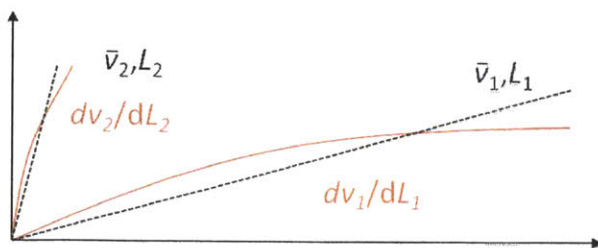
$$\frac{\partial C^*}{\partial t^*} = -v^* \nabla^* C^* + \left(\frac{D}{\bar{v}L}\right) \nabla^{*2} C^* - \left(\frac{LR_{max}}{\bar{v}C_{max}}\right) \frac{C^*}{k_m^* + C^*}$$

and when substituting the dimensionless numbers becomes

$$\frac{\partial C^*}{\partial t^*} = -v^* \nabla^* C^* + Pe^{-1} \nabla^{*2} C^* - Da \frac{C^*}{k_m^* + C^*}$$

Note on Selection of Characteristic Scales for Normalization:

Scaling the governing equation to dimensionless form is important because the order of magnitude of various transport mechanisms is revealed facilitating a comparison of terms and often resulting in drastic simplifications of the equation. The crucial step is selecting the appropriate constants for scaling. The idea is to factor out constants so unknown local derivative terms all have an order of magnitude of 1. For example if an equation term is $\partial v / \partial x$ representing the local gradient of velocity, although this term is unknown, an average velocity and total length scale are known. Terms should be scaled using these known quantities, $(\bar{v}/L) \partial v^* / \partial x^*$, such that the unknown local velocity gradient is close to 1, and the total magnitude (importance) of the term is defined by a known constant. Depending on the magnitude of the constant, it may be possible to eliminate this term from the calculation. If inappropriate scaling constants are used, the order of magnitude of local derivatives may not be 1, and inaccuracies will result.



Unknown local derivative terms shown in red with known scales shown in black. Scaling unknown local parameters to characteristic values sets the local derivative terms close to unity.

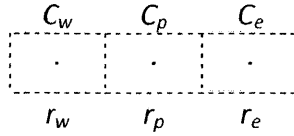
³ The transport term in the Damkohler number could either be diffusion or convection, convection is used here

Appendix A.3: 1D Radial diffusion reaction finite differences

Governing Equation:

$$\frac{\partial C}{\partial t} = D \left[\frac{1}{r} \frac{\partial}{\partial r} \left(r \frac{\partial C}{\partial r} \right) + \frac{\partial^2 C}{\partial z^2} \right] - \frac{R_{max} C}{k_m + C} \quad (\text{A.1})$$

Discretized:



$$\frac{C_p^{t+1} - C_p}{\Delta t} = D \left[\frac{1}{r_p} \frac{1}{\Delta r} \left(\frac{r_w + r_p}{2} \frac{C_w - C_p}{\Delta r} - \frac{r_p + r_e}{2} \frac{C_p - C_e}{\Delta r} \right) \right] - \frac{R_{max} C_p}{k_m + C_p} \quad (\text{A.2})$$

$$C_p^{t+1} = C_p + \Delta t \left[D \left(\frac{(r_w + r_p) C_w - (r_w + 2r_p + r_e) C_p + (r_p + r_e) C_e}{2r_p \Delta r^2} \right) - \frac{R_{max} C_p}{k_m + C_p} \right] \quad (\text{A.3})$$

In vector form:

$$C_p^{t+1} = \left(1 - \Delta t \frac{D_{O_2}}{\Delta r^2} \frac{r_w + 2r_p + r_e}{2r_p} - \Delta t \frac{R_{max}}{k_m + C_p} \right) C_p + \Delta t \frac{D_{O_2}}{\Delta r^2} \frac{r_w + r_p}{2r_p} C_w + \Delta t \frac{D_{O_2}}{\Delta r^2} \frac{r_p + r_e}{2r_p} C_e \quad (\text{A.4})$$

$$C_p = [C_1 \quad \dots \quad C_N], \quad (\text{A.5})$$

$$r_p = r_f + \Delta r ([1 \quad \dots \quad N] - 0.5), \quad (\text{A.6})$$

$$\frac{C_0 + C_1}{2} = C_{edge}, C_0 = 2C_{edge} - C_1, \text{ known interface concentration} \quad (\text{A.7})$$

$$D_{O_2} \frac{C_N - C_{N+1}}{\Delta r} = 0, C_{N+1} = C_N, \text{ known interface transport} \quad (\text{A.8})$$

$$r_0 = r_f, \text{ radius of flow path} \quad (\text{A.9})$$

$$r_p = r_f + n\Delta r, \text{ radius at a point} \quad (\text{A.10})$$

$$\Delta r = \frac{r_c - r_f}{N}, \text{ radius of channel } (r_c) \quad (\text{A.11})$$

Python Code: diffusion_reaction.py

```
#!/usr/bin/env python
"""
Oxygen Diffusion and Reaction in 1D cylindrical coords.
Reaction used MM equation:  $R = R_{max}C/(km+C)$ 
rc = channel radius (mm)
rf = fluid path radius (mm)
h = channel height (mm)
N = number of points to estimate
C = concentration
c0 = fixed concentration at inside of fluid channel
Do2 = diffusion coefficient for O2 (sq mm / s)
Rmax = max consumption rate (uM/s or pmol/uL/sec)
km = MM rate parameter ( $R = R_{max}C/(km+C)$ )
'F5' runs the simulation
Created on Mon Apr 25 11:36:49 2011
@author: winman@mit.edu
"""

from __future__ import division
from __future__ import print_function

import os
import matplotlib.pyplot as plt
import numpy as np

def drxn(df):
    rc = 0.34/2
    rf = df/2
    h = 0.20
    V = h*np.pi*(rc**2-rf**2)
    N=25

    c0 = 180
    km = 2
    Rmax = 60
    Do2 = 2.0e-3

    C = np.ones(N)*c0
    dr = (rc-rf)/N
    r = rf + dr*(np.arange(1,N+1)-0.5)
    rw = rf + dr*(np.arange(N)-0.5)
    re = rf + dr*(np.arange(1,N+1)+0.5)
    rp = (rw+2*r+re)/(2*r)
    rw = (rw+r)/(2*r)
    re = (re+r)/(2*r)

    dt = 0.25*min(dr**2/(25*Do2),(km+c0)/Rmax)
    tf = 5*max((rc-rf)**2/(25*Do2),(km+c0)/Rmax)
    M = int(tf/dt)
    R = np.zeros(M)
```

```
for t in range(M):
    Cw = dt*Do2/dr**2*rw*np.insert(C,0,c0)[-1]
    Ce = dt*Do2/dr**2*re*np.append(C,C[-1])[1:]
    Cp = (1-dt*Do2/dr**2*rp-dt*Rmax/(km+C))*C
    C = Cp + Cw + Ce
    R[t]=2*np.pi*dr*h*np.dot(r,C*Rmax/(km+C))

t = dt*np.arange(M)
C = np.insert(C,0,c0)
r = np.insert(r,0,rf)
return(R,R[-1],C,t,r,V)

if __name__ == "__main__":
    os.chdir(os.path.expanduser('~\\Desktop'))

    df = [0.1, 0.125, 0.15, 0.175, 0.2, 0.225, 0.25]
    R, Rf, C, t, r, V = [], [], [], [], [], []

    for k in range(len(df)):
        (a,b,c,d,e,f)=drxn(df[k])
        R.append(a)
        Rf.append(b)
        C.append(c)
        t.append(d)
        r.append(e)
        V.append(f)

    for k in range(len(df)):
        plt.plot(t[k],R[k])
        plt.xlabel('time (s)')
        plt.ylabel('reaction rate (pmol/s)')
        plt.show()

    # plt.subplot(211)
    for k in range(len(df)):
        plt.plot(r[k]*1000,C[k])
        plt.xlim((0,340/2))
        plt.ylim((0,C[0][0]))
        plt.xlabel('Radial Position (um)')
        plt.ylabel('Concentration (uM)')
        plt.legend(('100','125','150','175','200','225','250'),
                  loc='lower left')
        plt.show()

    Rf = np.array(Rf)
    V = np.array(V)*1000
    # plt.subplot(212)
    plt.plot(V,Rf,'bo')
    plt.xlabel('tissue volume (nL)')
    plt.ylabel('Observed Consumption (pmol/s)')
    plt.show()
```

Appendix A.4: Navier-Stokes approximations using finite differences

The algorithm for modeling Navier-Stokes equation was adopted from Seibold (http://www-math.mit.edu/cse/codes/mit18086_navierstokes.pdf). This algorithm solves Navier-Stokes equations, by dividing the time derivative into several sub-steps.

$$\text{NS, x-dimension:} \quad \frac{\partial u}{\partial t} = - \left(u \frac{\partial u}{\partial x} + v \frac{\partial u}{\partial y} \right) + \frac{\partial p}{\partial x} + \frac{1}{Re} \cdot \left(\frac{\partial^2 u}{\partial x^2} + \frac{\partial^2 u}{\partial y^2} \right)$$

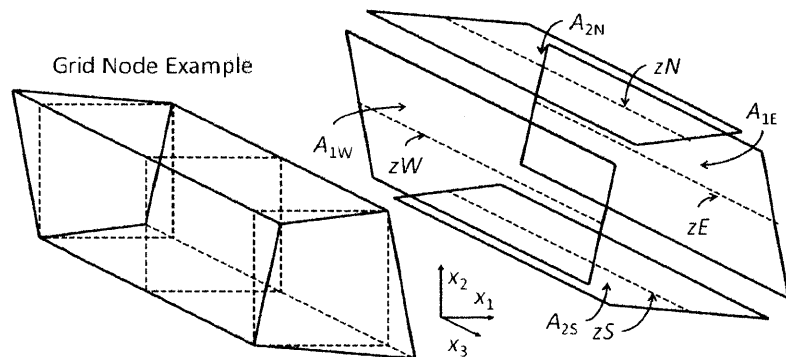
$$\text{NS, y-dimension:} \quad \frac{\partial v}{\partial t} = - \left(u \frac{\partial v}{\partial x} + v \frac{\partial v}{\partial y} \right) + \frac{\partial p}{\partial y} + \frac{1}{Re} \cdot \left(\frac{\partial^2 v}{\partial x^2} + \frac{\partial^2 v}{\partial y^2} \right)$$

$$\text{continuity equation:} \quad \frac{\partial u}{\partial x} + \frac{\partial v}{\partial y} = 0$$

Analysis of the first term on the right hand side of the Navier Stokes proceeds explicitly (forward in time) since this term is nonlinear. Progressing forward in time is slow because the fluid profile can only be allowed change by a small amount for each node. This limit is set so that the changes during any single time step should only influence nodes that are directly adjacent.

The viscosity terms are handled next. These terms are linear so they can be handled implicitly by solving a system of equations. Since a system of equations is used, all nodes can interact and there is no limitation on the total amount of change during any one time step. This speeds up the computation considerably. Finally, the pressure term is combined with the continuity and is also treated implicitly. These three sub-steps are performed for each iteration in time until the flow profiles stabilize.

In order to begin to account for the three dimensional geometry of the system, a fully 3D continuity equation was used. The depth of the four sidewalls for every node is used as a constraint so that continuity is appropriately maintained as the depth of the simulation changes. Simulation depth changes in the bioreactor when fluid flows from the cylindrical well to the rectangular surface channel, and when the surface channel tapers between the scaffold and reservoir.



Appendix A.5: Analysis of flow in the filter

Filter Hydraulic Permeability: $0.735 \frac{mm/s}{kPa}$, Filter thickness: 0.11 mm

Permeability normalized to thickness $80 \times 10^{-3} \frac{mm^2}{s kPa} [=] \frac{mm^3 s}{kg}$

Does no-slip boundary condition influence, or is Darcy permeability govern, use Brinkman Equation:

$$\nabla P = \mu \nabla^2 v - \frac{1}{K} v$$

Comparison of $\mu/L^2 = 7.1 \times 10^{-7} \frac{kg}{mm s} / 0.11^2 mm^2 = 5.8 \times 10^{-5} \frac{kg}{mm^3 s}$ with $1/K = 12.5 \frac{kg}{mm^3 s}$ shows Darcy permeability dominates and viscosity can be neglected. Continuity and the Darcy Permeability equation must be solved simultaneously.

Continuity:
$$0 = \nabla v = \frac{1}{r} \frac{\partial}{\partial r} r v_r + \frac{\partial v_y}{\partial y}$$

Darcy's Law:
$$v = -K \nabla p, v_r = -K \frac{dp}{dr}, v_y = -K \frac{dp}{dy}$$

Combining the two equations yields

$$\frac{1}{r} \frac{\partial}{\partial r} r \left(-K \frac{dp}{dr} \right) + \frac{\partial}{\partial y} \left(-K \frac{dp}{dy} \right) = 0$$

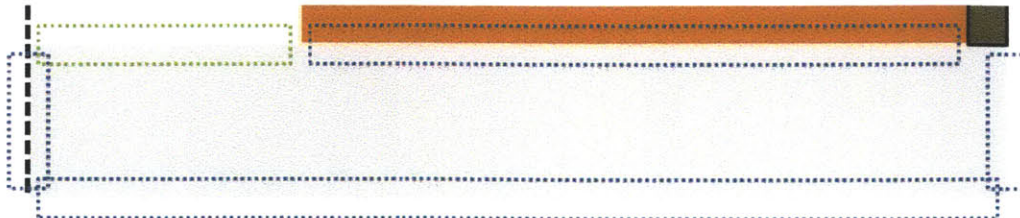
Discretizing the equation on the same grid as in A.3 (with the concentration field replaced by the pressure field yields

$$\frac{(r_w + r_p)/2 P_w - (r_w/2 + r_p + r_e/2) P_p + (r_p + r_e)/2 P_e}{r_p \Delta r^2} + \frac{P_n - 2P_p + P_s}{\Delta y^2} = 0$$

$$\frac{1}{\Delta y^2} P_s + \frac{(r_w + r_p)}{2 r_p \Delta r^2} P_w - \left(\frac{r_w + 2r_p + r_e}{2 r_p \Delta r^2} + \frac{2}{\Delta y^2} \right) P_p + \frac{(r_p + r_e)}{2 r_p \Delta r^2} P_e + \frac{1}{\Delta y^2} P_n = 0$$

Boundary Conditions:

The boundary conditions of the regions outlined with blue boxes in figure A.4.1, at the centerline of the channel, underneath the cells and at the outside of the simulation all specify a known velocity ($v = 0$), so the boundary condition is $dp/dx = v/K$. At the center of the channel and below the filter the velocity is unknown but there is a constant (arbitrary) pressure across this surface, so $P=0$ at the top and $P=1$ (dimensionless) at the bottom. The final solution can be scaled to find the appropriate total flow.



The solution is found by solving a system of equations $0=[\text{coefficients matrix}]*[\text{pressure vector}]+[\text{P boundary condition}]$. This will result in a pressure field. Darcy's law can now be used to find the velocity between each of the nodes.

Internal nodes are simple to formulate. Nodes on the boundary are a bit more complicated, but they follow the same pattern. This will be demonstrated setting up a single node, at the bottom left P(1). Since the y velocity is known between P(1) and the node to the left, once can solve for P_w as a function of P_p , then substitute into the equation for internal nodes. P_s has been set to a dimensionless pressure of 1.

From Darcy's Law:

$$v_x = -K \frac{P_w - P_p}{\Delta x}, \text{ so } P_w = P_p + \frac{v_r \Delta r}{K}$$

It greatly simplifies the construction of the coefficient matrix for pressures and boundary condition to replace the coefficients in the general equation with variables:

$$\text{south} = -\frac{1}{\Delta y^2}, \text{ west} = -\frac{(r_w + r_p)}{2r_p \Delta r^2}, \text{ east} = -\frac{(r_p + r_e)}{2r_p \Delta r^2}, \text{ north} = -\frac{1}{\Delta y^2}, \text{ point} = \left(\frac{r_w + 2r_p + r_e}{2r_p \Delta r^2} + \frac{2}{\Delta y^2} \right)$$

$$\text{south} \cdot P_s + \text{west} \cdot P_w + \text{point} \cdot P_p + \text{east} \cdot P_e + \text{north} \cdot P_n = 0$$

Then substituting in for the boundary conditions:

$$\text{south} \cdot (1) + \text{west} \cdot \left(P_p + \frac{v_r \Delta r}{K} \right) + \text{point} \cdot P_p + \text{east} \cdot P_e + \text{north} \cdot P_n = 0$$

Re-arranging yields:

$$(\text{point} + \text{west}) \cdot P_p + \text{east} \cdot P_e + \text{north} \cdot P_n = -(1) \cdot \text{south} - \left(\frac{v_r \Delta r}{K} \right) \cdot \text{west}$$

So, the first line of the coefficient matrix becomes:

$$[(\text{point} + \text{west}), \text{east}, 0, \dots, 0, \text{north}, 0, \dots] * [\text{P vector}] = [-\text{south} - v_r \Delta r / K * \text{west}]$$